UC Santa Barbara
UC Santa Barbara Electronic Theses and Dissertations

Title
Classification, design and mechanical performance of periodic trusses

Permalink
https://escholarship.org/uc/item/7p88c32r

Author
Latture, Ryan

Publication Date
2018

Supplemental Material
https://escholarship.org/uc/item/7p88c32r#supplemental

Peer reviewed|Thesis/dissertation

University of California

Santa Barbara

Classification, design and mechanical performance of periodic trusses

A dissertation submitted in partial satisfaction

of the requirements for the degree

Doctor of Philosophy

in

Materials

by

Ryan Michael Latture

Committee in charge:

Professor Frank W. Zok, Chair
Professor Matthew R. Begley
Professor Robert M. McMeeking
Professor Otger Campàs

June 2018

The Dissertation of Ryan Michael Latture is approved.

_____

Professor Matthew R. Begley

_____

Professor Robert M. McMeeking

_____

Professor Otger Campàs

_____

Professor Frank W. Zok, Committee Chair

May 2018

Classification, design and mechanical performance of periodic trusses

Copyright © 2018

by

Ryan Michael Latture

Acknowledgements

I'd like to thank my adviser, Frank Zok, for his patience and guidance when I needed it most. His incisive questions during our meetings have helped develop my critical thinking, and working with him to distill the ideas of a manuscript into a clear, concise form has improved my writing immensely. I'd also like to thank Matthew Begley. He has a unique talent for seeing potential in every project. His interesting ideas and new directions would often get research back on track at times I thought I'd reached a dead end. His help has been invaluable. I am grateful for the other members of my committee, Robert McMeeking and Otger Campàs, for sharing their time and expertise. I am fortunate to have been able to collaborate with and learn from each of you.

I'd like to thank my colleagues in the Begley, McMeeking and Zok groups. In particular, I'm greatly indebted to John Shaw and Michael Rossol for their advice and support throughout my time at UCSB, to Varun Rajan for always entertaining my mechanics questions and to Jonathan Berger for his help with Abaqus and all the problems therein.

Finally, I'd like to thank my family for their faith that even I, one day, would finish my Ph.D. and Katelyn for her constant love and support.

Curriculum Vitæ

Ryan Michael Latture

Education

2008–2012	B.S. in Materials Science and Engineering University of Tennessee Knoxville, TN
2012–2018	Ph.D. in Materials University of California, Santa Barbara Santa Barbara, CA

Publications

Ryan M Latture, Matthew R Begley, and Frank W Zok. Defect sensitivity of truss strength. *in preparation.*

Ryan M Latture, Matthew R Begley, and Frank W Zok. Design and mechanical properties of elastically isotropic trusses. *Journal of Materials Research*, 33(3):249–263, 2018.

Ryan M Latture, Ricardo X Rodriguez, Larry R Holmes, and Frank W Zok. Effects of nodal fillets and external boundaries on compressive response of an octet truss. *Acta Materialia*, 2018.

Frank W Zok, **Ryan M Latture**, and Matthew R Begley. Periodic truss structures. *Journal of the Mechanics and Physics of Solids*, 96:184–203, 2016.

NJ Ghimire, Michael A McGuire, David S Parker, Brian C Sales, J-Q Yan, V Keppens, M Koehler, **Ryan M Latture**, and D Mandrus. Complex itinerant ferromagnetism in noncentrosymmetric $Cr_{11}Ge_{19}$. *Physical Review B*, 85(22):224405, 2012.

Abstract

Classification, design and mechanical performance of periodic trusses

by

Ryan Michael Latture

Periodic truss structures can be designed with high specific stiffness and specific strength, exceeding those of stochastic foams by an order of magnitude at low relative densities. Despite the recognition of the enormous potential of periodic trusses, stochastic foams are still used in many applications. Two factors that limit the adoption of trusses are addressed in the present work: (i) there are no widely-accepted descriptors of truss structure, and (ii) many studies neglect effects that come into play in real (finite) truss structures. Instead, previous analyses largely focused on notional truss materials: aggregates of many struts with dimensions much smaller than macroscopic scales of interest. This approach fails to capture the effects of external boundaries which are key to understanding the performance of manufactured trusses. The goals of the present study are to: (i) develop a conceptual framework for classification of truss topologies that enables identification of topologies with potentially attractive mechanical attributes; (ii) couple this framework with robust finite element models to predict deformation and failure of trusses; and (iii) provide new insights into the roles of realistic features that can limit truss performance, including the presence of free surfaces, nodes with finite stiffness and strength, and

defects in the form of individual missing struts. These goals are pursued through a combination of finite element simulations of the mechanical responses of trusses under compressive, tensile or shear loadings and experimental studies on mechanical properties of select truss structures, employing digital image correlation to examine in detail deformation and failure of individual constituent struts as well as the structure as a whole.

The present work begins by establishing a system for classification of truss structure. By systematically stepping through and analyzing structure types identified through the classification system, several maximally-stiff, elastically-isotropic trusses are identified. In finite-sized trusses, strain elevations are obtained in struts near the external free boundaries: a consequence of reduced nodal connectivity and thus reduced constraint on strut deformation and rotation. Some of these effects can be mitigated by circular nodal fillets, which are shown to enhance the bending stiffness of the strut ends and thus increase the stress for buckling (by $\approx 20\%$ for the geometries tested). In all trusses studied, the strain elevations due to bulk defects (distant from free surfaces) are comparable to or lower than those associated with the surfaces themselves. Although defects located at truss corners and truss edges cause the highest elevations in strut strains, their effects on truss strength are small (5–25%). The results provide a set of design guidelines that, when used in combination, yield trusses that are defect tolerant, possess high stiffness and achieve the full strength potential of the truss.

Contents

List of Figures

xiii

xvii

List of Tables

Chapter 1

Introduction

Cellular structures and materials are ubiquitous in biological systems [61], structural engineering [18] and materials science [20]. Broadly, they consist of periodic arrays of plate- or strut-like elements. They can be designed to most efficiently exploit the properties of the constituent elements and/or the intervening spaces in achieving functionality, *e.g.*, bearing loads, enabling fluid flow, facilitating heat transfer, altering optical transmission. They are generally superior to structures in which the elements are distributed in a non-periodic manner, *e.g.* stochastic foams [18]. In some cases (*e.g.* photonic materials), periodicity is essential to achieving functionality.

For load bearing applications, periodic strut-based structures and materials — hereafter collectively referred to as trusses — are preferred over stochastic foams. In low relative density applications, the stiffness and strength of properly designed

trusses can exceed that of a stochastic foam by a factor of 10 [11]. The difference arises from the dominant deformation mechanisms of each topology: stochastic foams deform by strut bending whereas properly designed trusses deform by strut stretching.

In stretch-dominated trusses, struts are loaded axially in either tension or compression and thus the macroscopic truss stiffness is proportional to the extensional strut stiffness. Since extensional stiffness (determined from the cross-sectional area of the struts) scales linearly with relative density, stiffness scales similarly: $E \propto E_0 \rho$ where E and E_o are the Youngs moduli of the truss and the constituent strut material and ρ is relative density. Analogously, if truss failure is dominated by yielding, the yield stress σ_y also scales linearly with ρ: $\sigma_y \propto \sigma_{y,o} \rho$ where $\sigma_{y,o}$ is the yield strength of the solid.

In contrast, stochastic foams exhibit bend-dominated behavior. That is, rather than changing length, struts bend under an applied load and thus truss stiffness and strength are proportional to the bending stiffness and yield strength, respectively. As a result, these properties follow power-law scalings with relative density: $E \propto E_o \rho^2$ and $\sigma_y \propto \sigma_{y,o} \rho^{1.5}$ [20]. To retain favorable scaling ($\propto \rho$) at low relative densities, trusses must be designed to ensure stretch-dominated response.

Trusses are under development for use in an incredibly broad range of technolo-

gies, including structural biomedical implants [38], aerospace and naval structures [18], cushioning and force protection systems [59], thermal management [59], actuated structures [16, 25] and photonic materials [2, 3]. Five main classes of fabrication routes have been employed.

(i) Investment casting has been used to make laboratory-scale metallic truss structures [10, 12, 62]. Typically, a pattern is created using additive manufacturing techniques (see below) and is then used to form the mold. Casting alloys are poured into the mold to form the truss. This method has been used to manufacture small quantities of high-quality trusses provided the aspect ratio of the struts is not too high ($l/2r < 14$, where l is strut length and r is radius) and individual members are are not too thin ($r > 1$mm) [10]. However, investment casting is generally the most expensive and least amenable to large-scale production relative to other fabrication routes because of the high labor and material costs involved.

(ii) Fabrication schemes based on conventional machining, bending, assembly and joining of sheet materials have been devised as a low-cost method to make trusses [13, 42, 48, 59]. In one version, diamond-shaped holes are punched or laser-machined into thin steel sheet, leaving an X-pattern of narrow struts. The sheet is then bent along lines of nodes to produce one layer of the targeted

truss. Brazing methods are used to join the nodes of successive layers [60]. When bending is not required, this method is also amendable to carbon fiber composites. Instead of brazing, joints of the composite truss are joined using a high strength epoxy [14].

(iii) Metallic trusses can also be made by weaving wires into the desired structure and subsequently brazing the wires together [29, 59]. One of the drawbacks is that the weaving operations yield wavy or kinked strut segments between nodes. Moreover, since the nodes are formed by brazing of contacting wires, the integrity of these nodes is likely to be strength-limiting.

(iv) Self-propagating photocuring (SPPC) of photosensitive polymers has found utility in rapid fabrication of polymer trusses for use in impact mitigation and cushioning systems [26, 27, 28]. The main advantage of this process is the short time needed for polymerization (typically less than a minute). Metallic lattices can been formed by electroplating and etching away a polymeric template [53, 58], and polymer-derived ceramic trusses can be formed from pyrolizing pre-ceramic trusses formed from UV-curable resins [17]. One significant limitation of SPPC is its restriction to topologies in which all struts intersect one of the external faces. That is, it is inherently a "line-of-sight" curing method.

(v) Additive manufacturing (AM) offers the widest range of material and topology options. Broadly, AM consists of several technologies that build 3D parts layer by layer. A few of the more prominent AM technologies used to fabricate truss structures include fused deposition modeling (FDM) [49], selective laser sintering (SLS) [65], electron beam melting (EBM) [7, 47], and stereolithography (SLA) [66]. Some of the most notable developments in recent years have been in Ti-alloy trusses, produced by selective EBM of fine alloy powders, for biomedical implants [9, 34, 37, 38]. In another arena, direct laser writing by optical lithography has been used to fabricate polymer truss structures with extremely fine-scale features, for potential use in photonic applications [2, 3]. Currently, build volumes of commercial AM systems typically range from $0.001\,\mathrm{m}^3$ to $1\,\mathrm{m}^3$. Sub-mm minimum feature sizes and print resolutions of tens of µm are now routinely achieved. Therefore, in addition to enabling fabrication of even the most complex trusses, AM allows fine control of structural features and tailoring local geometries in ways that were heretofore unimaginable.

Although these technologies allow complex trusses to be fabricated, the mechanical properties of the manufactured trusses are often lower than theoretical predictions due to defects in the manufactured trusses that are not included in the models [6, 46, 52]. The extent to which defects degrade mechanical properties can be consid-

ered in terms of the stability of deformation as localized failure events accumulate. When the load-bearing capacity is dictated by elastic buckling of a family of struts that are equally strained, the macroscopic truss strength is dictated by the volume-averaged strut stress once all struts have buckled. Because the stress needed for continued buckling of an elastic strut is constant (*i.e.* the compressive response is essentially elastic, perfectly-plastic), a premature buckling event caused by a structural imperfection does not affect the ultimate truss strength. Analogously, in cases where the strut slenderness ratio is small and the nodal regions are augmented to mitigate the area reduction caused by strut overlap, the truss strength is dictated by the material yield strength and the load bearing area of all struts. Here, again, local structural defects or stress concentrations that may cause localized yielding should not affect truss strength. These represent best-case scenarios.

In an alternative scenario, where the material is relatively brittle and its strength follows weakest-link scaling laws, strut fracture is expected to be stochastic and controlled by extreme values in the stress distribution and the volumes over which such stresses persist. For example, local stress elevations due to structural defects may cause local fracture, leading to load shedding and potentially additional fracture events in neighboring regions. In one limit, where the truss is comprised of only a small number of unit cells (and hence a small number of struts), the first strut fracture

event may lead to instability and catastrophic truss failure. The truss strength would therefore be inherently stochastic. Conversely, if the macroscopic structural dimensions greatly exceed the unit cell dimensions and the truss is designed to exhibit some degree of damage tolerance (*i.e.* toughness), a single localized failure event may not be critical to structural stability.

An additional consideration is the effects of free surfaces. Nodal connectivities of struts that terminate at external boundaries are lower than those in the bulk. Consequently, near-boundary stiffness and strength may differ from the corresponding bulk properties. The effect persists to a depth that scales with strut length and depends sensitively on truss topology.

Effects of boundaries on elastic properties of truss structures have been studied through finite element calculations of large aggregates of unit cells [19, 35] and through novel application of Bloch wave theory [44]. Studies on 2-dimensional elastically-isotropic trusses have shown that, in fully triangulated and hexagonal structures, the thickness of the elastic boundary layer is comparable to the strut length and the layer has negligible influence on the elastic properties of finite-sized structures. In contrast, the 2-dimensional regular Kagome structure (which is also elastically isotropic) exhibits a thick boundary layer when loaded in certain directions; the thickness of this layer is inversely propertional to truss relative density.

The effect is a manifestation of the transition from a stretch-dominated mode of deformation in the bulk to combined bending and stretching along some boundary planes. Interestingly, when long cracks are present, boundary effects in the latter case cause a reduction in crack tip stresses and lead to an unusually high fracture toughness [19]. Computational studies on 3-dimensional octet trusses have similarly shown that the boundary layer is negligible [35] and that the stiffness and compressive buckling strength are independent of truss size [32]. Notwithstanding, we show in subsequent chapters that important boundary effects occur along the *edges* of trusses. Although benign with respect to global elastic response, the effects play a crucial role in compressive failure when the strut material has limited ductility.

1.1 Dissertation objectives and outline

The overarching goals of this work are two-fold: (i) to develop a set of conventions that yield unambiguous descriptions of structure types and (ii) to use this framework to identify trusses that are stiff, strong and defect tolerant. The former employs concepts from crystallography and geometry to describe nodal locations and connectivity of struts. The latter is accomplished using a combination of finite element simulations and experimental tests. FE simulations are used to predict the mechanical

properties of potential structures, and experimental tests measure the performance of manufactured trusses and serve as a comparison to the models. Together, these results are used to inform future truss designs.

The dissertation is organized in the following manner. A taxonomy of truss structure is formalized in Chapter 2. This framework is used to identify trusses that are stiff and that possess high strength in Chapter 3. Two isotropic binary compound trusses and many isotropic ternary trusses are identified, all with Youngs moduli equal to the maximal possible value for isotropic strut-based structures. In Chapter 4, experimental tests are used to measure the performance of additively manufactured trusses. Two coupled aspects of truss design and performance are addressed: (i) the extent to which circular nodal fillets enhance node stiffness and alleviate stress concentrations, and (ii) the extent to which external boundaries affect local strut strains. In Chapter 5, finite element simulations are used to to determine the extent to which individual strut defects and free surfaces, both separately and together, elevate strains in neighboring struts and, in turn, the effects of strain elevations on truss strength. Finally, in Chapter 6 key findings are summarized, and opportunities for future work are discussed.

Chapter 2

Periodic truss structures

2.1 Introduction

Despite the broad recognition of the potential of periodic trusses for use in many diverse fields of technology, there are no widely-accepted descriptors of their structure. In the numerous articles on this topic that have appeared in the past two decades, the terminology has been based loosely on descriptions of various polyhedra, but often without explicit connections between truss structure and specific characteristics of the reference polyhedron.

For example, trusses designated as pyramidal are conceptually constructed by placing struts along the four edges of a regular square pyramid at which the triangular faces intersect, but not along the edges of the square base [18, 59]. Similarly, tetrahedral trusses are formed by placing struts along three non-coplanar edges of a tetrahedron, but not on the other three edges [48, 59]. In other cases, truss structures are constructed by placing struts normal to and at the center of each face of the reference polyhedron (not along the edges), *e.g.* the truncated octahedral truss [22, 30]. Elsewhere, truss structures have been described as being "tetrahedral with three-fold symmetry" or "tetrahedral with six-fold symmetry", without explicit designations of strut locations [28].

In some instances, new words have been devised to describe truss structure. The octet truss, for example, derives from a combination of octahedral and tetrahedral. Here struts are placed along all edges of a series of regular octahedra and tetrahedral arranged to fill three-dimensional space [12]. Other truss structures have been described loosely as "fully triangulated", "bulk cross" [29], "cross I symmetric", "G6", "G7", "dode-thin", and "hatched" [9, 38]. These and the preceding designations are re-visited in a later section of this article.

In addition to the vagaries introduced by using polyhedra as the basis of truss designations, the terminology fails to recognize the fundamentally different nature

11

of polyhedra and of trusses. A polyhedron is a three-dimensional solid whose outer boundaries are defined by plane polygons such that the edge of each polygon belongs to one other polygon. A truss, on the other hand, consists of a set of points (or nodal locations) and a set of lines (or struts) joining certain points. Solid geometry alone lacks the structure needed to completely and unambiguously describe truss structure.

Descriptions of trusses have also frequently invoked terms derived from the field of crystallography. Examples include "body centered cubic" and "diamond". Indeed, the association between nodal positions of trusses and space lattices in crystallography has led to the characterization of trusses as lattice materials, lattice structures or simply lattices. In addition to the unfortunate conflict with the definitions of lattices in the context of crystallography, the terminology (again) fails to recognize the fundamental differences between space lattices and truss structure: A space lattice defines only an array of regularly-spaced points and provides no information about the connectivity of those points (*i.e.* topology). Therefore, crystallography alone (like solid geometry) lacks the structure needed to describe truss structure.

2.2 Elements of a new language

The principal objective of the article is to present a framework within which trusses can be systematically described and classified. This requires a set of conventions and terminology that, when applied in a consistent manner, yields concise yet unambiguous descriptions of structure types and of specific truss designs. In turn, this goal requires a language of truss structure. As with any language whether expressed by words in a spoken language or by symbols in mathematics or music the language of truss structure must have three hierarchical elements: (i) a lexicon of the smallest distinct meaningful elements (or morphemes); (ii) a grammatical system by which the morphemes are combined to form the smallest elements that, in isolation, have practical meaning (*i.e.* words); and (iii) a syntax, or a set of rules by which the ordering of elements is used to convey complex ideas (*i.e.* sentences). The key elements of the proposed language of truss structure are summarized in Table 2.1 and detailed in due course. Although seemingly short, the language is capable of describing the many truss structures of current scientific and technological interest.

The language of truss structure is derived from logical descriptors of both the nodal points in space and the connectivity of those points by struts. These descriptors and their organization form the basis for the conventions of the language.

The fundamental bases of the proposed conventions and associated terminology are fourfold:

(i) An elementary cubic truss is constructed by joining nearest-neighbor points of one of the three cubic space lattices with struts.

(ii) An elementary non-cubic truss is constructed by applying an affine deformation to an elementary cubic truss such that the new nodal locations exhibit symmetry of a different space lattice.

(iii) A compound truss is constructed by combining two different trusses on a single space lattice, with specified scaling, translational and orientational relationships and that have matching nodes.

(iv) Complex trusses are constructed by either assigning two or more nodes to each lattice point and then joining nearest-neighbor nodes with struts, or by assembling a number of truss sub-cells to form a super-cell and tiling that super-cell in space.

Hereafter, structure types are denoted by {...}, affine (non-distortional) deformations by a stretch vector $\langle \lambda_x \, \lambda_y \, \lambda_z \rangle$, translational shifts in origin by $[u \, v \, w]$, rotational transformations about the principal axes by $(\theta_x \, \theta_y \, \theta_z)$, and nodal locations at a lattice point by $\lfloor p \, q \, r \rfloor$. Specific truss configurations further include numerical values

14

n within {...} to indicate the number of unit cells and superscripts β on {...} that denote the number of directions in which the truss is tiled in space (1, 2 or 3). Unlike crystallography, where the concepts are predicated on the notion of an infinite array of repeating unit cells, the classification system presented here is not restricted to infinite systems; it naturally allows for the presence of free "boundaries".

The conventions and terminology are introduced and developed through a series of illustrative examples of progressively increasing complexity; generalizations of the resulting framework and taxonomy are presented afterwards. The hierarchy of the classification system and its conceptual evolution are depicted in Fig. 2.1. The system begins with elementary cubic trusses (at the center of the figure) and increases in complexity with the introduction of non-cubic and compound trusses and, finally, with complex trusses. The taxonomy is then applied to the descriptions of structure types employed in various science and engineering fields. The merits of one particular compound truss are assessed by comparing the elastic properties of the compound truss with those of the octet truss.

2.3 Development of the language of truss structure

In the present context, trusses are defined as arrays of straight, interconnected struts with periodic character. They can comprise few (large) repeating units, as found in structural engineering, or aggregates of many (small) repeating cells that, collectively, behave essentially as a material. Their structure is defined completely by: (i) the positions of all nodes in space, and (ii) the connectivity of the nodes by struts. Details of node geometry, strut cross-section, strut waviness and other geometric features and defects are not considered.

2.3.1 Elementary cubic trusses

By our definition, an elementary cubic truss is constructed by joining pairs of (only) nearest-neighbor points of one of the three cubic space lattices by struts. The complete set of elementary truss types constructed in this manner is illustrated in Fig. 2.2. The three structure types are denoted simple cubic, $\{SC\}$, body-centered cubic, $\{BCC\}$, and face-centered cubic, $\{FCC\}$. (Here the structure types, indicated by $\{...\}$ brackets, are distinct from those of lattices or crystals.) Any number of unit cells of one truss type, connected at the cell faces, can be tiled to form a truss. The

three specific trusses in Fig. 2.2 consist of $2 \times 2 \times 2$ arrays of unit cells of $\{SC\}$, $\{BCC\}$ and $\{FCC\}$ trusses; accordingly, they are denoted $\{2SC\}^3$, $\{2BCC\}^3$ and $\{2FCC\}^3$. Here the superscript (3) on $\{...\}$ indicates the number of directions in which the trusses are tiled in space and the numerical value within the $\{...\}$ brackets indicates the number of unit cells in each direction.

The unit cells can be arranged in other ways, to form rectangular (generally non-cubic) prisms. For example, a $2 \times 5 \times 5$ array of $\{SC\}$ cells could be expressed as $2\{5\{5SC\}\}$ or, more compactly, as $2\{5SC\}^2$, *i.e.* two layers of a 5×5 array of $\{SC\}$ cells. As another example, a $2 \times 3 \times 6$ array would be $2\{3\{6SC\}\}$.

In the preceding construction, struts are not placed between non-nearest-neighbor points on the space lattice. Doing so, in some cases, would lead to strut intersections. The problem can be visualized with the $\{SC\}$ truss; struts added between second nearest-neighbors — along the face diagonals — would intersect at the face centers. Although in principle the problem could be rectified by introducing new lattice points at the intersections, the process would alter the space lattice and unnecessarily complicate the truss description. Moreover, the trusses that would emerge through this procedure would not be unique; they could be constructed by other routes, *e.g.* via the compound trusses described below.

As with their crystallographic counterparts, each unit cell of an infinite array of

17

the three elementary trusses contains a characteristic number, j_o, of lattice points: $j_o = 1$ for $\{SC\}$, $j_o = 2$ for $\{BCC\}$ and $j_o = 4$ for $\{FCC\}$. By analogy — but now going beyond the realm of crystallography — each unit cell of that infinite array contains a characteristic number, b_o, of struts. For example, in an infinite $\{SC\}$ truss, there are 12 struts per cell, each shared by four adjoining cells, for a net of $b_o = 3$ struts per cell. Each strut is of length $l = a$ where a is the edge length of the unit cell (analogous to the lattice parameter in crystallography). In $\{BCC\}$ trusses there are eight struts per unit cell, each starting at the body center and radiating to one of the eight corners, all wholly contained within that cell; thus $b_o = 8$. The strut length is $l = 3\sqrt{a/2}$. In an $\{FCC\}$ cell, there are 12 struts connecting the six face centers, all wholly contained within that cell. There are also four struts joining each face center to the four corners on each of the six cube faces; since each of the latter struts is shared by two adjoining unit cells, collectively they net a total of 12 struts per cell. Combining with the ones joining the face centers yields a total of $b_o = 24$ struts. Each has a length of $a/\sqrt{2}$.

Analogous procedures are used to determine the number of struts b and lattice points j for systems of finite size. Consider for example multiple unit cells of an elementary truss arranged either as a line of n cells (joined at their faces), as a square array of $n \times n$ cells, or as a cubic array of $n \times n \times n$ cells. The $\{SC\}$ trusses

thus produced are denoted $\{nSC\}^1$, $\{nSC\}^2$ and $\{nSC\}^3$. Analogous terminology would be used to describe $\{BCC\}$ and $\{FCC\}$ trusses constructed in this manner. General results for b and j of finite trusses are obtained from geometry and are expressed by the simple formulae in Table 2.2.

A key characteristic of truss topology is the connectivity, Z, defined as the average number of struts meeting at each node. Since each strut ends at two nodes, the average connectivity is $Z = 2b/j$. For infinite trusses, $Z = Z_o = 2b_o/j_o$. The latter takes on values of $Z_o = 6$, 8 and 12 for $\{SC\}$, $\{BCC\}$ and $\{FCC\}$ trusses, respectively. For linear, square and cubic arrays of finite size, the connectivity can be calculated using the expressions for b and j in Table 2.2.

Truss geometry is further characterized by the relative density (or volume fraction) ρ of strut material within the volume defined by the external boundaries of the truss. When the strut radius r is small in comparison to the strut length l, the relative density of a unit cell (contained within an infinite truss) is given by $\rho = \rho_o = \pi b_o (r/a)^2 (l/a)$. Expressions for ρ for systems of finite size have also been derived and are presented in Table 2.2.

2.3.2 Compound cubic trusses

Deficiencies in connectivity of elementary trusses (discussed below) can be rectified by combining dissimilar elementary trusses to form compound cubic trusses. For example, combining a $\{2BCC\}^3$ truss and a $\{2SC\}^3$ truss — both residing in the same Cartesian coordinate system with the same origin and the same unit cell edge length — yields the compound truss $\{2BCC\}^3|\{2SC\}^3$ (Fig. 2.3(a)). (The vertical line is used to indicate that information on either side pertains to different constituent trusses.) If all strut radii are the same, the relative density of the compound truss is simply the additive sum of the relative densities of the constituent trusses. For example, for an infinite truss of the structure type $\{BCC\}|\{SC\}$, the relative density is $\rho_o = (4\sqrt{3}+3)\pi(r/a)^2$. Similarly, the number of struts is the sum of those in the constituent trusses, $i.e.$ $b_o = 3 + 8 = 11$. In contrast, the number of nodes j_o is not additive. Instead, it is greater of the two values of j_o of the two trusses, $i.e.$ $j_o = j_o^{\{BCC\}} = 2$. Consequently, the average connectivity is $Z_o = 2b_o/j_o = 11$. But the connectivity is not the same at each node: $Z_o = 8$ for half of the nodes (at the body centers) and $Z_o = 14$ for the other half (at the body corners).

Recognizing that only half of all lattice points of the $\{2BCC\}^3$ truss are used in the construction of the $\{2SC\}^3$ truss, a second SC truss with the same edge length could be added. It would differ from the first only in that its origin would reside at the

20

position $[^1/_2 \, ^1/_2 \, ^1/_2]$ (in units of edge length). But, because of the constraints set by the size of the parent truss, only one such unit cell could be added; additional struts emanating from this truss would extend beyond the external boundaries of the parent truss. This particular compound truss is denoted $\{2BCC\}^3|\{2SC\}^3|\{SC\} \, [^1/_2 \, ^1/_2 \, ^1/_2]$ (Fig. 2.3(b)). The latter part of the designation indicates that the origin of the last in the series of constituent trusses, notably $\{SC\}$, is shifted by $[u \, v \, w] = [^1/_2 \, ^1/_2 \, ^1/_2]$ with respect to the origin of the parent $\{BCC\}$ truss. Similarly, large trusses of this type (with $n \gg 1$) would be denoted $\{nBCC\}^3|\{nSC\}^3|\{(n-1)SC\} \, [^1/_2 \, ^1/_2 \, ^1/_2]$. The structure type is $\{BCC\}|\{SC\}|\{SC\} \, [^1/_2 \, ^1/_2 \, ^1/_2]$. Values of Z_o for these and other structure types are given in Table 2.3.

Another example of a compound truss, $\{2FCC\}^3|\{2SC\}^3$, is shown in Fig. 2.3(c). Here, again, the constituent elementary trusses share a common coordinate system and origin. Although the $\{SC\}$ truss does not occupy all of the nodes defined by the $\{FCC\}$ truss, a third unit cell (*e.g.*, a second $\{SC\}$ truss) cannot be introduced into the existing $\{2FCC\}^3|\{2SC\}^3$ truss without producing strut intersections. For this structure type — $\{FCC\}|\{SC\}$ — ρ_o and b_o are additive ($\rho_o = (12\sqrt{2} + 3)\pi(r/a)^2$ and $b_o = 27$), $j_o = 4$ (that for $\{FCC\}$) and the average connectivity is $Z_o = 13.5$.

Yet another example of a compound cubic truss, $\{2FCC\}^3|\{2BCC\}^3$, is shown in Fig. 2.3(d). As in the preceding example, no more than one of each of the

21

two truss types can be combined without producing strut intersections. For the $\{FCC\}|\{BCC\}$ structure type, ρ_o and b_o are (again) additive: $\rho_o = (12\sqrt{2} + 4\sqrt{3})\pi(r/a)^2$ and $b_o = 32$. But, because the $\{BCC\}$ contributes one additional node at the body center of each cell (not present in the parent $\{FCC\}$ truss), the number of nodes is $j_o = 5$ and the connectivity is $Z_o = 12.8$.

A variant on the $\{2FCC\}^3|\{2SC\}^3$ compound truss is shown in Fig. 2.4(a). It comprises a $2\times2\times2$ array of $\{SC\}$ cells with edge length a and one $\{FCC\}$ cell with the same origin but with twice the edge length $(2a)$. Conceptually, the $\{FCC\}$ cell is produced by scaling the edge lengths of the parent $\{FCC\}$ truss by a stretch ratio vector $\langle \lambda_x \, \lambda_y \, \lambda_z \rangle = \langle 2\,2\,2 \rangle$. The truss is therefore denoted $\{2SC\}^3|\{FCC\}\langle 2\,2\,2 \rangle$. It represents a cubic supercell that can be duplicated and tiled in space to make larger trusses. Its structure type is $\{2SC\}^3|\{FCC\}\langle 2\,2\,2 \rangle$. By analogy to superlattices in compound crystals, such collections are called supertrusses. Five other cubic supertrusses are shown in Fig. 2.4: $\{2SC\}^3|\{BCC\}\langle 2\,2\,2 \rangle$, $\{2SC\}^3|\{FCC\}\langle 2\,2\,2 \rangle$, $\{2FCC\}^3|\{SC\}\langle 2\,2\,2 \rangle$, $\{2FCC\}^3|\{BCC\}\langle 2\,2\,2 \rangle$, $\{2BCC\}^3|\{FCC\}\langle 2\,2\,2 \rangle$ and $\{2BCC\}^3|\{SC\}\langle 2\,2\,2 \rangle$

2.3.3 Non-cubic trusses

An elementary non-cubic truss is constructed by applying an affine deformation to an elementary cubic truss. (This procedure differs from first identifying a non-cubic space lattice and then joining lattice points. In the latter scenario, joining only nearest-neighbor points with struts would generally lead to a non-contiguous truss.) Two examples are shown in Fig. 2.5. The first is simple orthorhombic $\{SO\}$. Here the inter-axis angles are 90° and the edge lengths along the three principal directions differ. It is derived from a $\{SC\}$ truss through stretching/compressing operations in two of the three principal directions, say y and z, $e.g.$ $\langle \lambda_x \, \lambda_y \, \lambda_z \rangle = \langle 1 \, 1.2 \, 1.5 \rangle$. This particular truss is denoted $\{2SO\}^2 \langle 1 1.2 1.5 \rangle$ and its structure type is $\{SO\}\langle \lambda_x \, \lambda_y \, \lambda_z \rangle$.

Because an affine deformation does not alter truss topology, b_o, j_o and Z_o are the same as those of the parent $\{SC\}$ truss. The relative density, being a characteristic of geometry (not topology), differs. It is readily obtained from geometry.

The second is body-centered orthorhombic $\{BCO\}$, constructed by applying two stretching/compressing operations to a $\{BCC\}$ truss. If the stretch ratio vector is again taken to be $\langle \lambda_x \, \lambda_y \, \lambda_z \rangle = \langle 1 \, 1.2 \, 1.5 \rangle$, the resulting truss would be $\{2BCO\}^2 \langle 1 \, 1.2 \, 1.5 \rangle$. Four other non-cubic structure types with orthogonal axes are possible: face-centered orthorhombic, $\{FCO\}$, body-centered tetragonal, $\{BCT\}$,

simple tetragonal, $\{ST\}$, and face-centered tetragonal $\{FCT\}$. Here, again, b_o, j_o and Z_o are the same as those of the parent truss. Excluding trusses with non-orthogonal axes, the preceding list of (six) elementary non-cubic structure types is comprehensive.[1]

Elementary non-cubic trusses can be combined to form compound non-cubic trusses. For example, combining the $\{2SO\}^2\langle 1 \ 1.2 \ 1.5\rangle$ with the $\{2BCO\}^2\langle 1 \ 1.2 \ 1.5\rangle$ yields the truss shown in Fig. 2.5(c) and denoted $\{2SO\}^2\langle 1 \ 1.2 \ 1.5\rangle | \{2BCO\}^2\langle 1 \ 1.2 \ 1.5\rangle$. The coordinate axes and the origins of the two trusses are the same.

Elementary non-cubic trusses can also be combined to form compound non-cubic supertrusses. For example, combining one $\{2BCO\}^2\langle 1 \ 1.2 \ 1.5\rangle$ truss with one $\{2SO\}^2\langle 2 \ 2.4 \ 3\rangle$ truss yields $\{2BCO\}^2\langle 1 \ 1.2 \ 1.5\rangle | \{2SO\}^2\langle 2 \ 2.4 \ 3\rangle$ (Fig. 2.5(d)). Both stretch vectors are referenced to the dimensions of the baseline cubic truss.

Other non-cubic trusses can be formed by applying affine shear deformations to the preceding trusses. One example is the rhombohedral truss, $\{R\}$. The rhombohedral truss is of interest for two reasons: (i) it can be readily made by the SPPC process [26, 27, 28] and (ii) it forms the basis for the Kagome truss (described below).

_____

[1]In comparing the list of elementary trusses that have orthogonal axes to the list of Bravais space lattices that also have orthogonal axes, we find that one of the space lattices — notably, base-centered orthorhombic — does not have a truss counterpart.

Conceptually, it is formed by stretching a $\{SC\}$ truss along the cube diagonal while maintaining constant strut lengths. In doing so, the inter-axis angles decrease below 90°. An example is shown in Fig. 2.5(e). The structure type is denoted $\{R\}\langle\lambda_{111}\rangle$ where $\langle\lambda_{111}\rangle$ represents the stretch ratio along the body diagonal. When $\langle\lambda_{111}\rangle = \sqrt{2}$, the three inter-axis angles are 60°.

A compound rhombohedral truss can be constructed by combining two identical rhombohedral trusses with one rotated about the body diagonal by $\pi/3$. The structure type could be denoted $\{R\}\langle\lambda_{111}\rangle|\{R\}\langle\lambda_{111}\rangle(\theta_{111} = \pi/3)$, where θ_{111} is the rotation angle of the second constituent truss, or, more compactly, as $\{R(\theta_{111} = 0, \pi/3)\}\langle\lambda_{111}\rangle$ (Fig. 2.5(f)). Here the truss type designation R is followed by the two rotation angles, all contained within the { } brackets. Compound trusses of this kind have previously been fabricated by SPPC [28].

Although many other non-cubic trusses could be constructed by applying shear deformations to simpler trusses, the merits of doing so are presently unclear. In most cases the resulting trusses would exhibit low degrees of symmetry and complex shear/normal coupling of stresses and strains. Whether these can be exploited in a useful way in load-bearing systems remains to be established.

Yet other types of compound non-cubic trusses can be constructed by combining 2D planar trusses with 3D trusses. Conceptually, 2D trusses are constructed by join-

ing nearest neighbor points on a planar (rather than space) lattice with struts. For example, the 2D analogs to $\{SC\}$ and $\{ST\}$ (3D) trusses are square $\{Sq\}$ and rectangular $\{Re\}$, respectively. Two examples of compound 2D/3D trusses are shown in Fig. 2.6. In the first, a $\{2BCC\}^3$ truss (from Fig. 2.2(b)) is combined with two square trusses, one on each of two opposing faces. The compound layered truss is denoted $\{2Sq\}^2|\{2BCC\}^3|\{2Sq\}^2$ and its structure type is $\{Sq\}|\{BCC\}|\{Sq\}$ Although in this case the two trusses share common edge lengths and coordinate systems, various scalings, translations and rotations can also be employed. Trusses of this type, with planar trusses on the two external faces of a 3D truss, have been considered for use as stiff, lightweight "sandwich" panels: the 2D trusses serving as the panel faces and the 3D truss as the core. A variant is produced by inserting a third square truss along the mid-plane [64]. This yields a $\{2Sq\}^2|\{2BCC\}^2|\{2Sq\}^2|\{2BCC\}^2|\{2Sq\}^2$ truss.

2.3.4 Complex trusses

More complex trusses can be constructed following one of two approaches. In the first, two or more nodes are assigned to each point of a space lattice and struts are then placed between nearest-neighbor nodal locations. (The analogy in crystallography is the construction of a crystal structure by placing atom motifs at each point of

a space lattice.) Two particular structures of this type have received attention over the years: the diamond cubic truss [21, 31] and the Kagome truss [12].

The diamond cubic crystal structure is based upon an FCC space lattice with two atoms at each lattice point: at $\lfloor 000 \rfloor$ and $\lfloor {}^1\!/_4 \, {}^1\!/_4 \, {}^1\!/_4 \rfloor$ with respect to the origin of the lattice and at corresponding points following face-centering translations. (Note the use of $\lfloor \; \rfloor$ brackets to denote atomic positions at a lattice point) Nodal locations of a diamond cubic truss are defined in the same way. That is, two nodes are assigned to each point of an FCC lattice, at $\lfloor 000 \rfloor$ and $\lfloor {}^1\!/_4 \, {}^1\!/_4 \, {}^1\!/_4 \rfloor$. The truss is formed by joining the nearest-neighbor nodes with struts. The resulting truss comprises tetrahedral-like sub-units[2] with four struts meeting at each node and each strut making an angle of 109.5° to each of the other struts (Fig. 2.7(a)). The structure type is denoted $\{FCC\lfloor 0\,0\,0 \rfloor \lfloor {}^1\!/_4 \, {}^1\!/_4 \, {}^1\!/_4 \rfloor\}$. Here the space lattice designation, FCC, is followed by the two nodal locations associated with each lattice point, all contained within the $\{\,\}$ brackets. Its connectivity is $Z_o = 4$ at all nodes: the minimum possible value for a three-dimensional truss.

3D Kagome trusses are constructed in a similar way. This truss (Fig. 2.7(b)) is

---

[2]The tetrahedral designation comes from the fact that the four struts in each sub-unit are normal to the faces of a regular tetrahedron centered on the nodal point. In other contexts [59], the tetrahedral designation has been used to describe trusses in which the struts are coincident with the edges of a regular tetrahedron. The two resulting structures are vastly different from one another.

based upon a rhombohedral space lattice in which the three inter-axis angles are $60°$; the stretch ratio along the body diagonal needed to achieve this angle is $\lambda_{111} = \sqrt{2}$. Four nodes are assigned to each lattice point, at $\lfloor 000 \rfloor$, $\lfloor {}^1/_2 00 \rfloor$, $\lfloor 0 {}^1/_2 0 \rfloor$ and $\lfloor 00 {}^1/_2 \rfloor$. Once again, the truss is constructed by joining the nearest-neighbor nodes with struts. The resulting structure type is $\{ R \lfloor 000 \rfloor \lfloor {}^1/_2 00 \rfloor \lfloor 0 {}^1/_2 0 \rfloor \lfloor 00 {}^1/_2 \rfloor \} \langle \lambda_{111} = \sqrt{2} \rangle$. As with the preceding designation of the diamond cubic truss, the nodal locations associated with each lattice point are contained within the { } brackets.

In the second approach to constructing complex trusses, a super-cell is first constructed from an assemblage of two or more elementary sub-cells and the super-cell is then duplicated and tiled in three dimensions. (In this context, assemblage refers to a collection of sub-cells that are joined on their faces; it differs from a compound truss, wherein two or more constituent trusses are built on the same space lattice.) An illustrative example is a truss based on the rhombic dodecahedron.

The rhombic dodecahedron consists of 12 congruent faces, each in the shape of a rhombus in which the ratio of the long diagonal length to short diagonal length is $\sqrt{2}$. It is of interest because it is one of the few polyhedra with congruent faces that can be tiled to fill three-dimensional space. The truss is created by placing struts along each of the edges of the reference polyhedron (Fig. 2.7(c)). The resulting structure is equivalent to one-half of a $\{ BCC \}$ truss. Conceptually, it can be constructed by

alternating one $\{BCC\}$ cell with one vacant cubic cell in each of the three directions, in a 3D checkerboard pattern. The full unit cell comprises a $2 \times 2 \times 2$ array of sub-cells: four $\{BCC\}$ cells and four vacant cubes. The structure type is denoted $\{BCC\,[0\,0\,0]\,[0\,1\,1]\,[1\,0\,1]\,[1\,1\,0]\}$. The four translation vectors within the $\{\}$ brackets imply four families of $\{BCC\}$ trusses. Its packing density is $\rho_o = (3\sqrt{3}\pi/2)(r/l)^2$. Half of the nodes have connectivity $Z_o = 4$ and the other half have $Z_o = 8$; thus the average value is $\bar{Z}_o = 6$.

2.4 Generalizations of designations of trusses and structure types

Building upon the pattern established in the preceding examples, a generic terminology is readily developed. As demonstrated in a subsequent section, the terminology can be applied unambiguously to descriptions and classifications of periodic trusses. A summary of the taxonomy is presented in Table 2.3.

An elementary truss consisting of a linear, square or cubic array of cells is expressed generically as $\{nA\}^{\beta}$ where A is the truss type (SC, BCC or FCC), n is the number of unit cells in each row and β is the number of directions in which the truss is tiled (1, 2 or 3). The structure type is simply $\{A\}$. When combined

with the normalized strut radius r/a, the truss designation completely defines the structure and the geometry of an elementary truss. With these, all other important characteristics (b, j, Z, ρ) are known.

When the unit cells are arranged to form other types of rectangular (non-cubic) prisms, the trusses are expressed as $n_x\{n_y\{n_z A\}\}$ where n_x, n_y and n_z are the numbers of cells in the x, y and z directions, respectively. In cases where two of these quantities are equal, say $n_y = n_z$, the notation can be contracted to $n_x\{n_y A\}^2$.

An elementary non-cubic truss is expressed as $\{nA\}^\beta \langle \lambda_x\ \lambda_y\ \lambda_z \rangle$ where $\langle \lambda_x\ \lambda_y\ \lambda_z \rangle$ is the stretch vector required to transform the starting elementary cubic truss to the non-cubic truss $\{A\}$. The structure type is $\{A\}\langle \lambda_x\ \lambda_y\ \lambda_z \rangle$. Here, again, the truss designation along with r/a fully define truss structure and geometry. Shearing operations can also be applied; the pertinent strains would then be added to (or replace) the stretch vector.

A compound truss is described by a list of constituent trusses and their relationships with one another. The first truss in the list is the parent; it defines the size, shape and orientation of the system. The spatial extent of the trusses that follow in the list is restricted to that of the first. Each truss designation is followed, in order, by the stretch vector $\langle \lambda_x\ \lambda_y\ \lambda_z \rangle$, the translation vector $[u\ v\ w]$, and the rotations $(\theta_x\ \theta_y\ \theta_z)$ about the coordinate axes, all with respect to the cu-

bic parent. Since the parent truss defines orientation and position, both $[u\,v\,w]$ and $(\theta_x\,\theta_y\,\theta_z)$ for the parent are (usually) identically zero; the stretch vector $\langle\lambda_x\,\lambda_y\,\lambda_z\rangle$ is present only if the parent is non-cubic. When terms are absent, their values are implied to have no effect, *e.g.*, stretch values of unity or rotations of zero. This allows for short designations for simple trusses; additional details are pro- vided only when necessary. In general, a compound truss designation would read as

$$\{n^{(1)}A^{(1)}\}^{\beta}\langle\lambda_x^{(1)}\,\lambda_y^{(1)}\,\lambda_z^{(1)}\rangle\}|\{n^{(2)}A^{(2)}\}^{\beta}\langle\lambda_x^{(2)}\,\lambda_y^{(2)}\,\lambda_z^{(2)}\rangle\left[u^{(2)}\,v^{(2)}\,w^{(2)}\right]\left(\theta_x^{(2)}\,\theta_y^{(2)}\,\theta_z^{(2)}\right)|\ldots$$

where the superscripts (1), (2), ... denote truss family types. If both trusses are cubic, the structure type is $\{A^{(1)}\}|\{A^{(2)}\}$.

Compound cubic supertrusses are expressed as $\{2nA^{(1)}\}^{\beta}|\{nA^{(2)}\}^{\beta}\langle2\,2\,2\rangle$. The factor of 2 on the first truss indicates that the ratio of numbers of the two truss types must be 2^{β}; the stretch ratio $\langle2\,2\,2\rangle$ on the second truss indicates that the size ratio of the two unit cells is two. The structure type is $\{2A^{(1)}\}|\{A^{(2)}\}\langle2\,2\,2\rangle$. If deemed to be important, other size and number ratios as well as translations and rotations could be introduced.

More-complex trusses can be constructed by assigning multiple nodes to each lattice point and joining the nearest-neighbor nodes by struts. The structure type is $\{A\lfloor0\,0\,0\rfloor\lfloor p^{(2)}\,q^{(2)}\,r^{(2)}\rfloor\ldots\lfloor p^{(i)}\,q^{(i)}\,r^{(i)}\rfloor\}$ where $\lfloor p^{(i)}\,q^{(i)}\,r^{(i)}\rfloor$ represents the location of the ith node at each lattice point. Alternatively, a super-cell can be made from an

assemblage of elementary sub-cells and the super-cell duplicated and tiled in space. If all of the sub-cells are the same (apart from vacant cells), the structure type would be $\{A\,[0\,0\,0]\,\left[u^{(2)}\,v^{(2)}\,w^{(2)}\right]\ldots\left[u^{(i)}\,v^{(i)}\,w^{(i)}\right]\}$.

2.5   Applications

The many disparate truss designations introduced in prior literature can be concisely and unambiguously described using the present system of classification and taxonomy. For example, a pyramidal truss, which contains struts aligned along the four edges at which the triangular faces of a regular square pyramid intersect, is, in general, of the structure type $\{BCT\}\langle 1\,1\,\lambda_z\rangle$, where the base of the $\{BCT\}$ unit cell coincides with the pyramid base. From geometry, the stretch ratio (measured perpendicular to the pyramid base, or z-plane) is $\lambda_z = \sqrt{2}\tan\theta$ where θ is the angle between the triangle edges and the square base. (This structure type reduces to a $\{BCC\}$ for the special case in which $\lambda_z = 1$ and hence $\theta = \tan^1(1/\sqrt{2}) \approx 35.26°$). Two specific versions of these trusses have been described as "two-layer pyramidal" and "one-layer pyramidal" [24, 41]; they are, respectively, $\{nBCT\}^2\langle 1\,1\,\lambda_z\rangle$ and $1/2\{nBCT\}^2\langle 1\,1\,\lambda_z\rangle$. This structure has also been described as "octahedral-type" [28]. These and other structure types are summarized in Table 2.4.

Hierarchical truss designs based on the preceding structure have been synthesized [15]. They comprise a single-layer pyramidal truss and a fine scale "octahedral-type" truss. Despite the differing descriptions, both trusses are of the type $\{BCT\}\langle 1\ 1\ \lambda_z\rangle$. When combined, the two trusses form a supertruss of the type $\{BCT\}\langle 1\ 1\ \lambda_z\rangle|\{1/\alpha BCT\}\langle \alpha\ \alpha\ \alpha\lambda_z\rangle$ where α is the size ratio of the constituent trusses (large/small). The specific one reported in [15] is $5\{10nBCT\}^2\langle 1\ 1\ 1\lambda_z\rangle|1/2\{nBCT\}^2\langle 10\ 10\ 10\lambda_z\rangle$ with $\lambda_z \approx 3.7$. That is, it consists of 5 layers of a $10n \times 10n$ array of $\{BCT\}\langle 1\ 1\ 1\lambda_z\rangle$ cells and one half of the full thickness of an $n \times n$ array of $\{BCT\}\langle 10\ 10\ 10\lambda_z\rangle$ cells.

A tetrahedral truss, which has struts aligned along three non-coplanar edges of a regular tetrahedron, is of the type $\{R\}\langle\lambda_{111}\rangle$. When in the form of a single tetrahedral layer (typically used as cores within sandwich panels), the specific structure is $1/3\{nR\}^2\langle\lambda_{111}\rangle$, *i.e.* one third of the full thickness of an $n \times n$ array of $\{R\}\langle\lambda_{111}\rangle$ cells.

The octet truss, comprising struts along the edges of regular octahedra and tetrahedral [12], is simply $\{FCC\}$.

One class of trusses made by SPPC has been described as "tetrahedral with three-fold symmetry" [28]. This is also of the type $\{R\}\langle\lambda_{111}\rangle$. The specific designation depends on the pattern of apertures used for guiding the UV light into the monomer

bath and the axes of the three light beams. In the cases described by [26], the apertures are in a hexagonal pattern, the projections of the light beams on the mask are at 120° to one another, and each projection is aligned with one of the close-packed directions of the aperture array. As noted earlier, the resulting structure comprises three interlaced but not interconnected $\{R\}$ trusses. Taking the long axis of the rhombohedra to be aligned with the c-axis in a hexagonal coordinate system and using the three-index Miller notation, the structure type would be described as $\{R\,[0\,0\,0]\,[0\,1\,0]\,[1\,0\,0]\}\langle\lambda_{111}\rangle$.

A related class of trusses previously described as "tetrahedral with six-fold symmetry" are made in a similar manner but now with six (rather than three) light beams, each with its projection on the mask aligned with one of the six close-packed directions of the aperture array [28]. It would be denoted $\{R\,[0\,0\,0]\,[0\,1\,0]\,[1\,0\,0]\}(\theta_{111}=0,\pi/3)\langle\lambda_{111}\rangle$ where θ_{111} is the rotation about the body diagonal. The two rotations, $\theta_{111}=0$ and $\pi/3$, imply two families of trusses, each described in full by the contents in the preceding $\{\ \}$ brackets and each subjected to a stretch ratio λ_{111} along the body diagonal.

The structures being explored in the medical implant community are based on variants of $\{SC\}$ (*e.g.*, "cross I symmetric", "G6"), $\{BCC\}|\{Sq\}$ compound trusses ("G7"), or $\{BCC\,[0\,0\,0]\,[0\,1\,1]\,[1\,0\,1]\,[1\,1\,0]\}$ ("dode thin" or "rhombic dodecahe-

dral").

Sandwich panels with planar trusses as "face sheets" and 3D trusses as cores are also conveniently described as compound trusses. One example, previously described as "single layer pyramidal" [29] consists of a pyramidal core, specifically $1/2\{BCT\}^2\langle 1\ 1\ \lambda_z\rangle$, and square 2D trusses on each of the two faces. The structure type is $\{Sq\}|1/2\{BCT\}\langle 1\ 1\ \lambda_z\rangle|\{Sq\}$. The form of this designation, with planar trusses "book-ending" a 3D truss, indicates the plate-like character of the structure.

Another sandwich panel was previously described as being an octet truss plate [64]. It is, loosely, of the structure type $\{FCC\}$. But this designation alone is incomplete; it lacks information about the orientation of the truss with respect to the plane of the panel and does not explicitly acknowledge its plate-like character. The structure is best described in terms of its constituent elements: (i) the two faces, each comprising an equilateral triangular arrangement of struts, denoted $\{Tr\}$; and (ii) the central core, which is a tetrahedral truss and is denoted here as $1/3\{R\}\langle \lambda_{111} = \sqrt{2}\rangle$. Combining, the structure type of the sandwich panel becomes $\{Tr\}|1/3\{R\}\langle \lambda_{111} = \sqrt{2}\rangle|\{Tr\}$. Here, as in the preceding example, the form of the designation immediately marks the structure as being plate-like.

The final example comes from a recent theoretical study of the truss structure that yields the maximum stiffness while retaining isotropic elastic properties. The

truss is based on the regular truncated octahedron (also known as the Kelvin cell) [22]. This polyhedron has six square faces and eight regular hexagonal faces. The corresponding truss comprises 14 struts emanating from the center, each normal to one of the 14 faces. The structure can be broken down into two interlaced $\{SC\}$ trusses and one $\{BCC\}$ truss (Fig. 2.3(b)). It is equivalent to the compound truss $\{nBCC\}^3|\{nSC\}^3|\{(n-1)SC\}^3\,[^1\!/_2\,^1\!/_2\,^1\!/_2]$, introduced in Section 3.2. This structure type, $\{BCC\}|\{SC\}|\{SC\}\,[^1\!/_2\,^1\!/_2\,^1\!/_2]$, has also been referred to as "reinforced body-centered cubic" [43].

2.6   Merits of compounding trusses

To illustrate the merits of compound trusses, we compare the elastic properties of two truss types: $\{nFCC\}^3$ and $\{nBCC\}^3|\{nSC\}^3$. The latter consists of two elementary trusses that, on their own, act as mechanisms, but together produce a stiff structure.

The elastic properties were computed by finite element (FE) analysis. The FE mesh was created using linear Euler-Bernoulli beam elements, suitable for small-strain analyses with small rotations. The strut slenderness ratio, $l/2r$, was selected to be 25, the linear number of unit cells was $n = 25$, and the constituent elastic

properties were taken to be: Young's modulus, $E_o = 200$ GPa, and shear modulus, $Go = 80$ GPa. The strut connections at the nodes were taken to be rigid. Nodal displacements were applied in two configurations, subjecting the trusses to a state of uniaxial compression parallel to one of the principal truss directions (denoted 1) or pure shear (in the 1-2 plane). The reaction forces needed to maintain the prescribed nodal displacements on the external faces were computed and used to determine the global elastic constants: Young's modulus E_1, Poisson's ratio ν_{12}, and shear modulus G_{12}, as well as the elastic anisotropy parameter $\omega \equiv 2G_{12}(1 + \nu_{12})/E_1$ [39]. The results are summarized in Table 2.5. The FE results were also used to construct polar plots of the Young's modulus for all possible uniaxial loadings. Sections through these plots along (011) planes are shown in Fig. 2.8. (This plane contains directions along the body edge, the face diagonal and the body diagonal.) For reference, the theoretical upper bound ($E/\rho E_o = 1/6 \approx 0.167$) for isotropic trusses is also shown.

By comparison to the properties of the $\{nFCC\}^3$ truss, the Young's modulus of the compound truss is greater, its shear modulus is only slightly lower, and its anisotropy parameter ω is closer to unity. The higher degree of isotropy of the compound truss is also evident in the polar plot in Fig. 2.8; the Young's modulus of the compound truss falls in the narrow range of 0.161–0.170 (consistently close to the upper bound) whereas that of the $\{nFCC\}^3$ truss varies over the range 0.111–0.200.

Thus, for applications in which both high specific stiffness and isotropy are sought, the compound truss would be the preferred choice.

2.7   Concluding discussion

We have presented a system for classification and taxonomy of periodic truss structures. The system employs concepts from crystallography and geometry to describe nodal locations and connectivity of struts. The conventions and terminology yield concise yet unambiguous descriptions of structure types and of specific truss structures. The system captures a broad range of trusses that have been studied in various science and engineering fields and could be expanded to include structures with even greater complexity, going beyond the cases considered here. Additionally, the FE results demonstrate that the $\{nBCC\}^3|\{nSC\}^3$ compound truss exhibits elastic properties that rival those of $\{nFCC\}^3$, especially when isotropy is a determining factor.

Numerous trusses that have been studied in recent years do not appear to be particularly well-suited for use as stiff and strong lightweight structures on their own. Specifically, those based on the elementary structure types $\{SC\}$, $\{BCC\}$, $\{BCT\}$, $\{ST\}$ and $\{R\}$ exhibit mechanisms and would not be expected to be significantly

better than comparable stochastic foams. However, when combined with other structural elements, such as face sheets to make a sandwich panel, the additional constraints may, in some cases, suppress collapse modes and render the trusses stiff and strong. Examples include sandwich panels with truss cores of $1/2\{nBCT\}^2\langle 1\,1\,\lambda_z\rangle$ (single-layered pyramidal) or $1/3\{nR\}^2\langle 1\,1\,\lambda_z\rangle$ (tetrahedral). Their performance is attributable in part to the fact that all struts are affixed to both face sheets without any intervening nodes. By introducing additional nodes, the cores become progressively weaker, especially in the near-edge regions of the panels where the constraints are low. This would occur, for example, if a $1/2\{nBCT\}^2\langle 1\,1\,\lambda_z\rangle$ core were replaced with a $5\{nBCT\}^2\langle 1\,1\,\lambda_z\rangle$ core (with a proportionate ten-fold reduction in strut dimensions to preserve core thickness).

Finally, although the principal motivation for studying the elastic properties of the $\{nBCC\}^3|\{nSC\}^3$ truss was to ascertain the extent to which the deficiencies in the two constituent elementary trusses could be mitigated by compounding, we find that the compound truss is (coincidentally) closely related to the one that Gurtner and Durand [22] recently identified as the stiffest isotropic truss. In our terminology, the latter structure type is $\{BCC\}|\{SC\}|\{SC\}\,[^1/_2\,{}^1/_2\,{}^1/_2]$. It is a compound truss that naturally emerged from our classification system; a specific example is shown in Fig. 2.3(b). Interestingly, the somewhat simpler compound truss for which elas-

tic properties were calculated in the present study proves to be essentially as good as the stiffest isotropic truss, as evidenced by the polar plot of Young's modulus in Fig. 2.8. In light of these observations, one might expect that, by systematically stepping through and analyzing the finite number of structure types identified through the present classification system, optimal structures for prescribed mechanical and functional requirements could be ascertained in an expeditious manner.

Table 2.1: The language of truss structure.

Lexicon: smallest meaningful elements	
Operators:	{ }: truss designation; $\langle\,\rangle$: stretch vector; [ ]: translational shift; |: separation between trusses; ( ) rotational transformation; $\lfloor\,\rfloor$ nodal location
Variables:	λ: stretch ratio; u, v, w: translations; θ: rotation angle; p, q, r: nodes at lattice point; x, y, z: coordinate axes
Lattices:	SC: simple cubic; BCC: body-centered cubic; FCC: face-centered cubic; SO: simple orthorhombic; BCO: body-centered orthorhombic; ST: simple tetragonal; FCO: face-centered orthorhombic; BCT: body-centered tetragonal; FCT: face-centered tetragonal; R: rhombohedral

Grammar: Elementary trusses formed by combining smallest meaningful elements	
Cubic	$\{A\}$ where $A = SC$, BCC or FCC
Non-cubic:	$\{A\}\langle\lambda_x\,\lambda_y\,\lambda_z\rangle$ where $A = SO$, BCO, FCO, BCT or FCT
Arrays:	$\{nA\}^3$, $n_x\{n_yA\}^2$, $n_x\{n_y\{n_zA\}\}$ where n is the number of cells

Syntax: Rules on ordering in defining compound and complex structure types	
Compound cubic truss:	$\{A^{(1)}\}\|\{A^{(2)}\}$ (without translation/rotation)
	$\{A^{(1)}\}\|\{A^{(2)}\}\left[u^{(2)}\,v^{(2)}\,w^{(2)}\right]\left(\theta_x^{(2)}\,\theta_y^{(2)}\,\theta_z^{(2)}\right)$ (with translation/rotation)
Compound cubic supertruss:	$\{2A^{(1)}\}\|\{A^{(2)}\}\langle 2\,2\,2\rangle$ (without translation/rotation)
	$\{2A^{(1)}\}\|\{A^{(2)}\}\langle 2\,2\,2\rangle\left[u^{(2)}\,v^{(2)}\,w^{(2)}\right]\left(\theta_x^{(2)}\,\theta_y^{(2)}\,\theta_z^{(2)}\right)$ (with translation/rotation)
Compound non-cubic truss:	$\{A^{(1)}\}\langle\lambda_x^{(1)}\,\lambda_y^{(1)}\,\lambda_z^{(1)}\rangle\|\{A^{(2)}\}\langle\lambda_x^{(2)}\,\lambda_y^{(2)}\,\lambda_z^{(2)}\rangle$ (without translation/rotation)
	$\{A^{(1)}\}\langle\lambda_x^{(1)}\,\lambda_y^{(1)}\,\lambda_z^{(1)}\rangle\|\{A^{(2)}\}\langle\lambda_x^{(2)}\,\lambda_y^{(2)}\,\lambda_z^{(2)}\rangle\left[u^{(2)}\,v^{(2)}\,w^{(2)}\right]\left(\theta_x^{(2)}\,\theta_y^{(2)}\,\theta_z^{(2)}\right)$ (with translation/rotation)
Compound non-cubic supertruss:	$\{2A^{(1)}\}\langle\lambda_x\,\lambda_y\,\lambda_z\rangle\|\{A^{(2)}\}\langle 2\lambda_x\,2\lambda_y\,2\lambda_z\rangle$ (without translation/rotation)
	$\{2A^{(1)}\}\langle\lambda_x\,\lambda_y\,\lambda_z\rangle\|\{A^{(2)}\}\langle 2\lambda_x\,2\lambda_y\,2\lambda_z\rangle\left[u^{(2)}\,v^{(2)}\,w^{(2)}\right]\left(\theta_x^{(2)}\,\theta_y^{(2)}\,\theta_z^{(2)}\right)$ (with translation/rotation)
i translations of same truss type:	$\{A\,[0\,0\,0]\left[u^{(2)}\,v^{(2)}\,w^{(2)}\right]\ldots\left[u^{(i)}\,v^{(i)}\,w^{(i)}\right]\}$
i nodes at lattice points:	$\{A\lfloor 0\,0\,0\rfloor\left[p^{(2)}\,q^{(2)}\,r^{(2)}\right]\ldots\left[p^{(i)}\,q^{(i)}\,r^{(i)}\right]\}$

Table 2.2: Geometric characteristics of linear, square and cubic arrays of elementary trusses of finite size.

	$\{SC\}$	$\{BCC\}$	$\{FCC\}$
Linear array of n cells	$b = 8n + 4$ $j = 4n + 4$ $\rho = \pi \left(\frac{r}{a}\right)^2 \left(8 + \frac{4}{n}\right)$	$b = 8n$ $j = 5n + 4$ $\rho = 4\sqrt{3}\pi \left(\frac{r}{a}\right)^2$	$b = 32n + 4$ $j = 9n + 5$ $\rho = \frac{\pi}{\sqrt{2}} \left(\frac{r}{a}\right)^2 \left(32 + \frac{4}{n}\right)$
Square $n \times n$ array	$b = 5n^2 + 6n + 1$ $j = 2\left(1 + n\right)^2$ $\rho = \pi \left(\frac{r}{a}\right)^2 \left(5 + \frac{6}{n} + \frac{1}{n^2}\right)$	$b = 8n^2$ $j = 3n^3 + 4n + 2$ $\rho = 4\sqrt{3}\pi \left(\frac{r}{a}\right)^2$	$28n^2 + 8n$ $j = 6n^2 + 6n + 2$ $\rho = \frac{\pi}{\sqrt{2}} \left(\frac{r}{a}\right)^2 \left(28 + \frac{8}{n}\right)$
Cubic $n \times n \times n$ array	$b = 3n\left(1 + n\right)^2$ $j = \left(1 + n\right)^3$ $\rho = \pi \left(\frac{r}{a}\right)^2 \left(3 + \frac{6}{n} + \frac{3}{n^2}\right)$	$b = 8n^3$ $j = \left(1 + 2n\right)\left(1 + n + n^2\right)$ $\rho = 4\sqrt{3}\pi \left(\frac{r}{a}\right)^2$	$b = 12n^2\left(1 + 2n\right)$ $j = \left(1 + n\right)\left(1 + 2n + 4n^2\right)$ $\rho = \frac{\pi}{\sqrt{2}} \left(\frac{r}{a}\right)^2 \left(24 + \frac{12}{n}\right)$

Table 2.3: A summary of structure types.

System	Truss family	Structure type	Z_o
Cubic	Elementary [a]	{SC}	6
		{BCC}	8
		{FCC}	12
	Compound [a]	{BCC}|{SC}	11
		{BCC}|{SC}|{SC} [½ ½ ½]	14
		{FCC}|{BCC}	12 ⅘
		{FCC}|{SC}	13 ½
	Compound supertruss [a,b]	{2SC}|{FCC} ⟨2 2 2⟩	12
		{2SC}|{BCC} ⟨2 2 2⟩	8
		{2FCC}|{SC} ⟨2 2 2⟩	12 ³⁄₁₆
		{2FCC}|{BCC} ⟨2 2 2⟩	12 ½
		{2BCC}|{FCC} ⟨2 2 2⟩	14 ⅔
		{2BCC}|{SC} ⟨2 2 2⟩	11 ⅙
Non-cubic	Elementary [a,c]	{SO} ⟨$\lambda_x \lambda_y \lambda_z$⟩	6
		{BCO} ⟨$\lambda_x \lambda_y \lambda_z$⟩	8
		{FCO} ⟨$\lambda_x \lambda_y \lambda_z$⟩	12
		{ST} ⟨$\lambda_x \lambda_y \lambda_z$⟩	6
		{BCT} ⟨$\lambda_x \lambda_y \lambda_z$⟩	8
		{FCT} ⟨$\lambda_x \lambda_y \lambda_z$⟩	12
		{R} ⟨λ_{111}⟩	6
	Compound [d]	{$A^{(1)}$} ⟨$\lambda_x^{(1)}\lambda_y^{(1)}\lambda_z^{(1)}$⟩ | {$A^{(2)}$} ⟨$\lambda_x^{(2)}\lambda_y^{(2)}\lambda_z^{(2)}$⟩	
	Compound supertruss [d]	{$2A^{(1)}$} ⟨$\lambda_x \lambda_y \lambda_z$⟩ | {$A^{(2)}$} ⟨$2\lambda_x\, 2\lambda_y\, 2\lambda_z$⟩	
Complex [e]	Diamond cubic	{FCC ⌊0 0 0⌋⌊¼ ¼ ¼⌋}	4
	Kagome	{R ⌊000⌋⌊0 0 ½⌋⌊0 ½ 0⌋⌊½ 0 0⌋} ⟨$\lambda_{111}{=}\sqrt{3}$⟩	6
	Rhombic dodecahedron	{BCC [000] [011] [101] [110]}	5 ⅓

[a] List of structure types is comprehensive
[b] Only considers truss size ratio of two
[c] Neglects trusses with non-orthogonal axes, except for rhombohedral
[d] Structure types are generic; $A^{(i)}$ are elementary trusses
[e] Structure types are illustrative

Table 2.4: Designations of previously-studied trusses.

Reported description	Structure type	Comments
"G6" [9, 34, 37, 38]; "Orthotropic with cubic cells" [2]	$\{SC\}$	
"Octahedral-type" [26, 27, 28] "Pyramidal" [24, 41]	$\{BCC\}$ or $\{BCT\}\langle 1\,1\,\lambda_z\rangle$	Truss type dictated by strut angle Two-layered: $\{BCT\}\langle 1\,1\,\lambda_z\rangle$ One-layered: $1/2\{BCT\}\langle 1 1\lambda_z\rangle$
"Octet truss" [12]	$\{FCC\}$	
"Cross I symmetric" [9, 34, 37, 38]	$\{SC\}\left[{}^1/_2\,{}^1/_2\,{}^1/_2\right]$	Same as G6, except for origin translation
"Hatched" [34, 37, 38]	$\{ST\}\langle 1\,1\,\lambda_z\rangle$	$\lambda_z \approx 1.5$
"Tetrahedral" [48, 59]	$1/3\{R\}\langle\lambda_{111}\rangle$	
"G7" [9, 34, 37, 38]	$\{BCC\}|\{Sq\}$	
"Body centered cubic" [43]	$\{BCC\}|\{SC\}$	
"Orthotropic with cubic cells and global diagonal bracing" (design A) [2]	$\{2SC\}|\{FCC\}\langle 2\,2\,2\rangle$	Specific truss tested: $\{4SC\}^3|\{2FCC\}^3\langle 2\,2\,2\rangle$
"Dode thin" [9, 34, 37, 38]	$\{BCC\,[0\,0\,0]\,[0\,1\,1]\,[1\,0\,1]\,[1\,1\,0]\}$	Also called rhombic dodecahedral
"Tetrahedral with three-fold symmetry" [26, 27, 28]	$\{R\,[0\,0\,0]\,[0\,1\,0]\,[1\,0\,0]\}\langle\lambda_{111}\rangle$	Based on reported angles $\lambda_{111} \approx 2$. Translations are in the hexagonal coordinate system using three-index Miller notation.
"Tetrahedral with six-fold symmetry" [26, 27, 28]	$\{R\,[0\,0\,0]\,[0\,1\,0]\,[1\,0\,0]\}$ $(\theta_{111}=0,\pi/3)\langle\lambda_{111}\rangle$	Based on reported angles $\lambda_{111} \approx 2$. Superposition of the two $\{R\}$ trusses lead to strut intersections.
"Regular truncated octahedron" [22], "Reinforced body centered cubic" [43]	$\{BCC\}|\{SC\}|\{SC\}\left[{}^1/_2\,{}^1/_2\,{}^1/_2\right]$	
Hierarchical "single-layer pyramidal truss and octahedral-type truss" [15]	$\{BCT\}\langle 1 1\,\lambda_z\rangle|\{1/\alpha BCT\}\langle\alpha\,\alpha\,\alpha\lambda_z\rangle$	α is the size ratio
"Single-layer pyramidal" [29]	$\{Sq\}|1/2\{BCT\}\langle 1\,1\,\lambda_z\rangle|\{Sq\}$	Sandwich panel
"Octet panel" [64]	$\{Tr\}|1/3\{R\}\langle\lambda_{111}=\sqrt{3}\rangle|\{Tr\}$	Sandwich panel

Table 2.5: Elastic properties

	$E_1/\rho E_o$	ν_{12}	$G_{12}/\rho E_o$	$\omega \equiv 2G_{12}(1+\nu_{12})/E_1$
$\{nBCC\}^3 \vert \{nSC\}^3$	0.162	0.257	0.069	1.05
$\{nFCC\}^3$	0.111	0.333	0.083	2.00
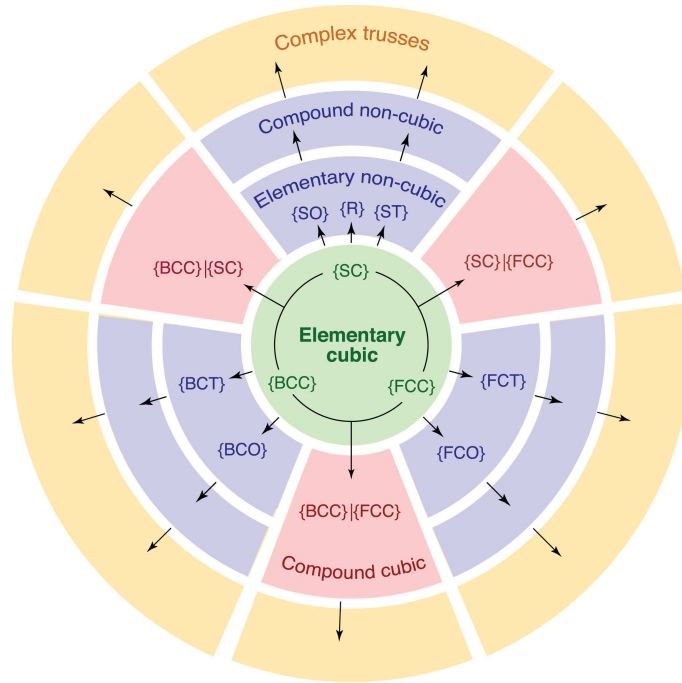
Figure 2.1: Schematic representation of the structure classification system and its conceptual evolution: from elementary cubic trusses (at the center) to more complex structures with non-cubic symmetries and with multiple constituent trusses in compound systems.

(a){2SC}^{3} (b){2BCC}^{3} (c){2FCC}^{3}
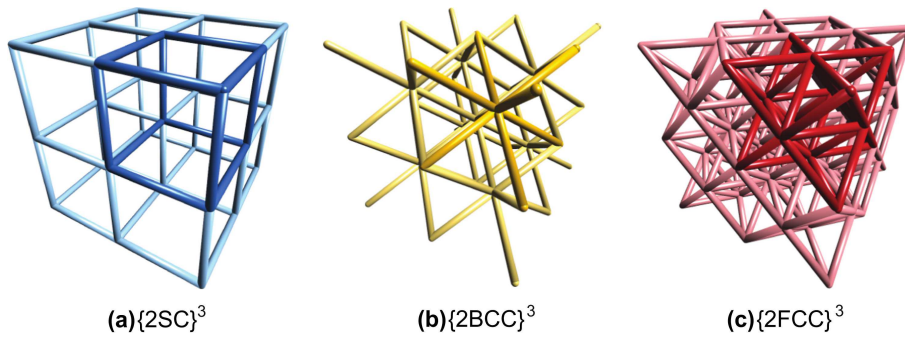
Figure 2.2: Examples of the three elementary cubic trusses. (Unit cells highlighted by darker colors.)

(a) {2BCC}³ | {2SC}³

(b) {2BCC}³ | {2SC}³ | {SC} [½ ½ ½]

(c) {2SC}³ | {2FCC}³

(d) {2BCC}³ | {2FCC}³
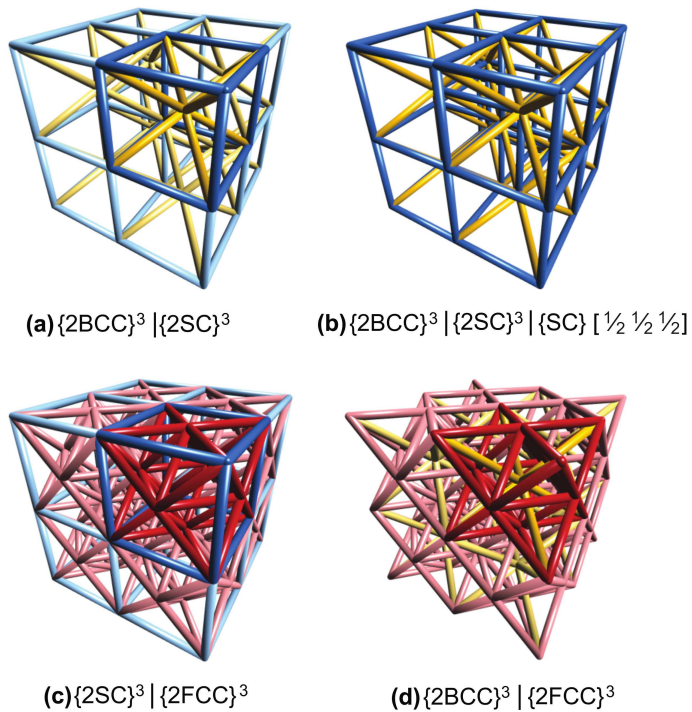
Figure 2.3: Compound cubic trusses. Unit cells are highlighted by darker colors. (Movies of trusses in (a) and (b) available as Supplementary Material at doi.org/10.1016/j.jmps.2016.07.007)

(a)$\{2SC\}^3 | \{FCC\} \langle 2\ 2\ 2 \rangle$ **(b)**$\{2SC\}^3 | \{BCC\} \langle 2\ 2\ 2 \rangle$

(c)$\{2FCC\}^3 | \{SC\} \langle 2\ 2\ 2 \rangle$ **(d)**$\{2FCC\}^3 | \{BCC\} \langle 2\ 2\ 2 \rangle$

(e)$\{2BCC\}^3 | \{FCC\} \langle 2\ 2\ 2 \rangle$ **(f)**$\{2BCC\}^3 | \{SC\} \langle 2\ 2\ 2 \rangle$
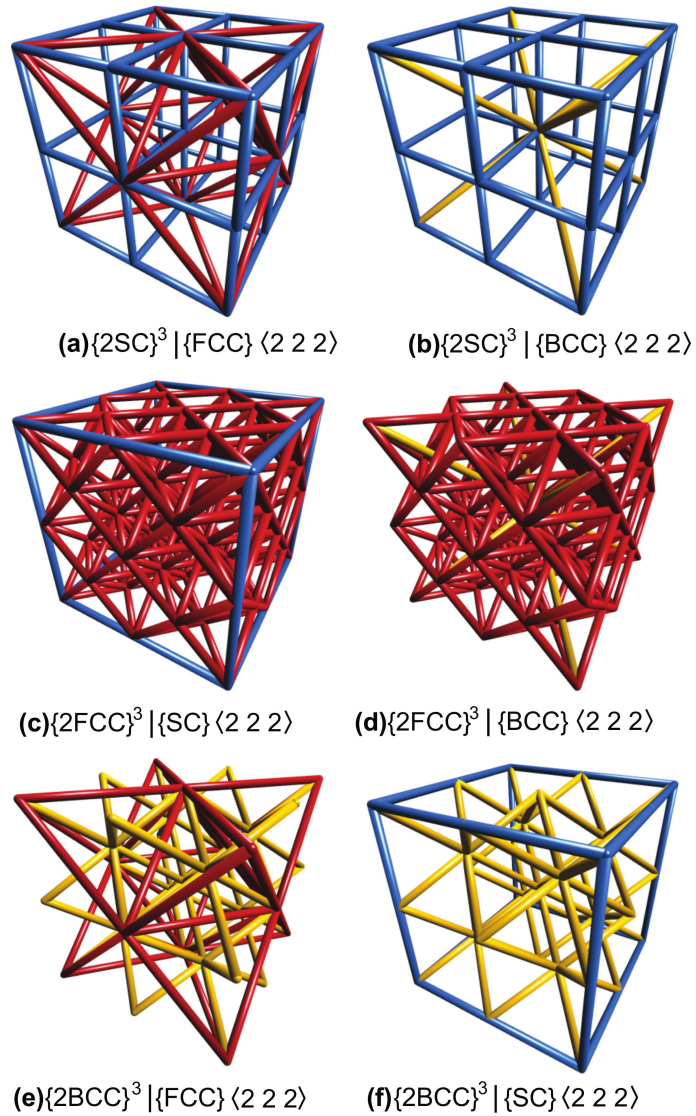
Figure 2.4: Single unit cells of compound cubic supertrusses. (Movies of trusses in (a), (e) and (f) available as Supplementary material at doi.org/10.1016/j.jmps.2016.07.007.)

48

(a) $\{2SO\}^2 \langle 1,1.2,1.5 \rangle$

(b) $\{2BCO\}^2 \langle 1,1.2,1.5 \rangle$

(c) $\{2SO\}^2 \langle 1,1.2,1.5 \rangle \mid \{2BCO\}^2 \langle 1,1.2,1.5 \rangle$

(d) $\{2BCO\}^2 \langle 1,1.2,1.5 \rangle \mid \{SO\} \langle 2,2.4,1.5 \rangle$

(e) $\{2R\}^2 \langle \lambda_{111} = \sqrt{3} \rangle$

(f) $\{R \ (\theta_{111} = 0, \pi/3)\} \langle \lambda_{111} = \sqrt{3} \rangle$
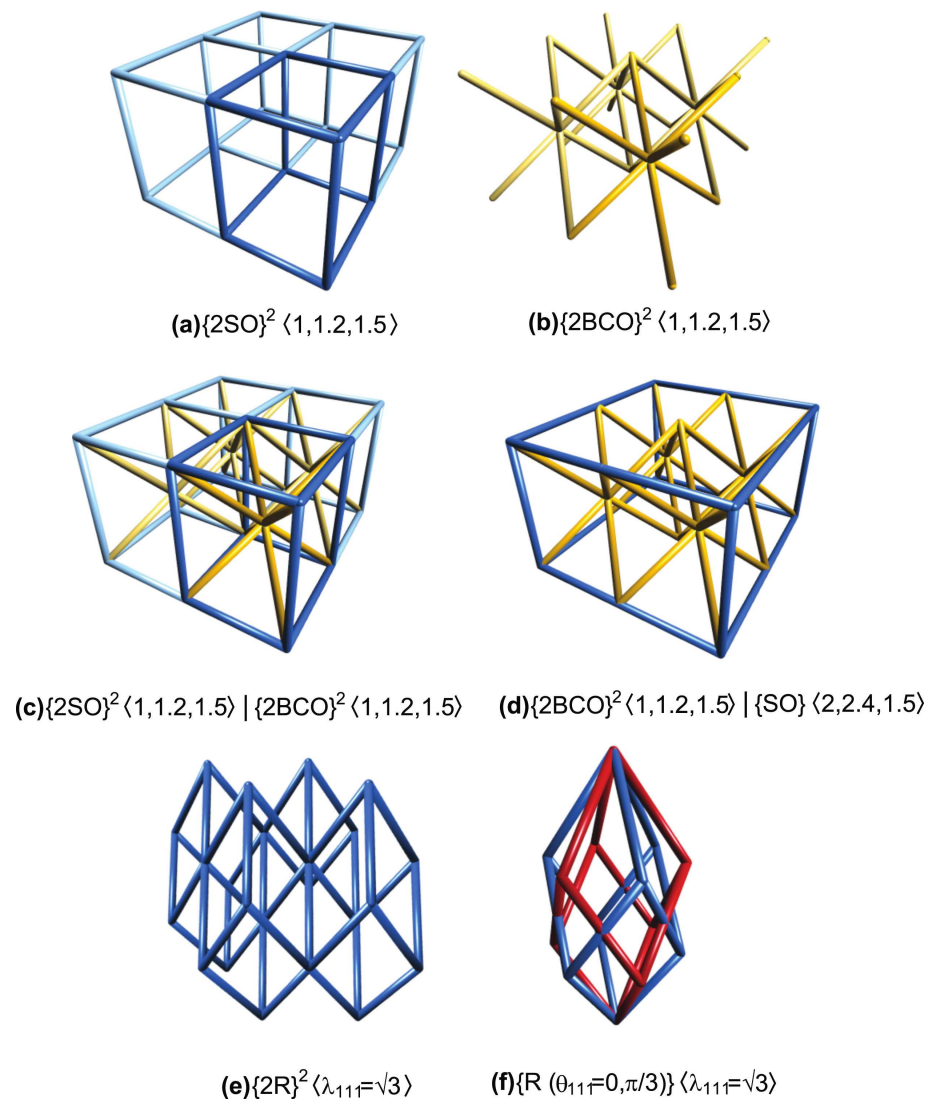
Figure 2.5: Examples of elementary and compound non-cubic trusses. (A movie of the truss in (e) available as Supplementary material at doi.org/10.1016/j.jmps.2016.07.007.)
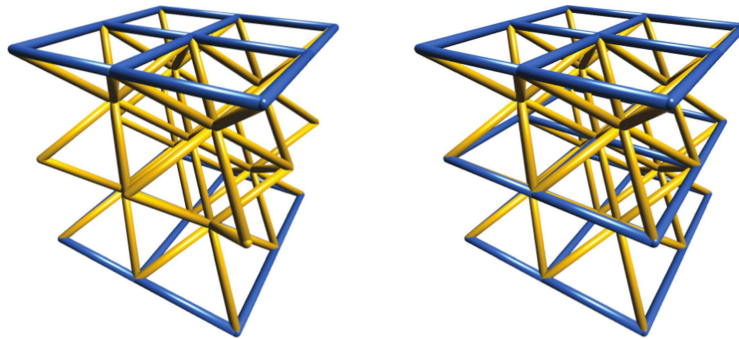
(a) $\{2Sq\}^2|\{2BCC\}^3|\{2Sq\}^2$ **(b)** $\{2Sq\}^2|\{2BCC\}^2|\{2Sq\}^2|\{2BCC\}^2|\{2Sq\}^2$

Figure 2.6: Examples of 2D/3D compound trusses.

(a) $\{2\{\text{FCC}\lfloor 0\ 0\ 0\rfloor \lfloor \frac{1}{4}\ \frac{1}{4}\ \frac{1}{4}\ \rfloor\}\}^3$

(b) $\{2\{\text{R}\lfloor 0\ 0\ 0\rfloor \lfloor 0\ 0\frac{1}{2}\ \rfloor \lfloor 0\frac{1}{2}\ 0\rfloor \lfloor \frac{1}{2}\ 0\ 0\rfloor\}\}^3$

(c) $\{2\{\text{BCC}\ [000]\ [011]\ [101]\ [110]\}\}^3$
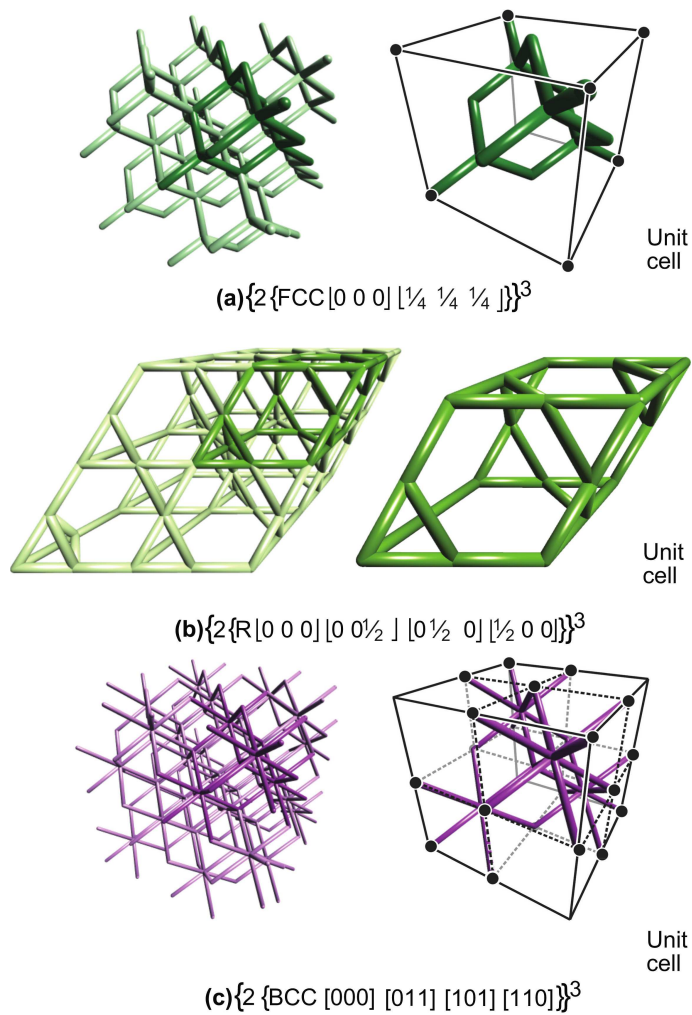
Figure 2.7: Examples of complex trusses: (a) diamond cubic, (b) Kagome and (c) rhombic dodecahedral. Unit cells are highlighted by darker colors. (Movies of all trusses available as Supplementary material at doi.org/10.1016/j.jmps.2016.07.007.)
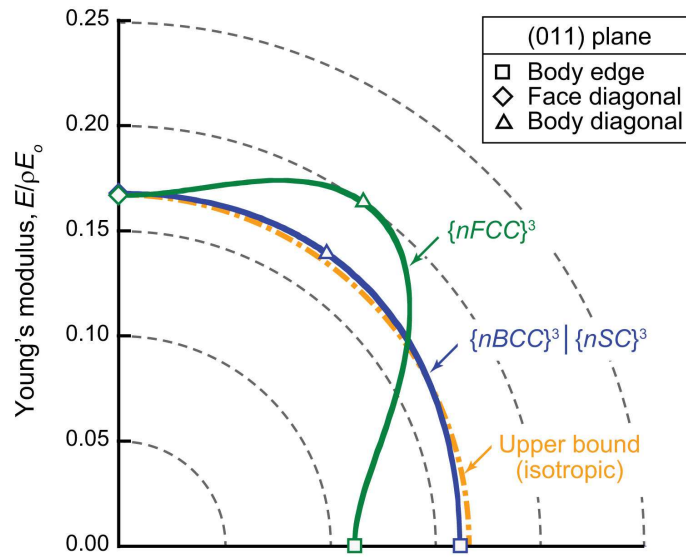
Figure 2.8: Planar sections through polar plots of Young's modulus along the (011) plane for the elementary $\{nFCC\}^3$ and the compound $\{nBCC\}^3|\{nSC\}^3$ trusses. The abscissa is aligned with one of the body edges. Because of symmetry, results for only one quadrant are presented. Results are based on FEA for $n = 25$.

Chapter 3

Design and mechanical properties of elastically isotropic trusses

3.1 Introduction

As discussed previously, periodic truss structures can be designed to have high specific strength and specific stiffness in combination with other desirable attributes. Most truss topologies, however, exhibit strongly anisotropic mechanical properties: an undesirable characteristic when trusses are used in applications in which the directions of loading are not known *a priori*. The present study addresses the design

---

of lightweight (low relative density) truss structures that are elastically isotropic and that also exhibit high strength. The designs are based principally on compound trusses comprising two or more elementary cubic trusses that, on their own, are highly anisotropic.

Truss design can follow one of two broad approaches. In the first, computational algorithms based on finite elements are used for shape and topology optimization [1, 4, 23, 54]. For structural problems, the entire allowable spatial domain is discretized by elements; the properties of the elements form the design variables. An optimization problem is formulated from an objective function and a set of constraints, the latter including mechanical equilibrium of the structure and allowable material volume. Using this approach, elastic moduli have been maximized under constraints of elastic isotropy and fixed relative density [8, 40]. Moduli were calculated from the response of trial structures to various applied test fields. Gradient-based optimization methods were used to find (local) optima. The moduli of resulting topologies have been shown to approach the Hashin-Shtrikman upper bound. However, in general, the topologies are complex and the structures would be difficult to fabricate, even with current additive manufacturing techniques. An additional drawback of this "top-down" approach is that it rarely yields insights into general design principles with broad application.

The second approach (employed here) follows a "bottom-up" path. Notably, elementary truss structures are combined in judicious ways to create trusses in which the positive attributes of the constituent trusses are exploited while their shortcomings are ameliorated. In essence, the topology is fixed at the outset while certain geometric parameters are systematically varied. The resulting design space is much smaller than that in the more general topology optimization approach.

The principal goal of the study is to identify designs of trusses that are: (i) elastically isotropic, (ii) exhibit high specific stiffness, and (iii) have potential for high strength under various loading scenarios, including compression, tension and shear. Preliminary insights into the design strategy are obtained from examination of the topology of elementary cubic trusses. Because of the alignment of struts along the edges of its unit cell, the $\{SC\}$ truss is stiff along the body edges but highly compliant in other loading directions, *e.g.*, along the face diagonal or the body diagonal. In contrast, the $\{BCC\}$ truss is stiff along the body diagonal and compliant in other directions.[1] Since the two trusses exhibit high stiffness along different directions, we expect that combining $\{SC\}$ and $\{BCC\}$ trusses on to a common space lattice

---

[1]From a structural mechanics perspective, $\{SC\}$ and $\{BCC\}$ trusses are mechanisms, not structures. If pin-jointed, they would collapse under infinitesimal loads. If the joints were rendered rigid, collapse would be resisted by the bending stiffness and strength of the struts. These are therefore classified as *bending-dominated* trusses. In contrast, $\{FCC\}$ trusses are structures. If pin-jointed, they could support finite loads in any arbitrary direction; the loads would be transmitted by axial tension or compression in the struts. These are classified as *stretching-dominated* trusses.

should yield a compound truss with a higher degree of isotropy than those of the constituent elementary trusses. The $\{FCC\}$ truss is stiffest along the body diagonal and most compliant along the body edge: the ratio of minimum to maximum stiffness being 5/9 [12]. Although this truss is the most isotropic of the three, we expect that its low stiffness along the body edges might be mediated by the addition of a $\{SC\}$ truss. Since both $\{FCC\}$ and $\{BCC\}$ trusses are stiff along the body diagonal and more compliant along the body edges, a compound truss comprising these two would not be expected to yield improved isotropy.

To provide context for subsequent analyses of buckling failure (the mode that invariably dominates when the relative density is sufficiently low), we find it useful to couch the discussion in terms of three distinct factors governing failure:

(i) The average axial strut strain ϵ_a relative to the global (applied) strain ϵ in each of the constituent strut populations;

(ii) The strut slenderness ratio l/r, where l is strut length and r is its radius (assuming circular cross-sections); and

(iii) The constraints imposed on the strut ends by adjoining struts, characterized by the effective length factor K in Euler buckling theory.

As we show in due course, the macroscopic failure strain of trusses that fail by

buckling is proportional to $\left(\frac{\epsilon}{\epsilon_a}\right)\left(\frac{r}{Kl}\right)^2$.

An additional implicit factor in truss failure is the nodal connectivity, Z. All other factors held constant, high values of Z lead to increased constraints on the strut ends and increased buckling resistance, as manifested in low K. Nodal connectivity is also indirectly related to strut slenderness. That is, if relative density is kept constant, an increase in connectivity must be accompanied by a higher number density of struts which, in turn, must be accommodated by lower strut radius and hence higher slenderness ratio. The preceding two effects act in opposition: the former inhibiting buckling and the latter promoting buckling as Z increases. When Z is sufficiently small (say < 12), truss deformation is dominated by strut bending and the average axial strut strains are negligible [5]. Instead, deformation is accommodated by changes in strut curvature and failure occurs by mechanisms other than buckling (*i.e.* yielding or fracture).

The article is laid out in the following way. Truss topologies, finite element models and solution methods are described in Section 3.2. Elastic properties of the trusses of interest are presented in Section 3.3. The axial strut strains and their spatial variations are considered in Section 3.4. Inelastic (buckling) responses are addressed in Section 3.5. Effects of truss size, characterized by the number of unit cells in a cubic array of such cells, are also explored.

3.2 Methods

3.2.1 Topologies, geometry and models

Finite element (FE) computations were used to ascertain the mechanical properties of, specifically: (i) the elementary cubic trusses $\{nSC\}^3$, $\{nFCC\}^3$ and $\{nBCC\}^3$, (ii) the binary compounds $\{nFCC\}^3|\{nSC\}^3$ and $\{nBCC\}^3|\{nSC\}^3$, and (iii) the ternary compounds $\{nFCC\}^3|\{nBCC\}^3|\{nSC\}^3$ and $\{nBCC\}^3|\{nSC\}^3|\{(n-1)\,SC\}^3\,[^1\!/_2\,{}^1\!/_2\,{}^1\!/_2]$ (the latter being the isotropic truss identified by Gurtner and Durand [22]). Here n was varied from 1 to 11. Structures were discretized using three-dimensional Timoshenko beam elements with circular cross-section. Strut dimensions were selected to yield a relative density of $\rho = 0.01$. (Other FE simulations, with ρ ranging from 0.001 to 0.05, yielded virtually identical results when normalized by relative density accordingly). The properties of the parent material were taken to be: Young's modulus $E_o = 200\,\mathrm{GPa}$, shear modulus $G_o = 80\,\mathrm{GPa}$, and mass density $\rho_o = 7800\,\mathrm{kg\,m}^{-3}$. Strut intersections were modeled as rigid joints. In compound trusses, all struts of a specific constituent truss were assigned the same cross-sectional area, dictated by the total volume fraction of material allocated to that truss type. The proportions of volumes allocated to each constituent truss within the compounds were varied from 0 to 1 in increments

of 0.01. Models were processed using the commercial package Abaqus (Version 6.13-EF4, Dassault Systèmes).

3.2.2   Elastic properties

Elastic properties were computed for uniaxial normal loading (compression or tension) along one of the principal directions (denoted 1) and in pure shear (in the 1-2 plane) using Abaqus/Standard. A state of uniaxial compression was obtained by prescribing displacements of lattice points on opposing faces of the model: $u = \epsilon_1 L$ at $x = L$ and $u = 0$ at $x = 0$, where u is nodal displacement along the 1-axis, x is the position on the 1-axis, ϵ_1 is the strain in the 1-direction and L is the length of the truss along the principal directions. Here lattice points are defined by the space lattice before discretizing struts into beam elements. Rigid body motion of the model was prevented by pinning the lattice point at the origin, *i.e.* $u = v = w = 0$ at $(0,0,0)$ where v and w are nodal displacements along the 2- and 3-axes, respectively, and assigning $w = 0$ for the lattice point at $(0, L, 0)$. Analogously, a state of pure shear was obtained by prescribing nodal displacements on the 1- and 2-faces: $v = \epsilon_{12}L/2$ at $x = L$, $v = -\epsilon_{12}L/2$ at $x = 0$, $u = \epsilon_{21}L/2$ at $y = na$, and $u = -\epsilon_{21}L/2$ at $y = 0$. Rigid body motion was constrained in shear by imposing $w = 0$ at $(0,0,0)$ and $(0, L, L)$. In all cases, the global engineering strains were 0.02, *i.e.*

$\epsilon_1 = 0.02$ for uniaxial compression and $\gamma_{12} = \epsilon_{12} + \epsilon_{21} = 0.02$ for pure shear. From the corresponding computed reaction forces, the Young's modulus, E_1, shear modulus, G_{12}, and Poisson ratio, ν_{12}, were computed.

The degree of elastic anisotropy was ascertained from the variation in axial stiffness with loading direction. The stiffness along a vector $\langle ijk \rangle$ is related to the elastic constants via [39]:

$$\frac{1}{E_{\langle ijk \rangle}} = \frac{1}{E_1} - 2\left(\alpha^2\beta^2 + \beta^2\gamma^2 + \alpha^2\gamma^2\right)\left(\frac{1}{E_1} - \frac{1}{2\,G_{12}} - \frac{\nu_{12}}{E_1}\right) \tag{3.1}$$

where α, β and γ are the direction cosines between $\langle ijk \rangle$ and the principal coordinate axes. The results are presented as polar plots of $E_{\langle ijk \rangle}$.

Based on symmetries in loading and truss topologies, struts are grouped in the following way. In $\{FCC\}$, type I struts comprise [110] and [1$\bar{1}$0], type II comprise [101] and [10$\bar{1}$], and type III comprise [011] and [01$\bar{1}$]. Type I and II struts are oriented at 45 degrees to the compression direction whereas type III struts are perpendicular to the compression direction. Additionally, type I and II struts are loaded in opposite directions under an applied shear strain, γ_{12}. In $\{SC\}$, type IV are [100] (parallel to the compression direction) and type V comprise [010] and [001]. In $\{BCC\}$, type VI struts comprise [111] and [$\bar{1}$11] and type VII comprise [1$\bar{1}$1] and [11$\bar{1}$]. The latter two are loaded in opposite directions under an applied shear strain.

3.2.3   Strut strains

Axial strut strains, ϵ_a, resulting from application of either uniaxial compression, ϵ_1, or pure shear, γ_{12}, in an infinite truss ($n = \infty$) were calculated using the direct stiffness method. For this purpose, a single unit cell was modeled using periodic boundary conditions. The boundary conditions were adapted from a method outlined in [62] whereby nodal displacements on opposing faces of the model are linked via linear multi-point constraints. This method assumes that faces remain planar and does not consider rotational degrees of freedom. The omission of the latter is valid in stretch-dominated trusses provided struts have not buckled (in which case nodal rotations are negligible). In their analysis, Wallash and Gibson reported errors due to the neglect of bending moments in reaction forces of approximately 1.4%. We expect to get similar errors in the present analysis. The cross-sectional area of struts shared between adjacent cells was properly adjusted to avoid over counting. Results are presented for each unique strut population for a given type of loading.

To ascertain the strain amplifications due to external boundaries, axial strut strains resulting from application of uniaxial compression were also calculated for struts in finite trusses. The results were sorted in two ways: (i) by strut type (I–VII) and (ii) by strut location, characterized by the distance δ from the strut centroid to the nearest external free boundary.

3.2.4 Inelastic response

The inelastic responses for uniaxial compression, pure shear and uniaxial tension were computed for finite trusses using Abaqus/Explicit. Boundary conditions were analogous to those employed for the elastic simulations, except that nodal *velocities* (rather than displacements) were prescribed, *e.g.* velocity, $\dot{x} = dx/dt = \dot{\epsilon}L$ at $x = L$ for uniaxial compression. Velocities were selected to yield quasi-static strain rates ($|\dot{\epsilon}| \leq 10^{-3}\,\mathrm{s}^{-1}$). The resulting ratio of kinetic to potential energy was less than 10^{-3} for all time steps in each simulation, confirming quasi-static loading. The equations of motion were integrated using explicit central differences with fixed timestep until reaching a global strain of 2%. To smoothly traverse bifurcation (buckling) phenomena in the solution path, imperfections consistent with the first three buckling modes were superimposed according to the geometric sequence:

$$\Delta\bar{x} = n \sum_{i=1}^{3} B(p)^{i-1}\bar{\phi}_i \tag{3.2}$$

where $\Delta\bar{x}$ is the resultant vector of nodal displacements applied to the original nodal coordinates, n is the lineal number of unit cells, B is the amplitude applied to the first buckling mode, r is the ratio of geometric progression, and $\bar{\phi}_i$ contains the set of nodal displacements of the ith mode shape normalized such that the maximum displacement is equal to 1.0. Here, B was taken to be 0.001, and p was 1/2.

Imperfections of this type do not affect the ultimate truss strength. In the trusses of present interest, failure is governed by elastic buckling of families of struts that are, on average, equally strained. Here the macroscopic truss strength is dictated by the volume-averaged strut stress once all struts have buckled. Because the stress needed for continued strut buckling is constant (*i.e.* the strut response is effectively elastic, perfectly-plastic), a premature buckling event caused by a structural imperfection does not significantly affect the ultimate strength.

Interestingly, without imperfections, the buckled solution can still be found; numerical integration of the equations of motion introduces errors into nodal displacements that serve the same purpose as artificial imperfections. But, since the integration errors and the resulting imperfections are small, buckling causes intense high frequency oscillations. Seeding structural imperfections dramatically reduces these effects. Even with structural imperfections, weak high frequency oscillations are still obtained. As a result, a small amount of damping was introduced in the form of linear bulk viscosity. It generates a pressure,

$$p = \zeta \rho_o c_d l_e \dot{\epsilon}_{vol} \tag{3.3}$$

where ζ is a damping coefficient, ρ_o is the material density, c_d is the dilatational wave speed, l_e is the length of the element and $\dot{\epsilon}_{vol}$ is the volumetric strain rate. For all simulations, $\zeta = 0.06$. Linear bulk viscosity of this form is included by default in

63

Abaqus/Explicit.

3.2.5 Buckling strengths

The preceding results were interpreted in the context of Euler buckling theory. For reference, the critical load P_c for strut buckling is given by $P_c = \pi^2 EI/(Kl)^2$ where E is Young's modulus; I is the second moment of area of the strut cross section; l is its length; and K is the non-dimensional effective-length factor, dictated by the degree of constraint at the strut ends. For example, if transverse displacements and rotations were fully-constrained at both ends, $K = 1/2$; this condition yields the highest buckling load. In contrast, if both strut ends were pin-jointed and displacements of the endpoints were only allowed along the strut axis, $K = 1$. Yet higher values of K would be obtained as the number of degrees of freedom of the strut ends is increased.

In the current study, values of K for each strut population were inferred from the average axial strut strain $\bar{\epsilon}_a$ at the point of buckling of the respective strut population, via $K = \pi r/2l\sqrt{\bar{\epsilon}_a}$. The results were further combined to compute three buckling metrics, defined by $\beta_c = \left(\frac{\epsilon_1}{\epsilon_a}\right)\left(\frac{r}{Kl}\right)^2$ in compression, $\beta_t = -\left(\frac{\epsilon_1}{\epsilon_a}\right)\left(\frac{r}{Kl}\right)^2$ in tension and $\beta_s = -\left(\frac{\gamma_{12}}{\epsilon_a}\right)\left(\frac{r}{Kl}\right)^2$ in shear, for each strut population. The values of the metrics provide quantitative measures of the resistance of the struts to buckling

for each truss type, taking into account strut slenderness (summarized in Table 3.1), axial strut strain (Tables 3.2–3.4), and constraints at the nodes, the latter governed by the number and nature of struts passing through the nodes.

3.3 Elastic properties

3.3.1 Elementary cubic trusses

The three elementary cubic trusses exhibit a wide range of elastic properties and anisotropy. (Polar plots of their axial stiffness for large n are shown in Figure 3.1.) For reference, the maximal stiffness for strut-based isotropic trusses is $E/E_o\rho = 1/6$ [22]. Both the $\{SC\}$ and $\{BCC\}$ trusses are mechanisms; they exhibit high stiffness only along directions parallel to strut directions and are highly compliant in other directions. Specifically, the maximum stiffness of $\{SC\}$ is $E/E_o\rho = 1/3$, along $\langle 100 \rangle$-type directions, whereas the maximum stiffness of $\{BCC\}$ is $E/E_o\rho = 1/9$, along $\langle 111 \rangle$-type directions. On their own, these trusses do not make useful structures. Among the elementary trusses, the $\{FCC\}$ truss is closest to isotropic. Its stiffness is $E/E_o\rho = 1/9$ and $1/5$ along $\langle 100 \rangle$- and $\langle 111 \rangle$-type directions, respectively.

The elastic properties of the elementary cubic trusses are essentially indepen-

dent of n (Figure 3.2). One exception is the shear modulus of the $\{BCC\}$ truss; the average nodal connectivity decreases from 8 when $n = \infty$ to 1.7 when $n = 1$. Consequently, its shear modulus goes to 0 as n goes to 1.

3.3.2 Binary compound trusses

Stiff isotropic trusses are obtained for select combinations of elementary trusses. Variations in the elastic constants with volume fraction of the constituent trusses in the binary compounds are plotted in Fig. 3.3 for $n = 11$. Also shown are the values based on rule-of-mixtures predictions. The latter predictions tacitly assume that the constituent trusses behave independently of each other, *i.e.* without mechanical coupling. Representative polar plots of the axial stiffness are also included as insets. Videos showing the evolution of axial stiffness and elastic moduli are provided in Supplementary Information at doi.org/10.1557/jmr.2018.2 (Vid. S1 and S2). The key observations follow.

The compound trusses $80\%\,\{FCC\}|20\%\,\{SC\}$ and $60\%\,\{BCC\}|40\%\,\{SC\}$ are isotropic.[2] Their Young's moduli are slightly higher than rule-of-mixtures prediction. This is because type V struts, which are perpendicular to the loading axis and stress-free in the elementary structure, are placed into tension in the compound truss,

---

[2] Composition denotes the relative percent of total material volume allocated to each truss.

thereby constraining the lateral node displacements. In shear, the $\{SC\}$ struts (type IV and V) are not loaded and do not contribute to the shear modulus. Thus the shear modulus is well represented by the rule-of-mixtures, in this case given by the product of the volume fraction and modulus of the constituent $\{FCC\}$ or $\{BCC\}$ sub-trusses.

Here again the elastic properties are insensitive to n. Variations of the elastic constants with n for the isotropic $60\% \{BCC\}|40\% \{SC\}$ truss are shown in Figure 3.2. Reported properties of isotropic trusses that are maximally stiff are also shown: $E_1/E_o\rho = 1/6$, $G_{12}/E_o\rho = 1/15$ and $\nu_{12} = 1/4$ [22]. Young's modulus and Poisson's ratio of the compound truss are virtually independent of n and are equivalent to those of the predicted maximal value. A reduction in shear modulus for the compound truss is observed below $n = 3$. Similar to the response of $\{BCC\}$ in shear, the reduction of average nodal connectivity that accompanies the reduction in n leads to a more compliant truss. Variations in the elastic properties of the isotropic $\{FCC\}|\{SC\}$ truss are not shown; by design its properties are identical to those of the $\{BCC\}|\{SC\}$ truss (at least at large n).

3.3.3 Ternary compound trusses

Stiff isotropic trusses are also obtained with certain ternary $\{FCC\}|\{BCC\}|\{SC\}$ compound trusses. Their elastic properties are shown in Figure 3.4. Each property is presented within a Gibbs triangle; each corner represents one of the three elementary trusses, each edge corresponds to one of the three binaries, and the interior regions correspond to the ternaries. Contours show compositions at which the properties are of constant value. Contours highlighting compositions that exhibit elastic properties of isotropic maximally-stiff trusses are also shown. The latter compositions follow straight lines joining the two isotropic binary trusses, namely $80\%\,\{FCC\}|20\%\,\{SC\}$ and $60\%\,\{BCC\}|40\%\,\{SC\}$. All trusses along this line are isotropic and exhibit the highest possible stiffness. Notably absent from the latter are binary combinations of $\{FCC\}$ and $\{BCC\}$. As noted previously, since each of these trusses on its own exhibits high compliance along the body edges, combinations of the two do not ameliorate their inherent anisotropy.

Gurtner and Durand [22] identified another maximally stiff isotropic ternary truss, of the type $\{BCC\}|\{SC\}|\{SC\}\,[^1\!/_2\,{}^1\!/_2\,{}^1\!/_2]$. In their treatment, the cross-sectional areas of struts in the two $\{SC\}$ trusses were taken to be equal to one another. The ratio of cross-sectional areas, s, of the $\{BCC\}$ struts and the $\{SC\}$ struts for maximal isotropic stiffness is $s_{BCC}/s_{SC} = 3\sqrt{3}/4$. This equates to approx-

imately 60% of $\{BCC\}$ and 20% of each of the two $\{SC\}$ trusses. As we show below, the analogous binary truss (with equivalent elastic properties) is more robust in the post-buckling domain.

3.4   Strut strains

3.4.1   Infinite trusses

As a prelude to the non-linear buckling responses of the trusses of interest, we present results for the axial strut strains when the trusses are loaded elastically in compression, in tension and in shear. The trusses of interest are the (anisotropic) $\{FCC\}$ truss, the isotropic binary trusses $\{FCC\}|\{SC\}$ and $\{BCC\}|\{SC\}$, and the isotropic ternary truss $\{BCC\}|\{SC\}|\{SC\}\,[^1\!/_2\,^1\!/_2\,^1\!/_2]$. The axial strut strains ϵ_a, normalized by the respective applied strains, ϵ_1 or γ_{12}, for infinite trusses are summarized in Tables 3.2–3.4.

When the $\{FCC\}$ truss is loaded in compression, the axial strain in type I and II struts (inclined at 45 degrees to the loading direction) is $\epsilon_a/\epsilon_1 = 1/3$ while that in type III struts (perpendicular to the loading direction) is $\epsilon_a/\epsilon_1 = -1/3$. The axial strains in the $\{FCC\}$ struts within the isotropic $\{FCC\}|\{SC\}$ truss differ slightly:

69

$\epsilon_a/\epsilon_1 = 3/8$ for types I and II and $\epsilon_a/\epsilon_1 = -1/4$ for type III. The differences arise because of the constraints imposed by the $\{SC\}$ struts. The strains in type IV and V struts within the binary truss are $\epsilon_a/\epsilon_1 = 1$ and $-1/4$, respectively. (The ratio of the latter two strains emerges naturally from the fact that the Poisson's ratio for the isotropic maximally-stiff truss is $1/4$ [22]). The difference in the axial strains in the compressed struts in the elementary and compound trusses ($1/3$ vs. $3/8$) suggests a slightly higher propensity for strut buckling in the compound truss at a prescribed macroscopic strain. The results for strut strains for tensile loading are the same except for a sign change.

For shear loading, the axial strut strains in the $\{FCC\}$ truss are $\epsilon_a/\gamma_{12} = 1/2$, $-1/2$ and 0 in type I, II and III struts, respectively. The same results are obtained for the $\{FCC\}$ struts within the binary $\{FCC\}|\{SC\}$ truss. Here the $\{SC\}$ struts experience no axial strain and therefore have no effect on the elastic response of the $\{FCC\}$ sub-truss (apart from the reduction in the diameter of the $\{FCC\}$ struts, to maintain constant relative density).

When compound isotropic trusses (both binary and ternary) containing $\{BCC\}$ struts are loaded in compression, all such struts experience the same axial strain: $\epsilon_a/\epsilon_1 = 1/6$. (On its own, the elementary $\{BCC\}$ truss is entirely bend-dominated and thus the struts experience negligible axial strain.) Again the strains in type IV

and V struts within the $\{SC\}$ truss are $\epsilon_a/\epsilon_1 = 1$ and $-1/4$. For shear loading, the strains in the $\{BCC\}$ sub-truss are $\epsilon_a/\gamma_{12} = 1/3$ and $-1/3$ while the constituent $\{SC\}$ struts experience no axial strain.

3.4.2 Boundary effects in finite trusses

Strut strains differ in near-boundary regions because of local differences in connectivity and constraint. Effects of boundaries on strut strains for compressive loading of trusses with $n = 11$ are shown in Figure 3.5. Strains are plotted against the normalized distance δ/a from the centroid of a strut to the nearest external free boundary. Data points are labeled by truss type and solid lines indicate predicted strains in infinite trusses. In all cases, some of the near-boundary struts experience a strain that is significantly greater or less than the average value.

The maximum strain amplification in type I and II struts in the $\{FCC\}$ truss is about 35%; the amplification persists over distances of about $\delta/a = 2$ into the truss interior. Type III struts in this truss experience a maximum (tensile) strain of $\epsilon_a/\epsilon_1 = -1/2$: 50% greater than the average value for that strut population. The most heavily strained struts are ones that intersect the truss edges (see Video S3 in Supplementary Information at doi.org/10.1557/jmr.2018.2). In the two binary trusses, the strain amplification within $\{SC\}$ struts is negligible. In contrast, $\{BCC\}$

71

and $\{FCC\}$ struts in the two binary trusses experience strain amplifications as high as 80% and 35%, respectively. Even higher amplifications are obtained in the near-surface $\{BCC\}$ struts in the ternary truss. In these cases the effects also persist to depths of $\delta/a \approx 2$.

The magnitude of strain amplification does not change appreciably with truss size. Distributions in axial strut strains for $n = 2 - 11$ are shown in Figure 3.6. Within a given strut type, the minimum and maximum strains are virtually independent of n. The middle two quartiles of data shrink as n increases because an increasing fraction of struts is located away from external boundaries. Strain amplifications for struts of the same type can be highly dependent on truss type. Type III struts of the elementary $\{FCC\}$ truss (Fig. 3.6(a)) on average experience greater strain amplification than that for struts in the compound truss (Fig. 3.6(b)). The most significant changes between corresponding struts of different trusses are seen when comparing the strut strains of the ternary truss to that of the binaries. Type IV struts, which experience little variation in axial strain in either binary truss, experience large strain amplifications in the ternary truss. Additionally, the maximum axial strain in $\{BCC\}$ struts (type VI and VII) in the ternary truss is roughly twice that of the $\{BCC\}|\{SC\}$ truss, despite the fact that the $\{BCC\}$ struts are identical in both structures.

3.5 Nonlinear response and strength

3.5.1 Compression ($n=11$)

The stress-strain responses of the four trusses of interest in compression are shown in Figure 3.7(a), all for truss size $n = 11$. Videos showing truss deformation are provided in Supplementary Information at doi.org/10.1557/jmr.2018.2. Stress is normalized by $E_o\rho^2$ and strain is normalized by ρ. These normalizations yield the expected scalings in properties, notably stiffness proportional to $E_o\rho$ and buckling strength proportional to $E_o\rho^2$. Provided ρ is sufficiently small and failure is buckling-dominated (that is, neither yielding nor fracture intervene), the results in this form are, to a very good approximation, independent of ρ and E_o. This feature is illustrated in Figure 3.8.

The $\{FCC\}$ truss exhibits the lowest modulus but highest initial buckling stress (Fig. 3.7(a)). Buckling occurs within 2/3 of the struts (types I and II); the remainder (type III) experience tension. Buckling initiates and proceeds at a stress $\sigma_1/E_o\rho^2 \approx$ 0.057. This yields essentially elastic, perfectly-plastic behavior.

Although the addition of the $\{SC\}$ truss to the $\{FCC\}$ truss is required to produce an elastically isotropic (binary) truss, the addition has a detrimental effect on strength. In the $\{FCC\}|\{SC\}$ truss, type IV struts within the $\{SC\}$ sub-truss buckle

first, at a stress $\sigma_1/E_o\rho^2 \approx 0.03$. As buckling of these struts proceeds, the tangent modulus decreases only slightly, because the $\{FCC\}$ struts remain unbuckled. The latter struts subsequently buckle, at a stress $\sigma_1/E_o\rho^2 \approx 0.048$: about 20% lower than that of the elementary $\{FCC\}$ truss. At this point essentially all of the load is borne by the $\{FCC\}$ struts.

The binary $\{BCC\}|\{SC\}$ exhibits a similar sequence of buckling events, albeit at higher stresses; the $\{SC\}$ and $\{BCC\}$ struts buckle at stresses $\sigma_1/E_o\rho^2 \approx 0.041$ and 0.062, respectively. The latter exceeds the strength of the elementary $\{FCC\}$ truss by about 10%. This effect could be exploited in practice only if the strut material were to have sufficiently high yield and fracture strains, thereby allowing the struts to remain elastic up to the second buckling event. The ternary $\{BCC\}|\{SC\}|\{SC\}$ truss exhibits the lowest buckle-initiation stress.

3.5.2 Tension (n=11)

All trusses undergo compressive strut buckling when the applied load is tensile (Figure 3.7(b)). The $\{FCC\}$ truss exhibits the lowest modulus and the lowest buckling stress. Buckling initiates and proceeds at $\sigma_1/E_o\rho^2 \approx 0.079$: 40% greater in magnitude than the corresponding compressive strength. The strength differential is attributable to the fraction of buckling struts: 1/3 in tension (type III) and 2/3 in

compression (strut types I and II). The balance of struts — 2/3 in tension and 1/3 in compression — provides stabilization against buckling.

Strut buckling in the compound trusses leads to only a modest reduction in tangent modulus and a bilinear stress-strain response. The secondary tangent modulus is governed by the struts that are aligned with the loading direction and that bear most of the load. Buckling begins in the $\{FCC\}|\{SC\}$ truss at essentially the same strain as that of the elementary $\{FCC\}$. But, because the stiffness of the compound truss is higher (by about 15%), the buckling stress is higher by a proportionate amount (also 15%).

The $\{BCC\}|\{SC\}$ truss exhibits the highest strength, governed by buckling of type V $\{SC\}$ struts. By comparison to the $\{SC\}$ struts in the $\{FCC\}|\{SC\}$ and the $\{BCC\}|\{SC\}|\{SC\}$ $[^1/_2 \, ^1/_2 \, ^1/_2]$ trusses, type V $\{SC\}$ struts have the lowest slenderness ratio.

3.5.3 Shear (n=11)

The responses in shear are plotted in Figure 3.7(c). Here the same normalizations are used for stress and strain: $E_o\rho^2$ and ρ, respectively. (Note that when stretch-dominated trusses are loaded in shear, the struts experience only axial loads, and

hence their stresses are dictated by E_o, not G_o.)

The $\{FCC\}$ truss exhibits the highest initial stiffness and the highest buckling stress (Figure 3.7(c)). Buckling initiates in type III struts at $\tau_{12}/E_o\rho^2 \approx 0.046$. Thereafter, the tangent modulus decreases by about 80% and the stress continues to increase as the type I struts are stretched further. In the $\{FCC\}|\{SC\}$ truss, the modulus and the buckling strain are each reduced by 20% relative to those of the elementary FCC truss. As a result, the $\{FCC\}$ struts in the compound truss buckle at an applied stress that is about 64% that of the $\{FCC\}$ truss. Here again the addition of $\{SC\}$ to $\{FCC\}$ to produce an isotropic binary truss comes at the expense of a significantly reduced strength.

The $\{BCC\}|\{SC\}$ and the $\{BCC\}|\{SC\}|\{SC\}$ $[{}^1/_2 \, {}^1/_2 \, {}^1/_2]$ trusses buckle at the same stress: $\tau_{12}/E_o\rho^2 \approx 0.043$. This is because the $\{BCC\}$ sub-trusses in the two compound trusses are equivalent. Here the $\{SC\}$ struts make no significant contribution to the response prior to buckling. Only after the $\{BCC\}$ struts buckle do the $\{SC\}$ struts engage and the curves for the two trusses begin to diverge.

3.5.4   Effects of truss size on strength

In light of the nonlinear behavior obtained in the post-buckling domain, truss strengths are characterized using offset stresses at two strains: 0.02% and 1%. Effects of truss size are shown in Figure 3.9. Here the strengths are plotted against $1/n$. (Although this selection was based in part on the observation that the fraction of struts at the free boundaries is proportional to $1/n$, the effects of n on strength are not due entirely to boundary effects, as discussed below.) In this form the strengths vary essentially linearly with $1/n$. Linear extrapolation to $1/n = 0$ yields the expected strengths of infinitely large trusses.

The offset stresses for the $\{FCC\}$ truss in tension and compression are the same at both the 0.02% and 1% levels, a result of the elastic, perfectly-plastic behavior in these two loadings. In shear the two differ slightly, because of the hardening caused by stretching of type I struts after type II struts have buckled.

The behaviors of the compound trusses in compression are more nuanced. Here there are two distinct buckling events in the constituent sub-trusses; the 0.02% offset captures the first whereas the 1% offset captures the second. With the hardening that occurs between the two buckling events, the 1% offset strengths for the compound trusses become comparable to those for the $\{FCC\}$ truss. Indeed, for large trusses,

the $\{BCC\}|\{SC\}$ is slightly stronger than the $\{FCC\}$ (by about 10%).

Although the linear dependence of strength on $1/n$ appears to coincide with the scaling of the fraction of struts that are affected by boundaries, the size-dependence is due at least in part (perhaps largely) to the variations in strut slenderness ratio with n. That is, in order to have circular struts along the truss faces and edges while maintaining a constant relative density, the strut slenderness must be adjusted to reflect changes in n. For example, l/r in the $\{FCC\}$ truss goes from about 63 to 52 as n goes from 1 to infinity. Analogous adjustments must be made to maintain the same volume fractions in the compound trusses. For example, the slenderness ratio of the $\{SC\}$ struts in the $\{BCC\}|\{SC\}$ truss goes from 97 to 49 as n goes from 1 to infinity. The slenderness ratio of the $\{BCC\}$ struts in this truss remain constant throughout, since these struts are contained entirely within the truss interior. The increase in slenderness ratio with decreasing n must play a central role in the reported dependence of strength on truss size.

3.5.5 Effective-length factors and buckling metrics

Effective-length factors K (inferred from truss strength, strut strain and strut slenderness ratio) are, to a very good approximation, independent of n when $n > 5$ (Figure 3.10). Values of K in this domain for each strut population are summarized

in Tables 3.2–3.4.

In uniaxial compression, K is lowest for type IV $\{SC\}$ struts within the compound trusses and falls in the narrow range of 0.53-0.60. Being close to 1/2, these values indicate that the end conditions on the struts resemble those of a strut that is fully constrained at both ends. Values of K for other struts are somewhat higher, falling in the range 0.7-0.8. Specific values depend on the fraction of struts that are undergoing buckling and the fraction of struts that experience tension.

In the elementary $\{FCC\}$ truss, $K = 0.72$, 0.61 and 0.58 in compression, tension and shear, respectively. The differences are attributable to the lower fraction of struts that buckle in shear and tension relative to that in compression: only 1/3 in shear (strut type I) and in tension (type III), and 2/3 in compression (strut types I and II). The balance of struts — 2/3 in shear and tension and 1/3 in compression — provides stabilization against buckling. Comparable differences are obtained in the $\{FCC\}$ sub-truss within the compound trusses. Here again the differences are attributable to the fractions of buckling struts.

Similar trends are obtained in the $\{BCC\}$ sub-truss within the two compound trusses. For example, in the $\{BCC\}|\{SC\}$ binary, K is higher in compression (0.76) than in shear (0.65), again reflecting the fraction of buckling struts: 100% in compression and 50% in shear.

Finally, examination of the buckling metrics (Tables 3.2–3.4) provides additional insights into the sequence of buckling events and their manifestations in the stress-strain responses. In compression, for example, the ranking of stresses and strains at the 0.02% offset follow in accordance with the buckling metric β_c: the lowest values associated with buckling of the $\{SC\}$ struts in the $\{FCC\}|\{SC\}$, $\{BCC\}|\{SC\}|\{SC\}$ and $\{BCC\}|\{SC\}$ trusses ($\beta_c = 0.07\rho$, 0.08ρ, and 0.12ρ, respectively), followed by buckling in the elementary $\{FCC\}$ truss ($\beta_c = 0.22\rho$). Whereas all struts in the $\{FCC\}$ buckle simultaneously and hence lead to a constant buckling stress, the compound trusses continue to "harden", until the second population of compressed struts buckles ($\beta_c = 0.38\rho$ and 0.35ρ in $\{BCC\}|\{SC\}$ and $\{BCC\}|\{SC\}|\{SC\}$, respectively). Similar correlations are evident upon examination of the buckling sequences under tensile and shear loading (Figures 3.7(c) and 3.7(b)) along with the metrics β_t and β_s (Tables 3.3 and 3.4).

3.6 Summary and conclusions

Families of stiff isotropic compound trusses based on binary and ternary combinations of elementary cubic trusses have been identified. Each exhibits the maximal axial stiffness for isotropic trusses [22]. The stiffnesses of some of these trusses are not

simply the additive sums of the contributions from the constituent sub-trusses. Instead, mechanical coupling between the constituent elementary trusses enables more efficient strut loading and leads to increased stiffness. This behavior is best exemplified by the 60% $\{BCC\}|$ 40% $\{SC\}$ truss, wherein the Young's modulus is over 20% greater than the rule-of-mixtures prediction.

The effects of truss topology and geometry on buckling strength can lead to three distinct effects: (i) the axial strains within buckling struts, (ii) the slenderness ratio of buckling struts, and (iii) the buckling constraints at the strut ends, manifested in the effective length factors. The three factors are combined into buckling metrics for the three loading scenarios. This partitioning of effects yields new insights into the connections between truss topology and truss strength. Based solely on geometric complexity, binary compound trusses are preferable over ternaries. Binary trusses are also superior to ternaries in terms of their inelastic response. The latter differences stem from the fact that, in order to maintain a fixed relative density, the slenderness ratio of some of the struts must be increased when expanding the design from binary to ternary trusses. The increase in nodal connectivity associated with the third truss does not provide sufficient benefit to offset the detrimental effects of higher strut slenderness ratios.

Boundary effects persist roughly two unit cell lengths into the truss from the

surface. There, reduced nodal constraint leads to a dispersion in strut strain. It is in these regions that strut buckling initiates. Although boundary effects do not play a dominant role in the buckling strengths of the present trusses, they would naturally affect other failure modes. That is, if failure were to occur by strut yielding or fracture, strain amplifications in the near-boundary regions could reduce truss strengths substantially relative to those expected on the basis of average strut strains in the bulk of the truss.

The $\{BCC\}|\{SC\}$ truss is competitive with the $\{FCC\}$ truss in several respects. In addition to being isotropic with maximal stiffness, it exhibits compressive and shear strengths that are comparable to those of the $\{FCC\}$ for large offset strains, as well as higher strength in tension. Achieving the higher strengths is predicated, however, on the material having sufficiently high yield and tensile fracture strain; otherwise, strut yield or fracture would govern strength.

Table 3.1: Values of slenderness ratio for each strut type in the elementary (anisotropic) $\{FCC\}$ truss and in three isotropic compound trusses.

	Slenderness ratio*, l/r		
	$\{SC\}$	$\{BCC\}$	$\{FCC\}$
$\{FCC\}$	—	—	$\frac{2^{3/4}\sqrt{3\pi}}{\sqrt{\rho}} \approx \frac{5.16}{\sqrt{\rho}}$
$80\%\,\{FCC\}\|20\%\,\{SC\}$	$\frac{\sqrt{15\pi}}{\sqrt{\rho}} \approx \frac{6.87}{\sqrt{\rho}}$	—	$\frac{\sqrt{15\pi}}{2^{1/4}\sqrt{\rho}} \approx \frac{5.77}{\sqrt{\rho}}$
$60\%\,\{BCC\}\|40\%\,\{SC\}$	$\frac{\sqrt{15\pi}}{\sqrt{2\rho}} \approx \frac{4.85}{\sqrt{\rho}}$	$\frac{3^{1/4}\sqrt{5\pi}}{\sqrt{\rho}} \approx \frac{5.22}{\sqrt{\rho}}$	—
$60\%\,\{BCC\}\|20\%\,\{SC\}$ $\|20\%\,\{SC\}\,[^1/_2\,^1/_2\,^1/_2]$	$\frac{\sqrt{15\pi}}{\sqrt{\rho}} \approx \frac{6.87}{\sqrt{\rho}}$	$\frac{3^{1/4}\sqrt{5\pi}}{\sqrt{\rho}} \approx \frac{5.22}{\sqrt{\rho}}$	—

* Neglects overlapping volume at nodes.

Table 3.2: Strut strains, buckling metrics, and truss strengths for compressive loading.

	{SC}				{BCC}				{FCC}			
	Strut type	$\frac{\epsilon_a}{\epsilon_1}$	K	$\left(\frac{\epsilon_1}{\epsilon_a}\right)\left(\frac{r}{Kl}\right)^2$	Strut type	$\frac{\epsilon_a}{\epsilon_1}$	K	$\left(\frac{\epsilon_1}{\epsilon_a}\right)\left(\frac{r}{Kl}\right)^2$	Strut type	$\frac{\epsilon_a}{\epsilon_1}$	K	$\left(\frac{\epsilon_1}{\epsilon_a}\right)\left(\frac{r}{Kl}\right)^2$
{FCC}	—	—	—	—	—	—	—	—	I, II	$\frac{1}{3}$	0.72	0.22ρ
									III	$-\frac{1}{3}$	—	—
80% {FCC}|20% {SC}	IV	1	0.56	0.07ρ	—	—	—	—	I, II	$\frac{3}{8}$	0.70	0.16ρ
	V	$-\frac{1}{4}$	—	—					III	$-\frac{1}{4}$	—	—
60% {BCC}|40% {SC}	IV	1	0.60	0.12ρ	VI, VII	$\frac{1}{6}$	0.76	0.38ρ	—	—	—	—
	V	$-\frac{1}{4}$	—	—								
60% {BCC}|20% {SC} |20% {SC} $\left[\frac{1}{2}\,\frac{1}{2}\,\frac{1}{2}\right]$	IV	1	0.53	0.08ρ	VI, VII	$\frac{1}{6}$	0.80	0.35ρ	—	—	—	—
	V	$-\frac{1}{4}$	—	—								

Table 3.3: Strut strains, buckling metrics, and truss strengths for tensile loading.

|	{SC}			{BCC}			{FCC}		
	Strut type	$\frac{\epsilon_a}{\epsilon_1}$ K	$-\left(\frac{\epsilon_1}{\epsilon_a}\right)\left(\frac{r}{Kl}\right)^2$	Strut type	$\frac{\epsilon_a}{\epsilon_1}$ K	$-\left(\frac{\epsilon_1}{\epsilon_a}\right)\left(\frac{r}{Kl}\right)^2$	Strut type	$\frac{\epsilon_a}{\epsilon_1}$ K	$-\left(\frac{\epsilon_1}{\epsilon_a}\right)\left(\frac{r}{Kl}\right)^2$
{FCC}	—	—	—	—	— —	—	I, II	$\frac{1}{3}$ —	—
							III	$-\frac{1}{3}$ 0.61	0.30ρ
80% {FCC}|20% {SC}	IV	1 —	—	—	— —	—	I, II	$\frac{3}{8}$ —	—
	V	$-\frac{1}{4}$ 0.62	0.22ρ				III	$-\frac{1}{4}$ 0.59	0.34ρ
60% {BCC}|40% {SC}	IV	1 —	—	VI, VII	$\frac{1}{6}$ —	—	—	— —	—
	V	$-\frac{1}{4}$ 0.68	0.37ρ						
60% {BCC}|20% {SC} |20% {SC} [½ ½ ½]	IV	1 —	—	VI, VII	$\frac{1}{6}$ —	—	—	— —	—
	V	$-\frac{1}{4}$ 0.75	0.15ρ						

Table 3.4: Strut strains, buckling metrics, and truss strengths for shear loading.

	{SC}				{BCC}				{FCC}			
	Strut type	$\frac{\epsilon_a}{\gamma_{12}}$	K	$-\left(\frac{\gamma_{12}}{\epsilon_a}\right)\left(\frac{r}{Kl}\right)^2$	Strut type	$\frac{\epsilon_a}{\gamma_{12}}$	K	$-\left(\frac{\gamma_{12}}{\epsilon_a}\right)\left(\frac{r}{Kl}\right)^2$	Strut type	$\frac{\epsilon_a}{\gamma_{12}}$	K	$-\left(\frac{\gamma_{12}}{\epsilon_a}\right)\left(\frac{r}{Kl}\right)^2$
{FCC}	—	—	—	—	—	—	—	—	I	$\frac{1}{2}$	—	—
									II	$-\frac{1}{2}$	0.58	0.23ρ
									III	0	—	—
80% {FCC}|20% {SC}	IV, V	0	—	—	—	—	—	—	I	$\frac{1}{2}$	—	—
									II	$-\frac{1}{2}$	0.56	0.19ρ
									III	0	—	—
60% {BCC}|40% {SC}	IV, V	0	—	—	VI	$\frac{1}{3}$	—	—	—	—	—	—
					VII	$-\frac{1}{3}$	0.65	-0.26ρ				
60% {BCC}|20% {SC} |20% {SC} $\left[^1/_2\,^1/_2\,^1/_2\right]$	IV, V	0	—	—	VI	$\frac{1}{3}$	—	—	—	—	—	—
					VII	$-\frac{1}{3}$	0.65	-0.26ρ				

Figure 3.1: Polar surfaces of axial stiffness for elementary cubic trusses.
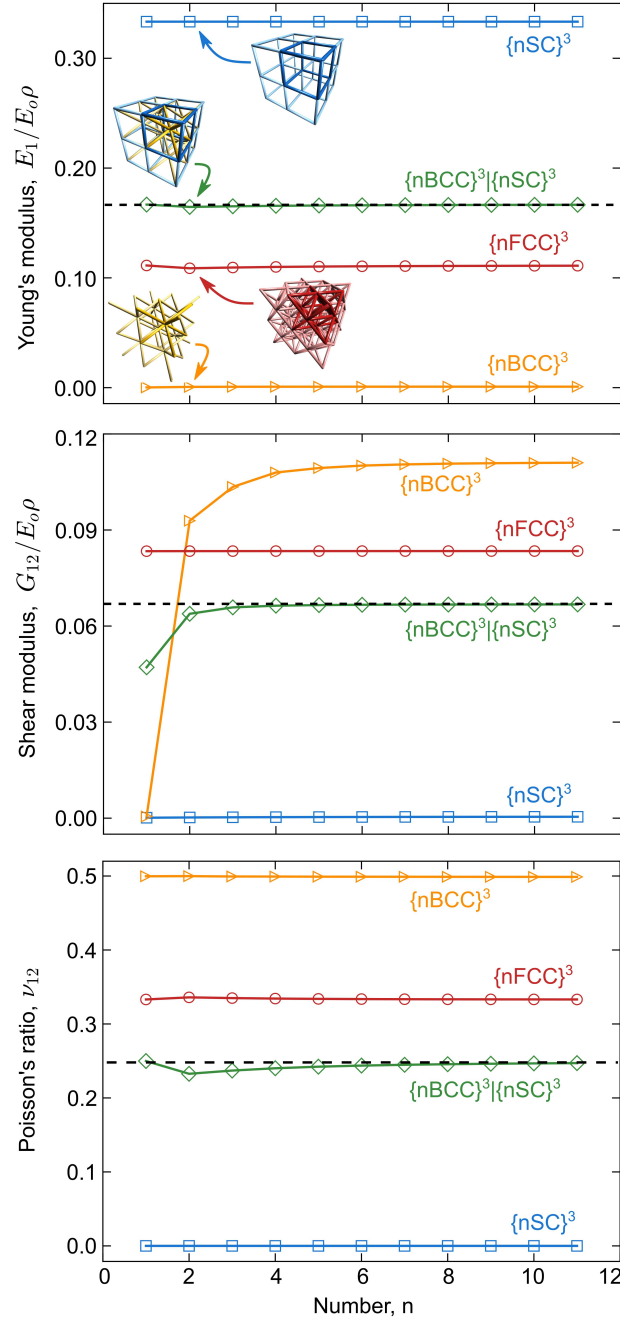
Figure 3.2: Elastic properties of cubic truss structures with finite size normalized by Youngs modulus of the parent material and relative density of the truss. The Young's modulus of the $\{nBCC\}^3$ truss and the shear modulus of the $\{nSC\}^3$ truss are 0.0006 and 0.0002, respectively: both close to but not identically zero, a consequence of rigid connections at the nodes.
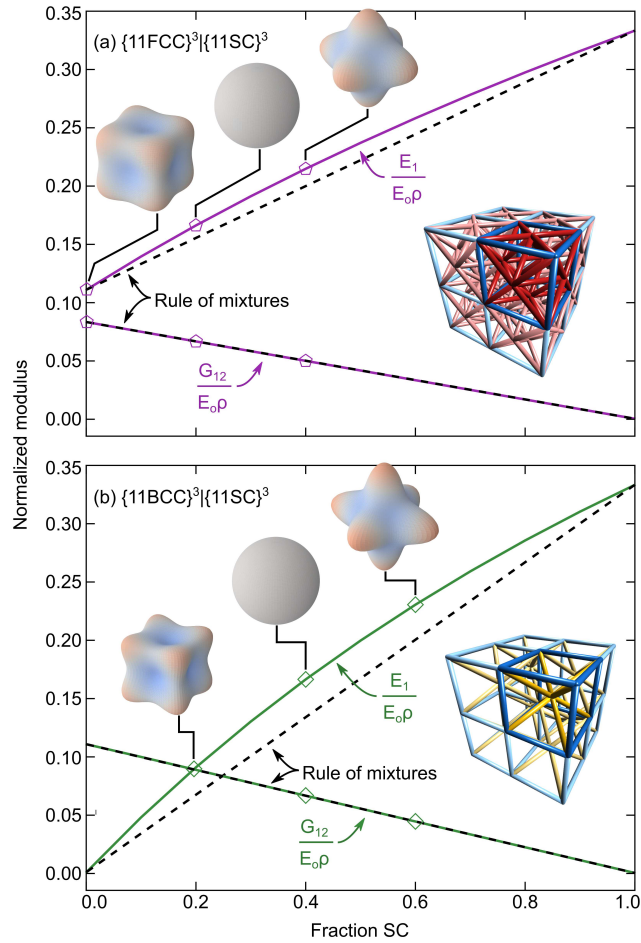
Figure 3.3: Young's and shear moduli for binary trusses comprising $\{SC\}$ and either (a) $\{FCC\}$ or (b) $\{BCC\}$ trusses. Insets are polar plots of axial stiffness. (See also Videos S1 and S2 in Supplementary Information at doi.org/10.1557/jmr.2018.2.)
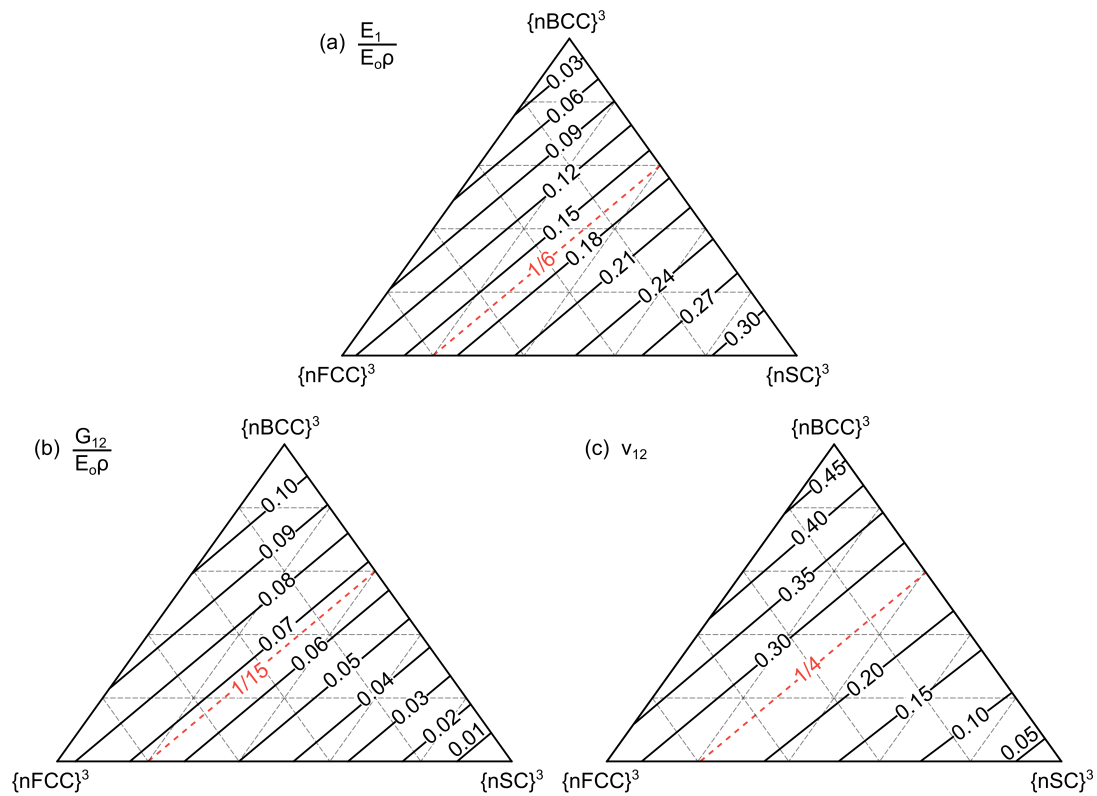
Figure 3.4: (a) Young's modulus, (b) shear modulus and (c) Poisson's ratio for ternary combinations of $\{SC\}$, $\{FCC\}$ and $\{BCC\}$ trusses.
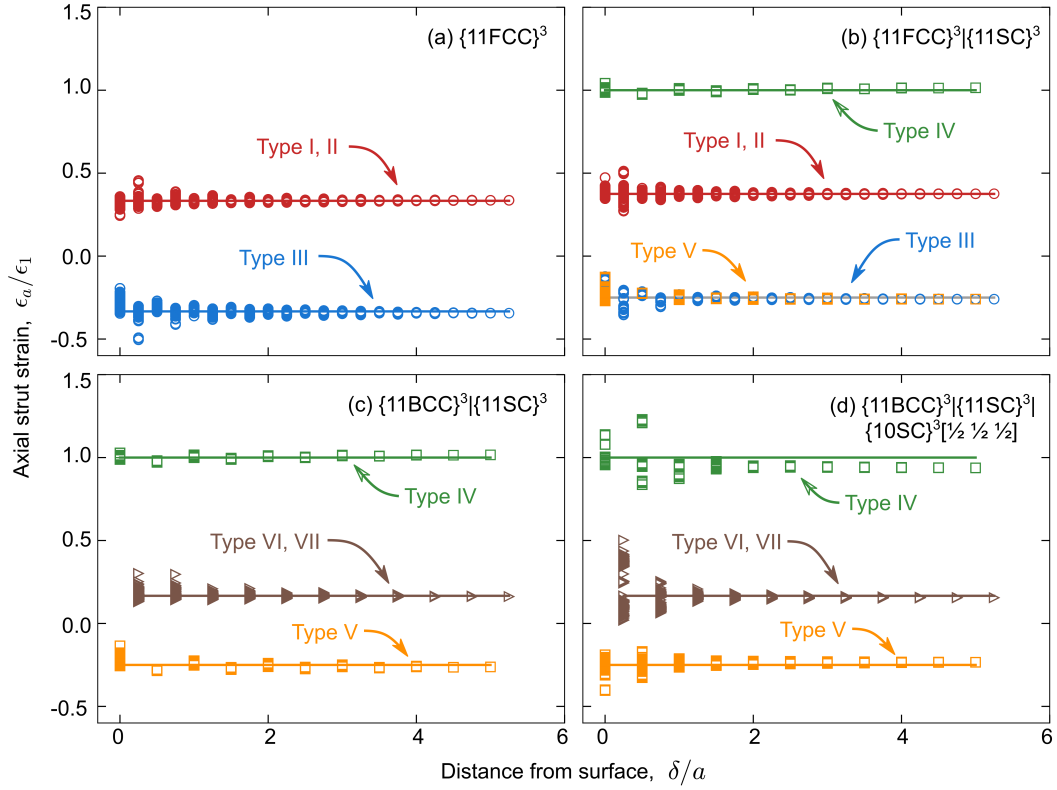
Figure 3.5: Variations in axial strut strains with distance from the nearest external free boundary.
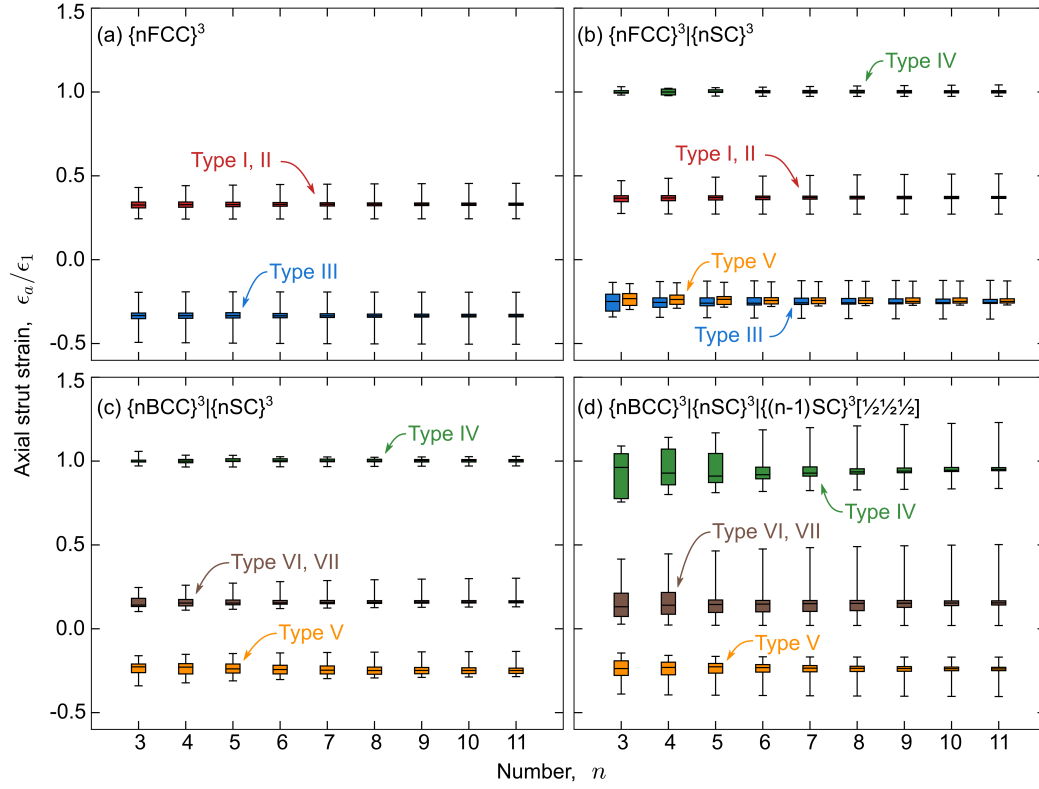
Figure 3.6: Summary or axial strut strains at a compressive strain of 0.01. Central lines represent means, boxes contain the middle two quartiles of data, and outlying hash marks represent minimum and maximum values.
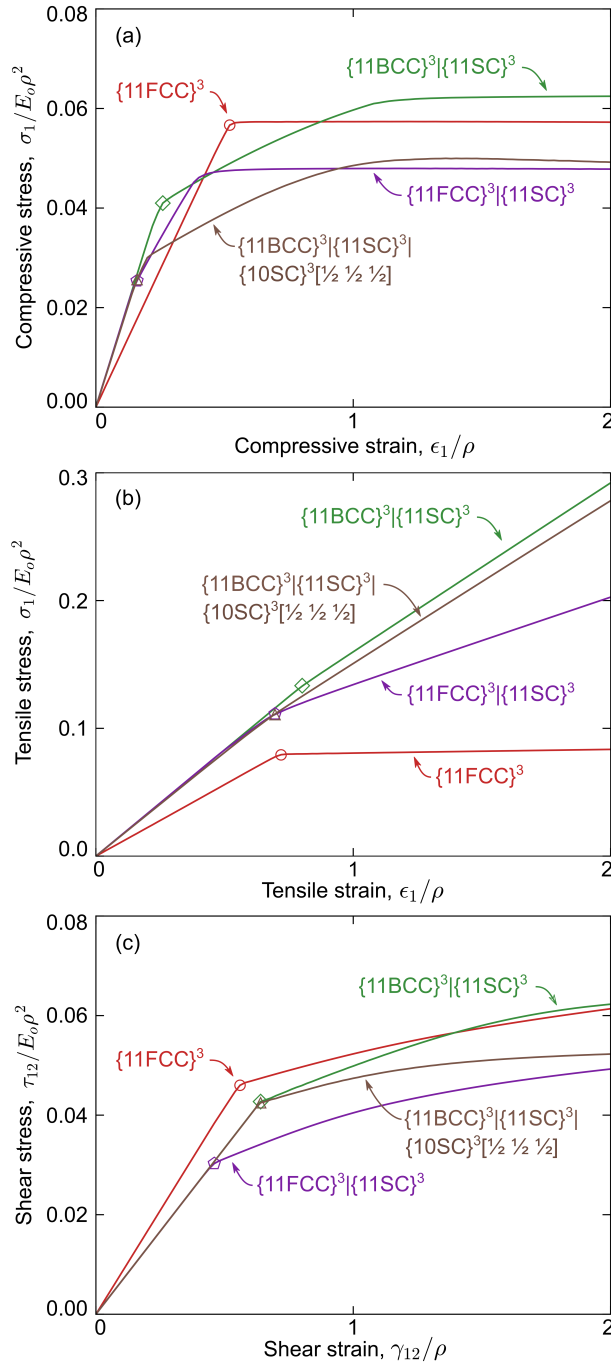
Figure 3.7: Stress-strain responses of trusses subjected to (a) uniaxial compression, (b) uniaxial tension, and (c) pure shear. (See also Videos S3-S6 in Supplementary Information at doi.org/10.1557/jmr.2018.2.)
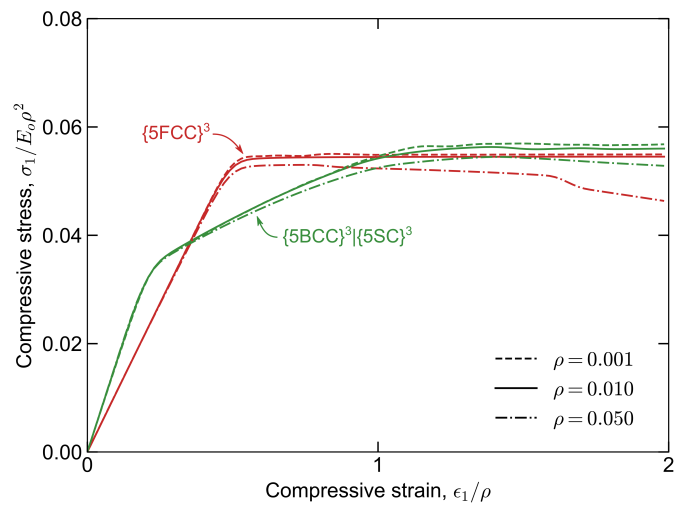
Figure 3.8: Stress-strain responses of trusses subjected to uniaxial compression at relative densities of 0.001, 0.01 and 0.05.
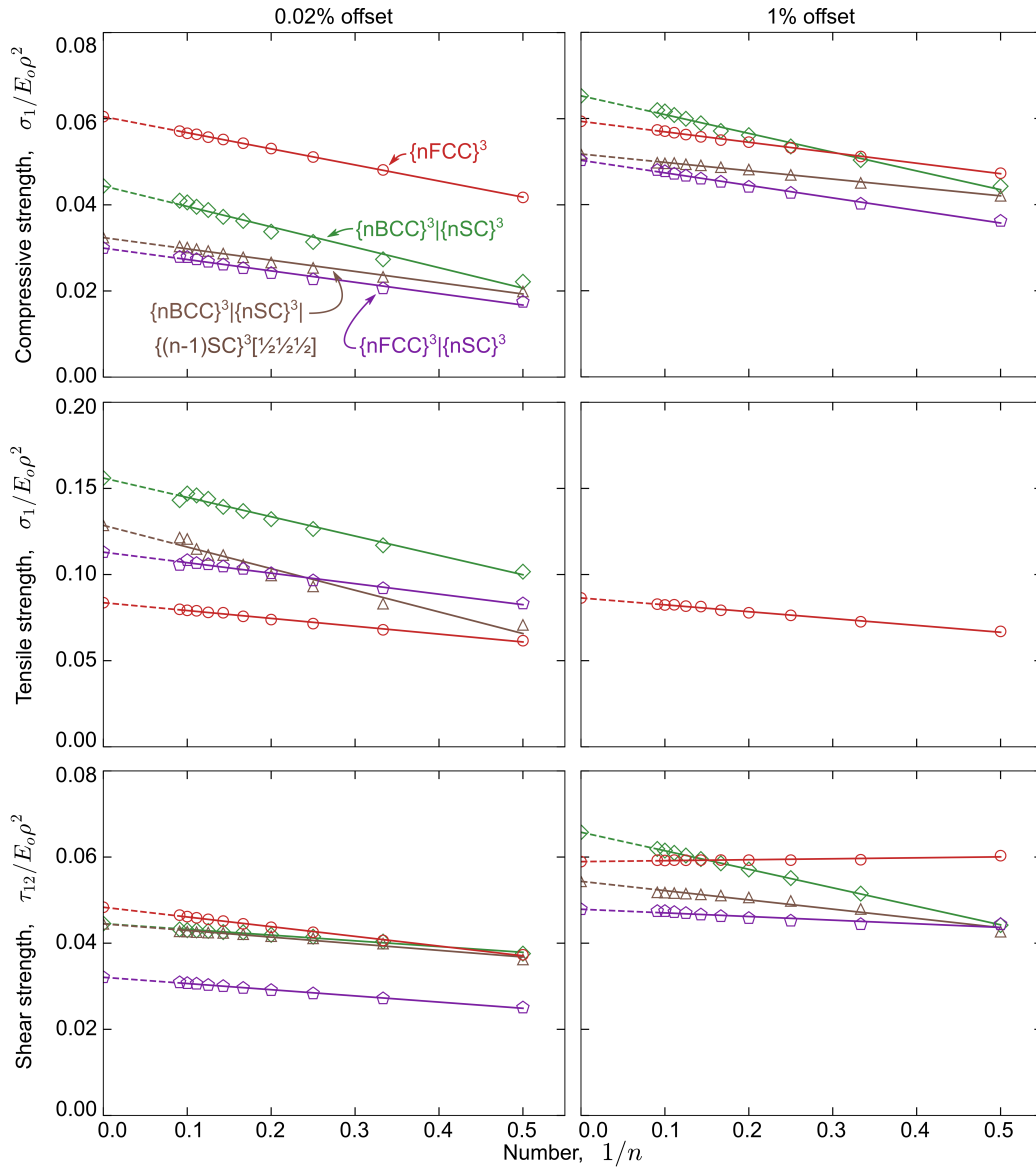
Figure 3.9: Strengths of trusses, defined at 0.02% and 1% offset strains.
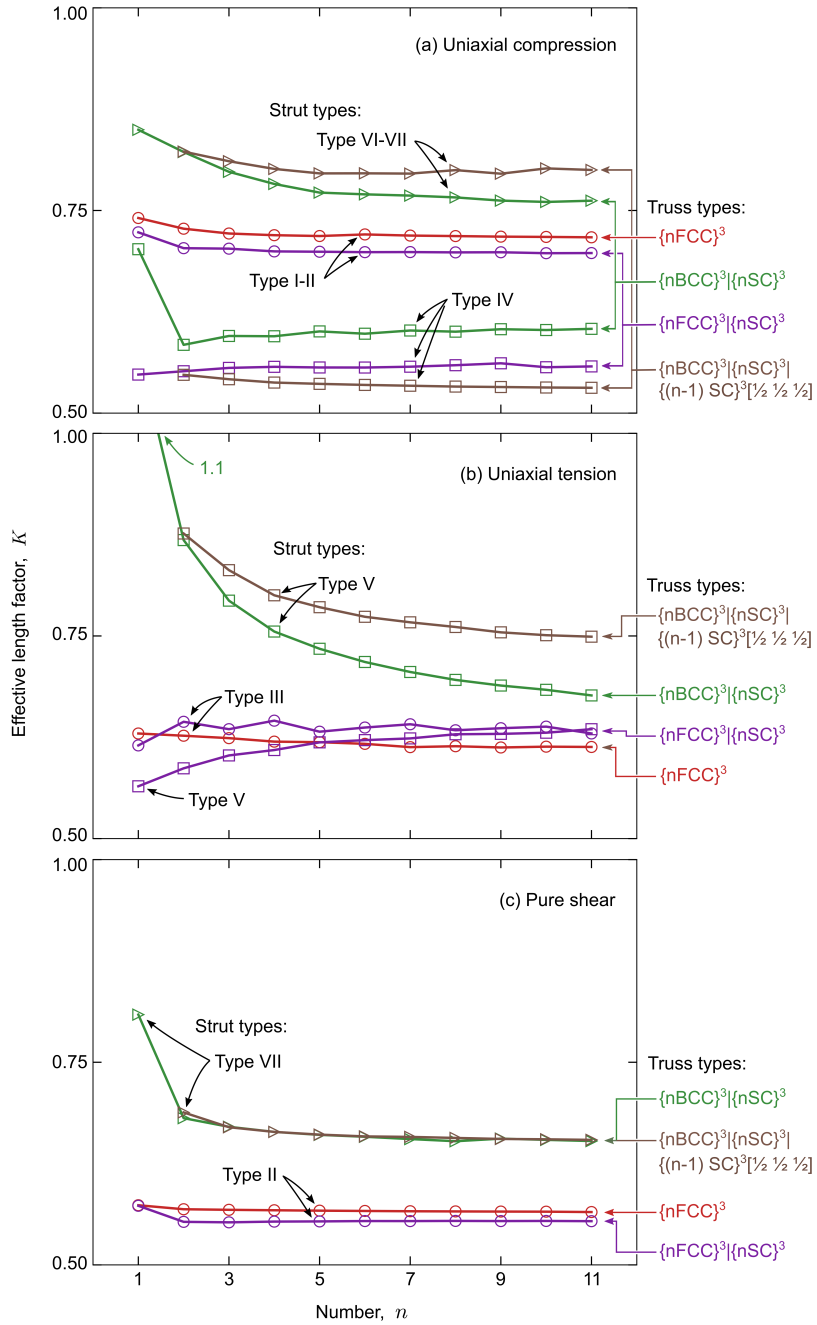
Figure 3.10: Effective length factors of various strut populations when trusses are loaded in (a) uniaxial compression, (b) uniaxial tension and (c) pure shear.

Chapter 4

Effects of nodal fillets and external boundaries on compressive response of an octet truss

4.1 Introduction

Analyses of truss properties (*e.g.* stiffness, strength, toughness) have largely focused on effects of topology in notional truss *materials*: aggregates of many struts with dimensions much smaller than macroscopic scales of interest. A tacit assumption is that the response of the material can be addressed by considering a small

---

This chapter is adapted from a peer-reviewed publication: Ryan M Latture, Ricardo X Rodriguez, Larry R Holmes, and Frank W Zok. Effects of nodal fillets and external boundaries on compressive response of an octet truss. *Acta Materialia*, 2018. Available at: https://doi.org/10.1016/j.actamat.2017.12.060

representative volume element, typically one unit cell. Although this approach is useful in identifying broad trends in behavior and establishing baseline properties, it fails to capture important effects that come into play in real (finite) truss *structures*. The current study focuses on two such effects: (i) the presence of external boundaries and (ii) the geometry of nodal regions at which struts intersect.

Little attention has been focused on the effects of node geometry on truss properties. A cursory inspection of the intersection of struts reveals the issue: the axial loads transmitted through the struts must be transmitted through nodes at which the load bearing area is lower because of the overlapping strut volume. One consequence is that, if no provision is made for the area reduction, yielding (when it dominates) initiates within the nodal regions, not within the struts themselves [24, 50]. Under compressive loads, this localized plasticity may be stable, leading to lateral expansion of the nodes under progressively increasing load and to eventual yielding of the struts [24]. In contrast, under tensile loading, local yielding within the nodes is likely to lead to strain localization before global strut yielding (except in cases where the work hardening rate of the constituent material is unusually high).

Effects of node geometry may be more nuanced in cases in which the strut slenderness ratio is particularly high. Absent yielding, the conditions for strut buckling under macroscopic compression depend on the (elastic) stiffness of the nodal region.

(The effect can be couched in terms of the effective-length factor in Euler buckling theory; a topic we return to in due course.) If node yielding precedes buckling, the constraints acting on the strut ends are reduced and thus the buckling strength is also reduced.

In addition to the effects of reduced cross-sectional area associated with strut intersections, changes in cross-section invariably lead to local stress concentrations. These concentrations may become important in cases in which the struts are loaded in tension and in which the strut material has low tensile ductility. Established design principles for stress concentration reduction employing gradual transitions in area [45], such as those obtained with the use of fillets, are expected to mitigate the problem to some extent.

The principal goal of the present study is to address the effects of nodal fillets and external boundaries on the compressive response of octet trusses made from a hard thermoplastic. The article is structured as follows. Materials and test methods for the experimental study are described in Section 4.2. The structure of a finite element (FE) computational model is presented in Section 4.3. Experimental and computational results of macroscopic stress-strain response and of strut strains and nodal rotations are presented in Section 4.4. This is followed by a discussion of the results and the implications for truss design and failure prediction, in Section 4.5.

4.2 Materials and test methods

Specimens of the specific octet truss $\{2FCC\}^2$, *i.e.* a $2 \times 2 \times 1$ tiling of face-centered cubic unit cells following the truss taxonomy outlined in [68], were fabricated both with and without rounded fillets (Fig. 4.1). The struts were designed to have a circular cross-section with radius $r = 1\,\mathrm{mm}$, length $l = 20\,\mathrm{mm}$ and slenderness ratio $\ell/r = 20$. Fillets (when employed) were designed with a constant radius of $2\,\mathrm{mm}$. The average relative densities, $\bar{\rho}$, were approximately 0.082 and 0.090 for trusses with and without fillets, respectively.

The trusses were printed using a production-level, through-vat stereolithography machine (ProJet 6000, 3D Systems). Print resolution is $50\,\mathrm{\mu m}$ in the build direction (z) and $75\,\mathrm{\mu m}$ in the two transverse directions (x and y). The material used in this study is VisiJet SL Clear, a hard polycarbonate-like material with a reported ultimate tensile strength $\sigma_o = 52\,\mathrm{MPa}$, Young's modulus $E_o = 2.56\,\mathrm{GPa}$ and an elongation at break $\epsilon_f = 6\%$. Auxiliary support structures were automatically generated in 3DManageTM (3D Systems) with an angle constraint of 36°. Upon completion of the build, the fabricated parts were immersed in a bath of isopropyl alcohol (IPA) for 10 minutes. Auxiliary support structures were then manually removed and the parts were re-immersed in the IPA bath for an additional 10 minutes. Following

extraction from the bath, the parts were placed in an ultra-violet finishing chamber for 30 minutes. Photographs of the trusses, including comparisons of the nodal regions in the computer models and in the printed parts, are shown in Figure 4.1. These comparisons attest to the high printing fidelity. Nodal regions of both sample types are accurately reproduced in the finished parts. Surface steps due to the layer-by-layer build process are on the order of the layer thickness ($50\,\mu$m).

Uniaxial compression tests were performed perpendicular to the build direction at a nominal strain rate of $10^{-4}\,\text{s}^{-1}$. Full-field displacement measurements were obtained using 3D digital image correlation (DIC) (Vic-3D, Correlated Solutions, Columbia, SC). Prior to testing, random speckles with a diameter of approximately $0.1\,$mm were applied to the struts in the near surface regions using an airbrush. Images were taken using a pair of digital cameras (Point Grey Research Grasshopper), each with a CCD resolution of 2448×2048 pixels, at a magnification of $32\,$pixels/mm. With this magnification, the area of the entire sample ($\approx 1800\,\text{pixels}^2$) could be monitored during testing while maintaining a minimum of $3\,$pixels/subset in subsequent analyses, as recommended for accurate correlation [56]. The data were analyzed using incremental correlation with a subset size of $23\,$pixels and step size of $2\,$pixels. In total, about 56 struts were imaged and analyzed for each test specimen. The macroscopic compressive strain was obtained from the DIC data using virtual exten-

someters spanning the entire specimen height. The stress was computed from the measured load and the projected area of the entire truss perpendicular to the loading direction. Three specimens of each of the two truss types (with and without fillets) were tested.

Three local deformation metrics were computed from the DIC data: (i) axial strut strains, ϵ_a, (ii) bending strut strains, ϵ_b, and (iii) nodal rotations, θ_r. Axial and bending strut strains were computed from the displacements of 50 sample points along the centerline of each strut. Axial strains were calculated from the total length of the line segments joining the sample points in deformed and undeformed configurations, neglecting segments within one strut diameter of a node. To determine bending strains, first a three-dimensional parametric curve, $f(t)$, was fit to the 50 sample points, *i.e.* $f(t) = (x(t), y(t), z(t))$ where t is a non-dimensional position coordinate between the strut endpoints ($0 \leq t \leq 1$). Strut curvature, defined by $\kappa = \frac{||f' \times f''||}{||f'||^3}$ (primes denoting derivatives with respect to t), was computed and averaged over the range $0.1 \leq t \leq 0.9$. Bending strains were calculated as the product of mean strut curvature and strut radius. The two strains were further combined to obtain the strut-averaged maximum and minimum principal strains: $\epsilon_{max} = \epsilon_a + \epsilon_b$ and $\epsilon_{min} = \epsilon_a - \epsilon_b$. Finally, nodal rotations were calculated for all nodes on the external surface (plane perpendicular to the viewing direction), from vectors joining

102

material points about 2 mm on either side of each node.

The struts were subsequently sorted in two ways: (i) by orientation with respect to loading direction (x) and build direction (z), and (ii) by proximity to faces, edges and corners. On the basis of orientation, three unique strut types exist: (i) those along [110] directions, denoted type I, (ii) [101], denoted type II, and (iii) [011], denoted type III. The first two are at 45 degrees to the loading direction whereas the third is perpendicular. With respect to location, distinctions are made between *corner* struts (those that have one end at a truss corner), *edge* struts (one end at a truss edge), *face* struts (fully contained on an external face) and *bulk* struts. The struts are distinguished by the nodal connectivities at their two ends: 3 and 8 for corner struts, 5 and 8 for edge struts, 8 and 8 for face struts, and 8 and 12 for bulk struts. (Because there is only one unit cell in the build direction, all bulk struts have one end on a face. For larger trusses, nodal connectivity for bulk struts would be 12 at both ends.)

4.3 Finite element analysis

The macroscopic response of the trusses was simulated using the commercial finite element code Abaqus/Explicit. The principal goal was to identify the effects

of external boundaries (edges, corners and faces) on strut strains, strut buckling and truss failure. A secondary objective was to probe the effects of nodal stiffness on truss response.

For these purposes, the truss was discretized using Timoshenko beam elements with circular cross-section. Each strut consisted of 40 elements. Strut dimensions were selected to yield a strut slenderness ratio equal to that in the tested trusses, *i.e.* $l/r = 20$. The parent material was assumed to be linear-elastic with Young's modulus $E_o = 2.56\,\text{GPa}$, shear modulus $G_o = 0.93\,\text{GPa}$ and mass density $\rho_o = 1170\,\text{kg/m}^3$. Finite element simulations of compressive response were performed for three scenarios, distinguished by the assumed character of the nodal regions. These include: (i) pinned nodes, (ii) locally rigid nodes, *i.e.* without relative movement of the strut ends that meet at the node, and (iii) locally rigid nodes with rigid strut segments within one strut radius of the nodes (to account for finite material at the nodes). In the latter case, the slenderness ratio of the *deformable* strut segments is reduced to $(l - 2r)/r = 18$.

Geometric imperfections, based on the first three buckling modes, were introduced in according to the geometric sequence defined by Equation 3.2. Here, B was taken to be 0.001. This amplitude was chosen such that the maximum imperfection was approximately equal to the printing resolution of the machine used to fabricate

the test specimens.

Uniaxial compression was simulated by prescribing nodal velocities along the loading (x) direction on one face of the FE model, *i.e.* velocity, $\dot{u} = du/dt = l_x \dot{\epsilon}$ at $x = l_x$ where l_x is the truss length along the x-axis. Velocities were selected to yield quasi-static strain rates ($|\dot{\epsilon}| \leq 10^{-3}\,\text{s}^{-1}$). The resulting ratio of kinetic to potential energy was less than 10^{-3} for all time steps in each simulation, confirming quasi-static loading. The equations of motion were integrated using explicit central differences with fixed timestep until reaching a compressive strain, ϵ_1, of 0.05. Rigid body motion was prevented by setting $w = 0$ for the node at $(0, l_y, 0)$ and fixing translational degrees of freedom of a single node at the origin, *i.e.* $u = v = w = 0$ at $(0, 0, 0)$ (v and w being displacements along y- and z-axes, respectively). The FE calculations were used to ascertain the macroscopic stress-strain response, the average axial and bending strains in individual struts, and the nodal rotations.

To assess the generality of the boundary effects operative in the specific truss $\{2FCC\}^2$, additional FE calculations were performed for cubic arrays of the unit cell, designated $\{nFCC\}^3$, with rigid nodes, a strut slenderness ratio of 20, and n varying from 2 to 11. Uniaxial compression was simulated in a manner analogous to that used for the $\{2FCC\}^2$ truss.

4.4 Experimental and computational results

4.4.1 Macroscopic response of $\{2FCC\}^2$ trusses

Figure 4.2 shows the measured compressive stress-strain curves and those obtained from FE calculations. (Corresponding videos are provided in Supplementary Information at doi.org/10.1016/j.actamat.2017.12.060.) The measured curves for each of the two truss types exhibit minimal variation up to the stress maximum. Moreover, the Young's moduli for both truss types are virtually identical: $E = 27\,\mathrm{MPa}$. In normalized form, the modulus is $E/\bar{\rho}E_o \approx 0.13$. By comparison, the theoretical value, obtained from a statics analysis of a truss with periodic boundary conditions and infinitesimal nodes, is $E/\bar{\rho}E_o = 1/9 \approx 0.11$ [12]. The slight difference is attributable to the finite sizes of nodes and thus the slightly-reduced effective strut lengths in the current test specimens.

The stress-strain curves for specimens with and without filleted nodes begin to diverge at a compressive strain of about 0.01. At larger strains, specimens without filleted nodes exhibit a progressive reduction in tangent modulus. In contrast, specimens with filleted nodes continue to exhibit linear response up to a strain of about 0.02. Thereafter a progressive reduction in tangent modulus is obtained. In both cases, the tangent modulus gradually and smoothly approaches zero. As described

later, this response is attributable to bending and buckling of certain struts. At or very near the stress maximum, strut fracture begins, at a strain $\epsilon_1 \approx 0.038$. But, because of greater softening in the trusses without filleted nodes, these trusses experience a peak stress about 20% lower than that of the filleted trusses. In both cases it appears that the conditions for large-scale strut buckling and for onset of tensile strut fracture are nearly coincident.

By comparison, the pinned-node FE result displays non-linearity and large-scale buckling at a strain of about 0.02 and attains a plateau stress of about 0.4 MPa: only half of the peak for the filleted truss. In contrast, the rigid-node FE result for the same geometry ($l/r = 20$) initially follows the same response but reaches a plateau stress that is roughly twice that of the pin-noded truss and in good agreement with that measured on the filleted truss. Introducing rigid strut segments in the near-node regions has the effect of increasing the initial tangent modulus; this modulus closely matches the measured values for the filleted trusses. Buckling in the latter simulations begins at a strain of about 0.035; at slightly higher strains, a plateau stress of about 1 MPa is attained. The FE results for pin-noded trusses and for trusses with rigid nodes and rigid strut segments near the nodes neatly bound the two sets of experimental results. Overall, the FE result for rigid nodes and struts that are elastic everywhere most closely resembles the shapes of the measured stress-strain

curves.

4.4.2 Strains, rotations and failure locations in $\{2FCC\}^2$ trusses

Variations in axial and bending strut strains with applied compressive strain ϵ_1 are plotted in Figures 4.3 and 4.4, respectively. The results are sorted by strut types (I, II and III in top, middle and bottom rows) and by strut location (color-coded lines). The three columns in each figure, from left to right, correspond to measured strains for specimens without and with fillets and those from rigid-node FE calculations. (These FE results are very similar to those obtained for the case of rigid nodes and short rigid strut segments near the nodes; thus the latter are not presented here.) Figure 4.3 also contains lines representing the analytic predictions for a truss with periodic boundary conditions and infinitesimal nodes: $\epsilon_a/\epsilon_1 = -1/3$ for type I and II struts and $\epsilon_a/\epsilon_1 = 1/3$ for type III struts [32]. Three-dimensional renderings of the computed axial strut strains at select strain levels are shown in Figure 4.5. Finally, a summary of maximum and minimum principal strut strains at macroscopic compressive strains $\epsilon_1 = 0.02$ and 0.038 are presented in the form of a box-and-whisker chart in Figure 4.6.

At small strains ($\epsilon_1 \leq 0.02$), the measured axial strut strains, on average, follow the trend predicted by the analytic predictions: $\epsilon_a/\epsilon_1 = -1/3$ for type I and II struts and $\epsilon_a/\epsilon_1 = 1/3$ for type III struts. But, because of the varied proximities of struts to corners, edges and faces, the axial strains vary from strut to strut, by factors of 2 to 3 from minimum to maximum. The FE results show analogous (but slightly smaller) variations. At larger applied strains, the variations increase, with some struts undergoing more rapid and others less rapid increases in strain. Despite the variations, the axial strains in individual struts from the FE calculations reach a plateau level once the struts begin to buckle, at a compressive strain of about 0.032.

Among type III struts, those situated along the mid-plane (indicated by arrows in Figure 4.3) experience the highest tensile strains, reaching values of about twice the analytic prediction: $\epsilon_a/\epsilon_1 \approx 2/3$. Indeed, these are the struts that usually fracture first (Figure 4.7), at the stress maximum. The peak axial strut strains differ only very slightly in the two truss types: 0.024-0.026 in unfilleted struts and 0.023-0.031 in filleted struts.

The FE results similarly show that these type III struts experience the largest strains (shown in Figure 4.5). Prior to buckling, the computed strut strain in the most critical regions is $\epsilon_a/\epsilon_1 = 1/2$: 50% greater than the nominal value for bulk struts. The predicted peak axial strain in type III struts ($\epsilon_a \approx 0.018$) at the onset of

109

buckling of type I and II struts is only slightly lower than that measured experimentally ($\epsilon_a \approx 0.025$). The bending strains in type III struts (first column in Figure 4.4) are the lowest among the three strut types. The edge struts on the mid-plane in particular experience negligible bending.

The measured bending strains in type I and II struts in the *unfilleted* struts are the greatest and span the largest range (by almost an order of magnitude, from about 0.002 to 0.02). The peak values are obtained in corner struts (indicated by arrows in top row of Figure 4.4). These are also the struts with the lowest nodal connectivity (3 and 8). *Filleted* type I and II struts also experience bending, but with peak values only about half those obtained in the unfilleted struts. Moreover, the bending strains for the filleted struts are in closer agreement with the rigid-node FE predictions. These results indicate that filleted nodes are stiffer than unfilleted nodes and therefore reduce somewhat the degree of bending.

Effects of node geometry and external boundaries on truss deformation are also manifested in the transverse strut displacements, illustrated in Figure 4.8. Notably, type I and II corner struts experience the greatest transverse displacements; in the examples in Figure 4.8(a), the maximum displacement of a corner strut (AB) is typically about twice that of the adjoining co-linear face strut (BC). Moreover, the peak displacements of these two struts in the unfilleted struts are about twice those

obtained in the filleted struts. Similar trends are obtained from the FE results for rigid-node trusses (Figure 4.8(b)). Nodal rotations on the external truss face, plotted on Figure 4.9, exhibit similar trends: greatest at the corner nodes and, in the unfilleted nodes, about twice those in the filleted nodes.

Closer examinations of the tested trusses reveal the locations of strut fracture (Figure 4.10). In the unfilleted trusses, strut fracture occurs *at* the nodes and, in some instances, leads to shattering of the nodes and some of the adjoining struts. In contrast, in the filleted trusses, strut fracture occurs at some distance from the node itself, near the end of the fillet.

4.4.3 $\{nFCC\}^3$ trusses

FE results for *cubic* arrays of the octet truss, notably $\{nFCC\}^3$ (with n=2 to 11), are presented in Figures 4.11–4.14. The macroscopic compressive stress-strain curves are essentially independent of n; only minor variations are observed in the transition from the linear-elastic domain to the buckling domain (Figure 4.11).

Distributions in the minimum and maximum principal strains for $n = 2 - 11$ and the locations of struts with minimum and maximum strains for $n = 5$, all in the linear-elastic domain, are shown in Figure 4.13. These results are also essentially

independent of n. Although the maximum principal strains in type III struts are, on average, the same as the analytic prediction ($\epsilon_{\max}/\epsilon_1 = 1/3$), the values obtained in the edge struts reach $\epsilon_{\max}/\epsilon_1 \approx 0.50$: the same as those in the $\{2FCC\}^2$ truss. This is further evidenced by the 3-dimensional renderings of the axial strut strains in Figure 4.12. In contrast, the minimum principal strains in type I and II struts are, on average, of greater magnitude than the analytic prediction ($\epsilon_{\min}/\epsilon_1 = -1/3$), a consequence of slight strut bending. Their peak values, $\epsilon_{\min}/\epsilon_1 \approx -0.57$, are obtained at the truss edges (as indicated in Figure 4.13(b)) and are the same as those in the $\{2FCC\}^2$ truss.

The evolution of axial and bending strains in representative struts that experience the minimum and maximum principal strains as well as those in the bulk of the $\{5FCC\}^3$ truss are plotted in Figure 4.14. These results are quantitatively comparable to those obtained for the $\{2FCC\}^2$ truss (the latter shown in Figures 4.3(c) and 4.4(c)).

4.5 Discussion

4.5.1 Synopsis of key findings

The main role of fillets in the current truss system is to enhance the nodal stiffness and, in turn, reduce the degree of softening due to bending of type I and II struts. In both truss types, the peak compressive stress is approached smoothly, consistent with the progressive nature of strut buckling. However, large-scale buckling is preceded by tensile fracture of type III struts intersecting the truss edges. Interestingly, the peak axial strains in these type III struts at the onset of strut fracture appear to be insensitive to the presence of fillets. Evidently either the fillets employed here play only a minor role in alleviating the stress concentrations at the nodes at which tensile fracture occurs or the failure strain is insensitive to these stress concentrations. A further possibility is that the stress concentrations of surface steps resulting from the manufacturing process may control the strut failure strain.

Strut strains at external boundaries generally differ from those in the bulk. Type I corner struts, with nodal connectivities of only 3 and 8, experience the greatest amount of bending and are most prone to buckling. Type III edge struts, with nodal connectivities of 5 and 8, experience the greatest axial (tensile) strains. Prior to buckling, they are 50–100% greater than the nominal value and are usually the first

to break.

Further analyses of these results and discussion of their implications in the context of competing failure modes follow.

4.5.2   Failure by buckling

Buckling strengths can be interpeted in the context of Euler buckling thoery. Here the axial strut strain for buckling is predicted to be proportional to E and $(r/\ell)^2$, through a proportionality constant that depends on the effective-length factor, K. The theoretical prediction for the octet truss can be couched in terms of a normalized macroscopic buckling stress: $\sigma_c/E_o = \pi^3(r/\ell)^4/K^2\sqrt{2}$. For pinned nodes, the effective-length factor is $K = 1$ [12] and thus the buckling stress reduces to $\sigma_c/E_o = \pi^3(r/\ell)^4/\sqrt{2}$. For $\ell/r = 20$ and $E_o = 2.56\,\mathrm{GPa}$, the critical stress is $\sigma_c = 0.35\,\mathrm{MPa}$. By comparison, the buckling stress obtained in the present FE calculations for pinned nodes is $\sigma_c \approx 0.38\,\mathrm{MPa}$ (essentially the same as the analytic prediction).

The preceding analysis can be further used to infer the volume-averaged effective-length factor for rigid-node trusses. Since the strength is proportional to $1/K^2$ and the strength ratio of rigid and pinned trusses from Figure 4.2 is about 2, the inferred

effective-length factor for the struts within the rigid-node truss is $K = 1/\sqrt{2} \approx 0.71$. By comparison, if the nodes were *globally* rigid – with zero rotation and zero displacements transverse to the strut axis – the effective-length factor would be $K = 0.5$. Even with the addition of short rigid strut sections in the nodal region (to represent constraints of a finite node volume), the nodes are still free to rotate and, as a result, the inferred effective-length factor is only moderately lower: $K \approx 0.63$. Evidently, although the nodes (and in some instances portions of the strut) are treated as being *locally* rigid in the FE calculations, the nodes behave in a more compliant fashion globally, as manifested in an increase in the inferred value of K. Nevertheless, the value of K remains well below that for pin-noded trusses (1.0).

The measured buckling strengths can be interpreted in a similar fashion (assuming that the peaks are indeed close to the plateau buckling stress). Comparing these strengths with the predicted buckling stresses for pinned trusses (wherein $K = 1$), the inferred effective-length factors are $K \approx 0.66$ and $K \approx 0.73$ for trusses with and without fillets, respectively. These lie near the mean of the values for *globally* rigid nodes and pinned nodes (0.5 and 1.0).

External boundaries and truss size do not play significant roles in the buckling process. Despite some strain differences in type I and II struts in the boundary regions relative to those in the bulk as well as slight differences in the transition

115

from the linear-elastic domain to the buckling domain, the plateau buckling stress remains the same.

4.5.3   Failure by strut fracture or yielding

External boundaries play a more significant role in tensile strut fracture (especially in brittle polymers). As previously noted, the peak axial strut strains are 50–100% greater than nominal values. In small truss structures, a single fracture event may lead to a cascade of further fractures and global failure (as observed in the current truss system). Larger structures may tolerate a greater number of fracture events before catastrophic fracture. The absence of fillets would exacerbate these effects.

If, instead, failure were to initiate by yielding or by combined yielding and subsequent buckling, the pertinent strut metric would be the minimum principal strain in type I and II struts; as evidenced in Figure 4.6, its magnitude is greater than the maximum principal strain in type III struts. This arises from the bending strains in these struts which, on average, are $\epsilon_b/\epsilon_1 \approx 1/9$. (Although usually neglected in the analysis of octet trusses, bending strains are not altogether insignificant in comparison to axial strains ($|\epsilon_b/\epsilon_a| \approx 1/3$), especially in the context of yield initiation. They would therefore also be relevant to low cycle fatigue failure.) The computed

peak value at small applied strains is $\epsilon_{min}/\epsilon_1 = -0.55$ (in type II struts). The measured values are somewhat greater, reaching $\epsilon_{min}/\epsilon_1 = -0.72$ in type I struts. Once the struts begin to bend appreciably, at higher applied strains, the computed peak values are $\epsilon_{min}/\epsilon_1 = -0.60$ and those measured experimentally are as great as $\epsilon_{min}/\epsilon_1 = -1.1$ (about 3 times the nominal value). Depending on the sensitivity of the subsequent structural response (especially strut buckling) to the onset of yielding in the most critically-strained struts, the load-bearing capacity of finite trusses may be lower than that expected of an infinite truss.

4.6   Conclusions and implications

The key conclusions follow:

(i) Circular nodal fillets in octet trusses enhance the bending stiffness of the strut ends. In turn, the degree of softening due to strut bending is reduced and the stress for buckling is increased (by about 20%).

(ii) The axial strut strain for tensile rupture in the material used in the current study does not appear to be affected significantly by the presence of fillets. Whether this result is a general one, applicable to other classes of materials used in AM, remains to be established.

(iii) Boundary effects in octet trusses lead to elevations in local strut strains, a result of reduced local nodal connectivity. Most importantly, the peak tensile strains in type III struts are elevated almost 2-fold relative to nominal values.

(iv) Boundary effects persist to depths comparable to the unit cell size. This result is consistent with previous findings [19, 32, 35].

In light of the findings regarding tensile strut fracture and effects of external boundaries, two potential strategies for enhancing the performance of the current truss system are envisioned. One would involve modifications to truss *geometry* in the near-boundary region, especially along the truss edges. These could include increases in the diameter of type III struts and the fillet radii. A second strategy would involve changes in local truss *topology*. For example, the octet truss could be locally augmented by layers or columns of simple cubic (SC) trusses, interlaced with the octet truss and sharing the same nodes. In effect this would comprise a local *compound* truss of the form $\{FCC\}|\{SC\}$. Assessment of the efficacy of these strategies would require consideration of the increased mass of near-boundary enhancements. For example, if modifications were made at constant mass, the strut diameter in the truss interior would need to be reduced to offset the additional mass allocated to the near-boundary regions. A problem of this nature would likely lend itself well to established optimization algorithms. Additionally, additive manufacturing would

118

enable these designs to be readily put into practice.
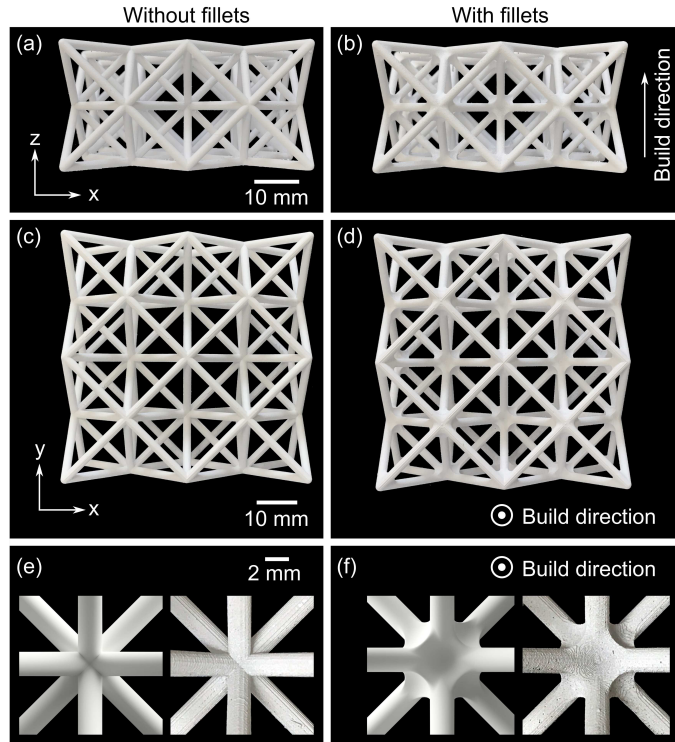
Figure 4.1: (a-d) Photographs of printed trusses with and without filleted nodes viewed in two orientations. (e,f) Higher magnification views of the nodal regions in computer models (left image in each pair) and in the printed parts (right image in each pair).
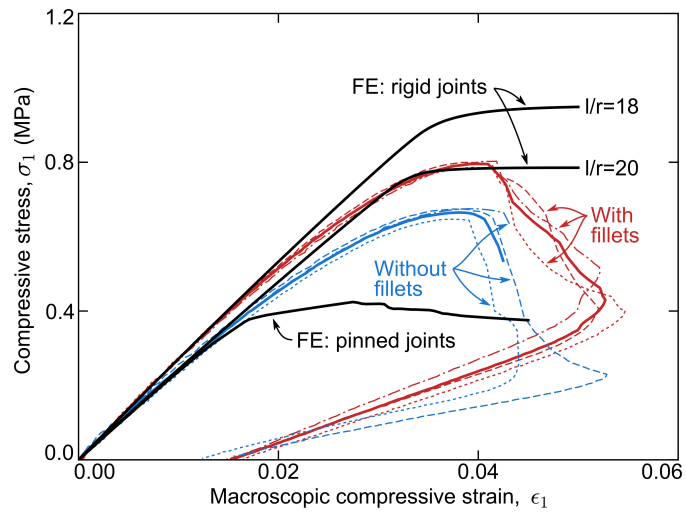
Figure 4.2: Compressive stress-strain responses of trusses with and without filleted nodes and from FE calculations. Dotted and dashed lines represent measured responses of individual test specimens whereas the solid colored lines represent averages. (See also Videos 1 and 2 in Supplementary information at at doi.org/10.1016/j.actamat.2017.12.060.)
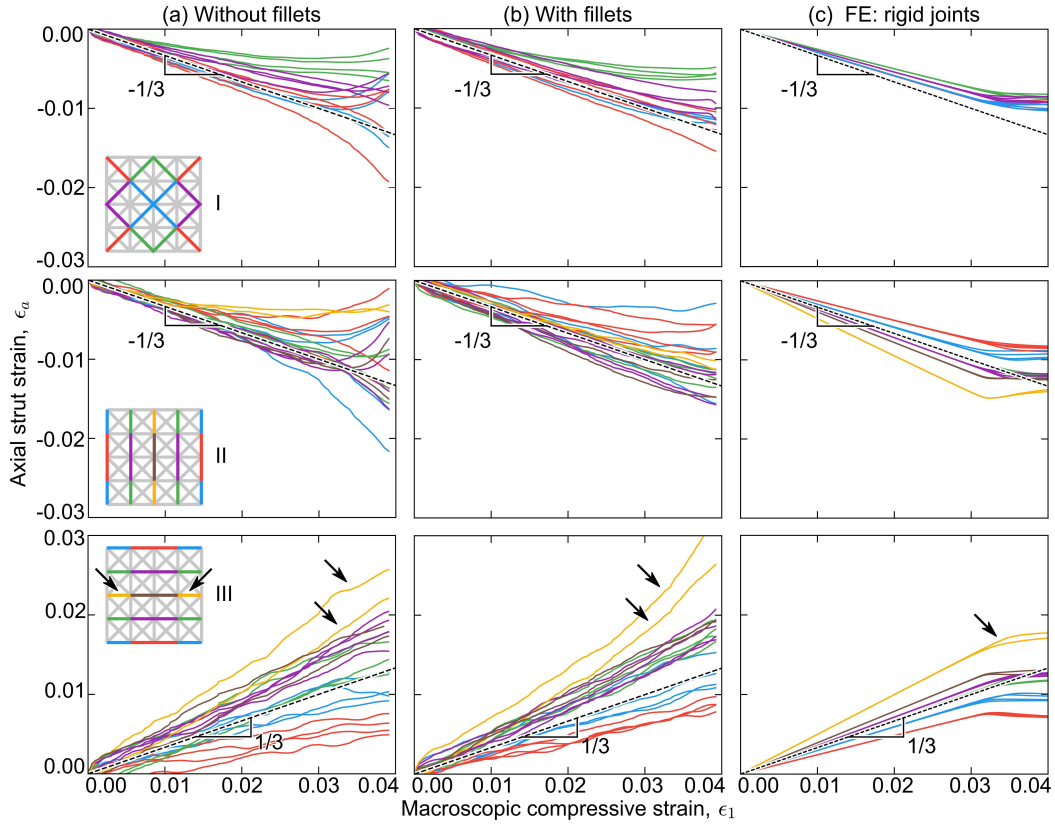
Figure 4.3: Evolution of measured axial strut strains in the three strut types (I, II and III) in trusses with and without filleted nodes as well as results from FE calculations (assuming rigid nodes). Results are further sorted on the basis of strut locations relative to free boundaries. Line colors correspond to strut colors in insets in (a). Dotted lines (with slopes of $1/3$ and $-1/3$) represent analytic predictions for periodic boundary conditions and infinitesimal nodes. Arrows in bottom row indicate type III edge struts that experience the greatest axial strain and are the ones that rupture first.
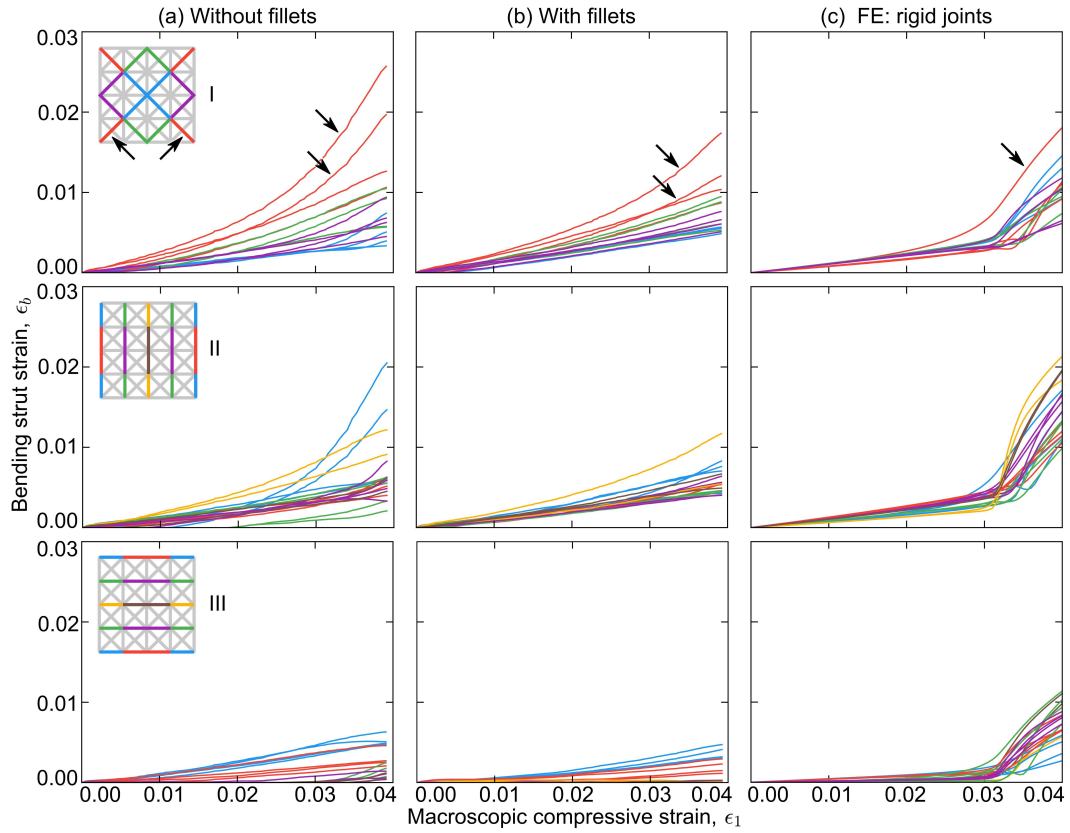
Figure 4.4: Evolution of measured bending strut strains in the three strut types (I, II and III) in trusses with and without filleted nodes as well as results from FE calculations. Line colors correspond to strut colors in insets in (a). Arrows in top row show strut that experience the greatest bending strain and are most prone to buckling.
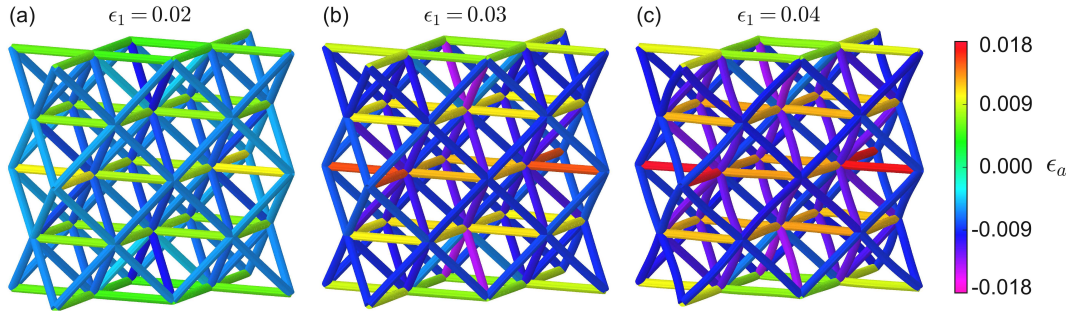
Figure 4.5: Three-dimensional renderings of the computed axial strut strains in the $\{2FCC\}^2$ truss at the macroscopic compressive strains indicated. (See also Video 3 in Supplementary information at doi.org/10.1016/j.actamat.2017.12.060.)
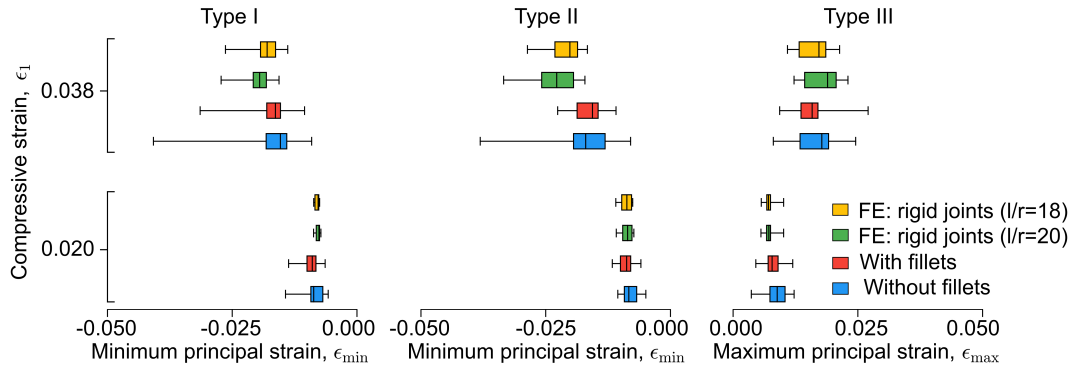
Figure 4.6: Summary of maximum and minimum principal strut strains at macroscopic compressive strains of 0.02 and 0.038. Central lines represent means, boxes contain the middle two quartiles of data, and outlying hash marks represent minimum and maximum values.
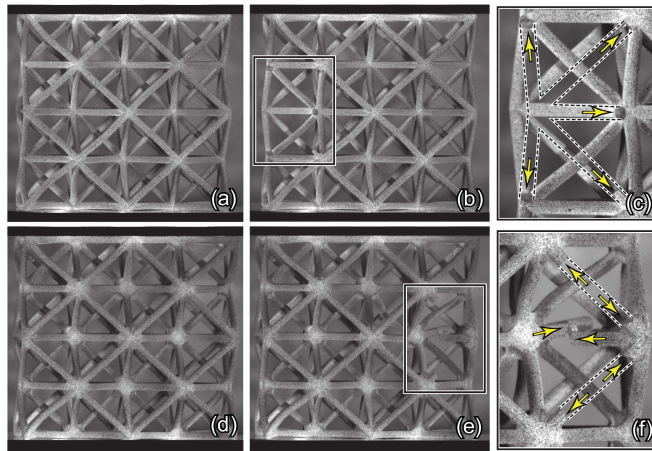
Figure 4.7: Images of trusses (a-c) without and (d-f) with fillets, essentially at the load maximum, immediately before and after strut rupture begins. In both cases, fracture of an edge type III strut leads to secondary fractures, a consequence of the dynamic nature of the fracture process. Close-up views (c, f) show strut fracture locations (arrows) and struts that had been ejected (indicated by dashed lines).
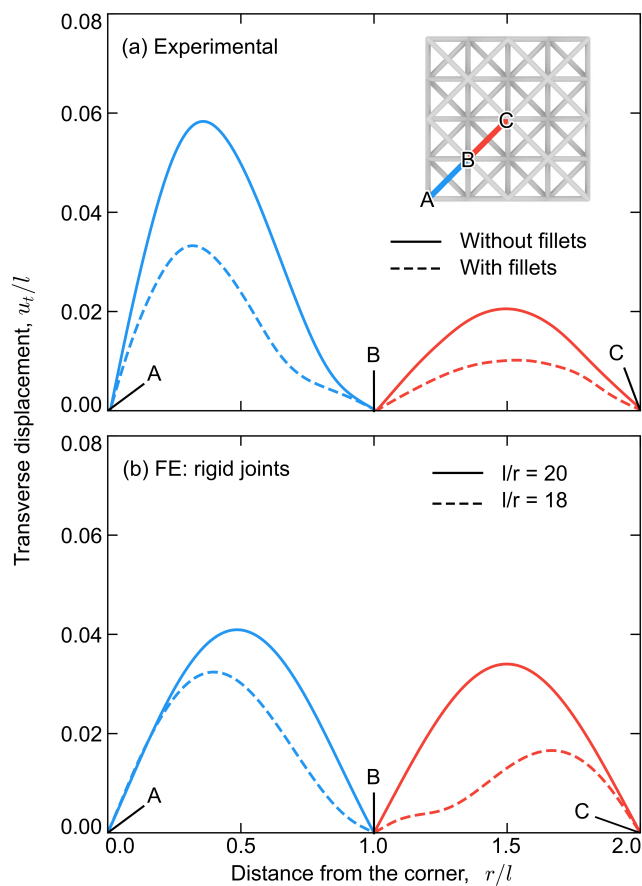
Figure 4.8: Transverse displacement profiles of two co-linear struts emanating from the bottom left corner of the truss: (a) experimental results and (b) finite element simulations. Each corresponds to the respective maximum stress for that truss.
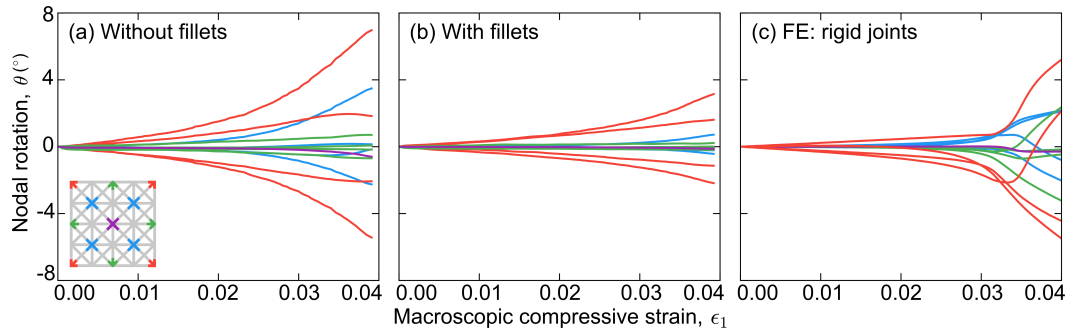
Figure 4.9: a, b) Nodal rotations on the external faces in the two truss at their respective peak stress and (c) those obtained from rigid-node FE calculations. Line colors correspond to node colors in the inset in (a).
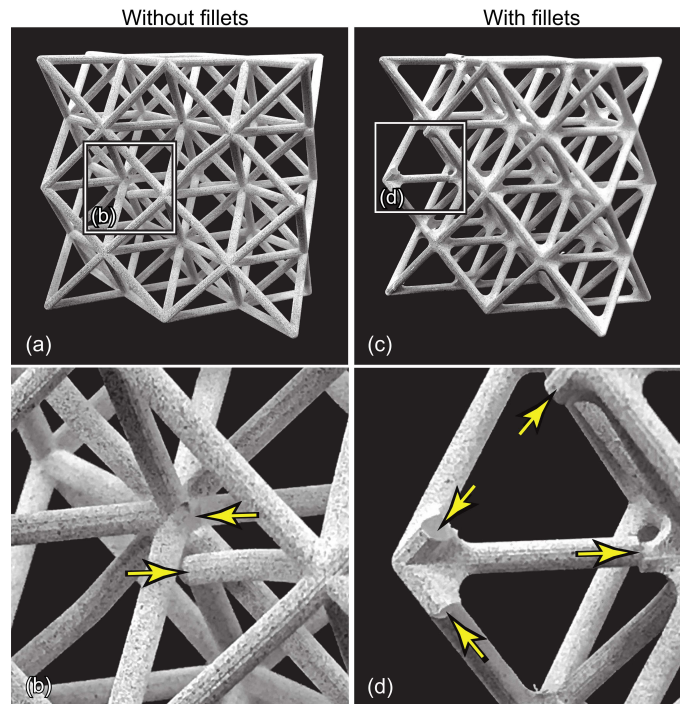
Figure 4.10: Images of specimens after compression tests. Fracture locations indicated by arrows in (c) and (d). In the specimen without filleted nodes, fracture occurs at the nodes; in contrast, in the specimen with filleted nodes, fracture occurs a short distance from the nodes, close to the end of the node fillet.
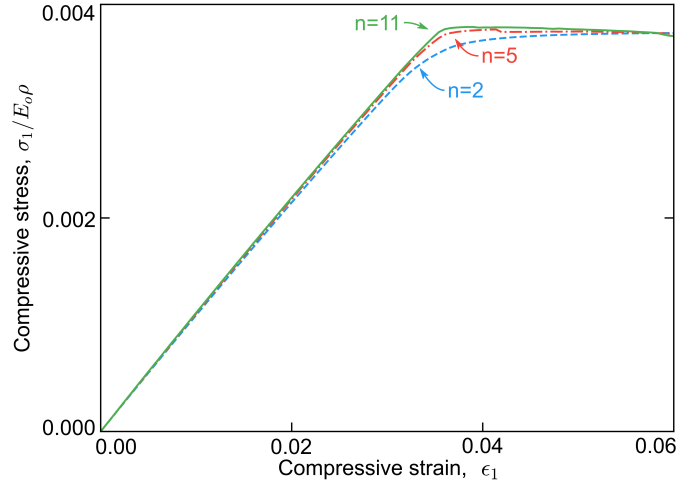
Figure 4.11: Compressive stress-strain response of the $\{nFCC\}^3$ truss for $n = 2$, 5 and 11.
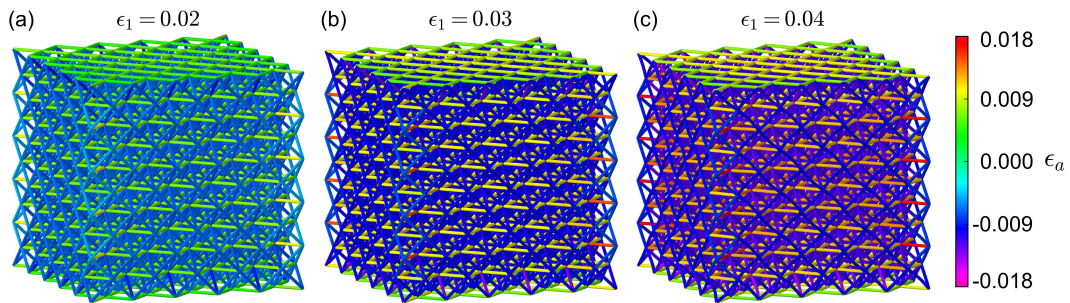
Figure 4.12: Three-dimensional renderings of the computed axial strut strains in the $\{5FCC\}^3$ truss at the macroscopic compressive strains indicated. (See also Video 4 in Supplementary information at doi.org/10.1016/j.actamat.2017.12.060.)
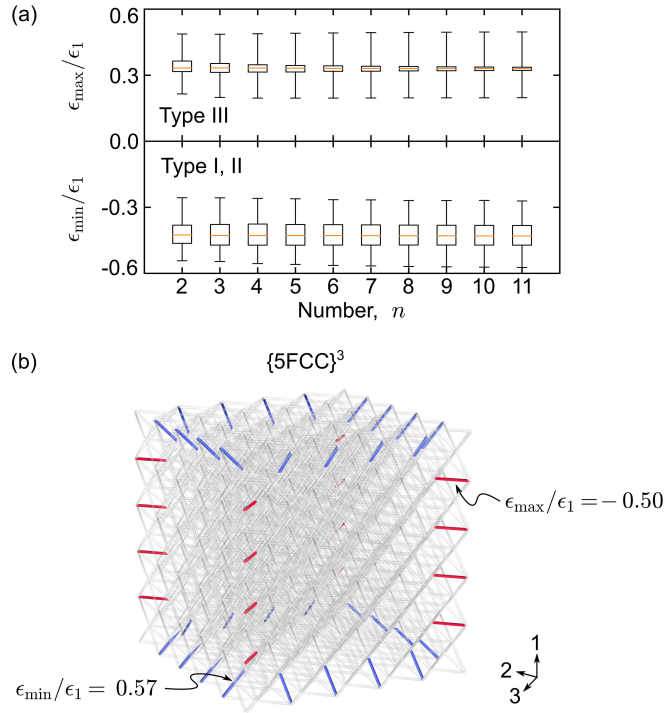
Figure 4.13: Effects of truss size on macroscopic response and strut strains in $\{nFCC\}^3$ trusses. (a) Minimum and maximum strut strains prior to strut buckling (at $\epsilon_1 = 0.01$). Central lines represent means, boxes contain the middle two quartiles of data, and outlying hash marks represent minimum and maximum values. (b) Locations of struts with minimum and maximum principal strains (also at $\epsilon_1 = 0.01$).

129
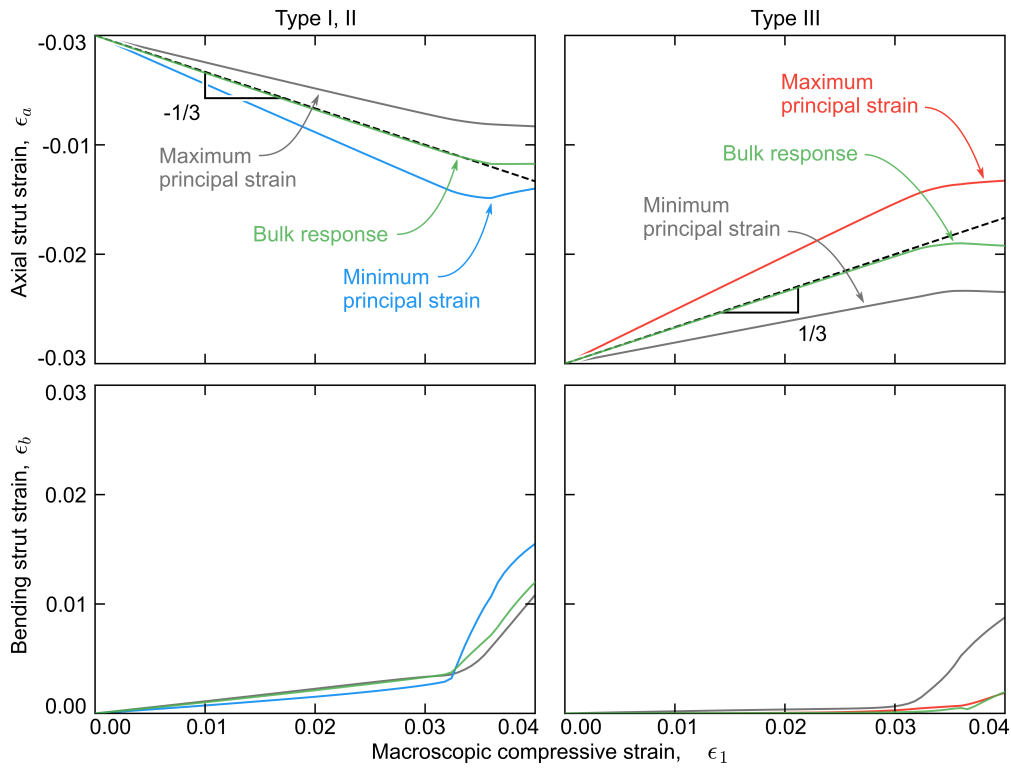
Figure 4.14: Axial and bending strains for struts with the maximum and minimum strut strains within each strut type as well as struts in the bulk of the $\{5FCC\}^3$ truss. Dotted lines (with slopes of $1/3$ and $-1/3$) represent analytic predictions for periodic boundary conditions and infinitesimal nodes.

Chapter 5

Defect Sensitivity of Truss Strength

5.1 Introduction

The present chapter addresses one specific aspect of truss performance: that of defect sensitivity of compressive strength. It is motivated by numerous studies showing that truss properties often fall short of theoretical predictions, a consequence of defects and imperfections introduced during manufacturing. In one study, effects of strut waviness in woven metal trusses were found to produce a knock-down in compressive stiffness and compressive strength of about 20% relative to those obtained in corresponding structures with straight struts [46]. Such effects are well-predicted by analytical and finite element models that account for deviations in strut orientations relative to their ideal values and the resulting axial and bending stresses produced

131

within these struts. In another, variations in strut geometry in hollow-microtube truss structures were measured and the results used to build a stochastic model of geometric imperfections [52]. In turn, through Monte Carlo simulations and finite element analyses, the critical buckling loads were computed for many instantiations of strut geometry. The results were used to rationalize large deviations in strength from the theoretical values for perfectly uniform trusses as well as large statistical strength variations from sample to sample. Yet other studies have found imperfections in the form of progressive changes in strut diameter and local strut properties in polymeric trusses made by a self-propagating photocuring method [50, 51]. Analogous effects of geometric imperfections on the elastic response of solid-strut Ti-alloy trusses fabricated by selective electron beam melting have also been reported [6]. In another computional study, the stiffness and yield strength of an octet-truss panel were found to decrease approximately linearly with the fraction of struts removed from the truss [63]. Similar results have been reported for the effects of missing wall members on the modulus, elastic buckling strength and plastic collapse strength of hexagonal honeycombs [55].

Defect sensitivity of truss properties may also be affected by the predominant deformation mode: that is, whether the truss is stretch-dominated or bend-dominated. For example, the elastic moduli of 2-dimensional triangular trusses are minimally af-

fected by random removal of struts [57]. This is because the starting truss is stretch-dominated and, in the presence of a small number of defects, remains essentially stretch-dominated for all loading states. In contrast, the behavior of 2-dimensional hexagonal trusses depends on the nature of the macroscopic stress state. When loaded in shear, the truss is bend-dominated and therefore its shear modulus is extremely low; removing struts only reduces the shear modulus slightly [57]. But, when loaded hydrostatically, it deforms entirely by strut stretching. Here, removal of even a small number of struts triggers a transition from stretch- to bend-dominated deformation and a precipitous drop in the bulk modulus. For example, when 10% of struts are randomly removed from such a truss, the computed bulk modulus decreases by nearly three orders of magnitude [57].

Viewed from a different perspective, the extent to which defects affect truss properties may be influenced by the nature of the failure mechanism. For example, if the load-bearing capacity is dictated by *elastic strut buckling*, the presence of a small number of missing struts should not significantly affect truss strength. Although missing struts may cause strain elevations in neighboring struts and lead to premature buckling of the affected struts, eventually all remaining compressive struts also buckle, each supporting *nominally* the same load. In this case, the truss strength is reduced by an amount proportional to the fraction of missing struts [63]. In con-

trast, if failure occurs by *brittle fracture* of struts that experience tensile stresses, the strain elevations around a single missing strut may initiate fracture of neighboring struts, possibly leading to a cascade of further strut fractures and ultimately complete truss failure. Here, the load-bearing capacity of the truss would be determined by extreme values of tensile stresses within the struts and would follow weakest link scaling laws. Failure via *plastic strut yielding* is likely to exhibit an intermediate sensitivity to strut defects. That is, local strain elevations may trigger strut yielding in regions adjacent to strut defects which, in turn, may lead to *plastic* buckling before the remaining struts have yielded. Because of the strain softening inherent to plastic buckling, the process is likely not as benign as elastic buckling (where buckled struts sustain essentially a constant load); but it is likely to spread in a more progressive manner relative to that associated with strut fracture (where failed struts have no load-bearing capacity).

Free surfaces of trusses are, themselves, defects. Because of reduced nodal connectivity at surfaces, strut strains may be elevated relative to those in the bulk [19]. Finite element simulations for the $\{FCC\}$ (octet) truss have shown that struts oriented perpendicular to the loading direction and situated along the edges experience strains that are as much as 50% greater than those of equivalent struts in the bulk [32, 35]. These strain elevations have been confirmed by experimental measurements

of strut strains using digital image correlation [33]. These measurements also confirm that the strains in the affected tensile struts are almost entirely due to axial deformation; the contributions from bending are negligible, as predicted by the simulations. They further show that the strains in compressive struts situated at the truss corners experience significant bending, with bending strains comprising up to 50% of the peak principal strut strains.

The goal of the present study is to determine the effects of individual strut defects and free surfaces, both separately and together, on strains in neighboring struts and the effects of strain elevations on the strength of three elastic-brittle, stretch-dominated truss structures. The article is organized in the following way. The truss topologies and defect types are described in Section 5.2. Finite element (FE) models are described in Section 5.3. Results for strut strain distributions in the elastic (pre-buckling) domain are summarized in Section 5.4. The nonlinear responses of the trusses, wherein struts buckle and/or fail in tension, are presented in Section 5.5. The implications for truss design and topology selection are noted in Section 5.6.

5.2 Truss topologies and defect types

The three truss structures of present interest are: (i) the octet truss, denoted $\{nFCC\}^3$, (ii) the binary truss 60% $\{nBCC\}^3 \,|\, 40\%$ $\{nSC\}^3$; and (iii) the binary truss 80% $\{nFCC\}^3 \,|\, 20\%$ $\{nSC\}^3$. Examples of the three trusses, each with $n = 2$, are shown in Figure 5.1. The two binary trusses are elastically isotropic and exhibit the maximal possible stiffness for strut-based trusses. (See Chapter 3 for a detailed analysis.) Their elastic properties are $E/E_o\rho = 1/6$, $G/E_o\rho = 1/15$ and $\nu = 1/4$, where ρ is relative density, E is Young's modulus, G is shear modulus, ν is Poisson's ratio, and E_o is the Young's modulus of the parent material [22, 32]. In contrast, the $\{nFCC\}^3$ truss is elastically anisotropic, with Young's moduli varying from a low of $E/E_o\rho = 1/9$ in [100]-type directions to a high of $E/E_o\rho = 1/5$ in [111]-type directions [12].

Strut types are denoted according to the system laid out in Section 3.2.2. In $\{FCC\}$ trusses, type I struts are aligned with [110] and [1$\bar{1}$0] directions, type II are aligned with [101] and [10$\bar{1}$] directions, and type III are aligned with [011] and [01$\bar{1}$] directions. Under compressive loading along the [100] direction, both type I and type II struts are oriented at 45 degrees to the compression direction and experience equivalent compressive strains. (The distinction between type I and type II struts is

only necessary when considering shear loading, wherein the two strut types are loaded in opposite directions: one in compression and the other in tension. For compressive loading, both are treated as type I struts.) Type III struts are perpendicular to the compression direction and experience axial tension. In $\{SC\}$ trusses, type IV struts are aligned with the [100] (loading) direction while type V struts are aligned with the [010] and [001] directions: the latter being loaded in tension when the truss is loaded in compression along the [100] direction. In $\{BCC\}$ trusses, type VI struts are aligned with [111] and [$\bar{1}$11] directions while type VII are aligned with [1$\bar{1}$1] and [11$\bar{1}$] directions. (Here again the distinction between the two strut types is only necessary for shear loading. In compression the two are identical and are treated here as type VI struts.) Table 3.2 shows struts of each type and their axial strains in an infinite truss ($n = \infty$) [32].

Defect types are similarly denoted by the type of missing strut (I, III, IV, V and VI). Defects are further distinguished by their locations: *bulk* defects being in the truss interior (far from the free surfaces), *surface* defects on one of the external faces parallel to the loading direction, *edge* defects at the intersections of two external faces, and *corner* defects at one of the 8 truss corners. In the subsequent analyses, surface defects are placed at the center of one of the external faces and edge defects are placed along the mid-point of an edge. Locations of surface, corner and edge

137

defects are shown in Figure 5.2.

5.3   Finite element methods

Finite element models were developed in a manner analogous to that of Section 3.2. Trusses were discretized using Timoshenko beam elements with circular cross-section. All struts of each elementary truss were assigned equal cross-sectional area, determined by the volume fractions of the constituent trusses. Simulations were performed for trusses with relative densities $\rho = 0.01$ or 0.05, although the normalizations introduced below allow the results to be generalized for other values of relative density. Defects were introduced by removing individual struts of the designated type. Compressive loads were applied along the [100] direction, hereafter denoted as the 1-axis. Models were processed using the commercial package Abaqus (Version 6.13-EF4, Dassault Systèmes, Providence, Rhode Island).

Both linear and non-linear simulations were performed. For the linear simulations, nodal displacements were prescribed on opposing faces of the model in a manner identical to that described in Section 3.2.2: $u = \epsilon_1 L$ at $x = L$ and $u = 0$ at $x = 0$, where u is nodal displacement along the 1-axis, x is the position on the 1-axis, ϵ_1 is the strain in the 1-direction and L is the length of the truss along the principal

directions. This yields uniaxial compressive loading along the [100] direction.

For the nonlinear simulations (incorporating effects of elastic strut buckling), nodal *velocities* (instead of displacements) were prescribed on one face using the boundary conditions detailed in Section 3.2.4: $\dot{u} = \dot{\epsilon}L$ at $x = L$ where the dots represent derivatives with respect to time. The opposing face was fixed ($u = 0$ at $x = 0$). Rigid body motion was prevented by pinning the node at the origin, *i.e.* $u = v = w = 0$ at $(0,0,0)$ where v and w are nodal displacements in the 2- and 3-directions, respectively, and by assigning $w = 0$ to the node at $(0, L, 0)$. Velocities were selected to yield quasi-static strain rates ($|\dot{\epsilon}| = 10^{-3}s^{-1}$). To reduce computation time, the mass density in the nonlinear simulations was artificially increased by a factor of 10. To minimize oscillations following tensile failure, damping was introduced according to Equation 3.3. Here, $\xi = 0.48$. To confirm that the loading was quasi-static (prior to strut failure), the ratio of kinetic energy to potential energy was computed at each time step and found to be less than 10^{-2}.

Two truss sizes were studied. The first, with $n = 11$, was used to assess the effects of *bulk* defects in essentially infinite trusses. Here strut defects were placed at the truss center. Using linear simulations, the principal strains in all struts in both the pristine and the defect-containing trusses were calculated from the strain components derived from axial, bending and torsional deformation modes on the strut surfaces.

We find, however, that maximum principal strains in the linear elastic domain are dominated by axial strains; bending and torsional modes contribute minimally. The size of the affected region around the bulk defects was characterized by the distance from the centroid of the defect to the centroid of the farthest strut in which the principal strains differ by at least 5% relative to that in the same strut within a pristine truss.

A second set of linear simulations was performed for $n = 5$. In this case, defects were placed on either bulk, surface, edge or corner sites. Here again the principal strains were computed for all struts in both pristine and defect-containing trusses. The objective of these simulations was to ascertain, both separately and together, the effects of free surfaces and strut defects on local strut strains. Because of reduced nodal connectivity of struts at free surfaces, such struts also experience strain elevations. In this context, surfaces themselves serve as defects, competing with missing struts to determine which ultimately dictates strength.

Results for peak values of maximum and minimum principal strains, ϵ_{max} and ϵ_{min}, respectively, are couched in two normalized forms. For tensile struts they are $k_{max} \equiv \epsilon_{max}/\epsilon^o_{max}$ and $\epsilon_{max}/\epsilon_1 = k_{max}\epsilon^o_{max}/\epsilon_1$ where ϵ^o_{max} is the maximum strain that would be obtained in an equivalent strut in the absence of a defect, ϵ_1 is the macroscopic axial strain, and k_{max} is the strain concentration factor; for the com-

pressive struts they are $k_{min} \equiv \epsilon_{min}/\epsilon_{min}^o$ and $\epsilon_{min}/\epsilon_1 = k_{min}\epsilon_{min}^o/\epsilon_1$ where ϵ_{min}^o is the largest minimum principal strain that would be obtained in an equivalent strut in the absence of a defect and k_{min} is the corresponding strain concentration factor. Although the former of each pair (the strain concentration factors) represent the relative effects of defects on the neighboring fields, the latter of each pair, when compared to values for other struts in the same truss, provide a more informative indicator of which defects are likely to dominate failure.

To determine the separate effects of free surfaces and strut defects, strut strains are also couched in terms of minimum and maximum principal strains due to free surfaces, ϵ_{min}^{edge} and ϵ_{max}^{edge}, and those due to a single strut defect, ϵ_{min}^{defect} and ϵ_{max}^{defect}. When $\epsilon_{max}^{defect}/\epsilon_{max}^{edge} < 1$, bulk strut defects are not expected to be strength-limiting.

All nonlinear simulations were performed for $n = 5$ (larger truss sizes being somewhat prohibitive in terms of computation time). Although the size of the truss is smaller than that of the linear simulations, strain amplification due to free surface effects are nearly equivalent to those of the larger truss [32]. The goal of these simulations was to to determine the effects of defects on both buckling of struts in compression and fracture of struts in tension. Tensile fracture was assumed to occur when the maximum principal strain in the tensile struts exceeds a critical value at any point in an element. The broken element was then removed from the model.

To accurately determine the sequence of strut fractures, the nonlinear simulations were performed in two steps. In the first, the state of the system was recorded at 100 equally-spaced time increments, up to a macroscopic strain of 1%. From this data, the increment of time (usually within a single time step) over which most failures occurred was identified. The simulations were then repeated, in this case with the state of the system being saved in 1000 equally-spaced time increments within the interval in which the failure events occurred.

In order to probe transitions from buckling-dominated to fracture-dominated domains, the tensile failure strains selected for this study were based on the expected strains required for strut buckling, using the $\{FCC\}$ truss as a baseline, in the following way. In the $\{FCC\}$ truss, type I struts buckle at an axial strut strain $\epsilon_a = \rho/6$, essentially independent of truss size [32]. Within the bulk of a large truss, the axial tensile strains in type III struts are of equal magnitude ($\epsilon_a = \rho/6$). At free surfaces, however, the reduced nodal connectivity leads to a 50% elevation in strut strain, yielding $\epsilon_a = \rho/4$ [33]. Neglecting bending strains, the expectation therefore is that, when the tensile failure strain is $\epsilon_f = \rho/4$, buckling of type I struts and tensile failure of near-surface type III struts should occur simultaneously. Accordingly, most simulations were performed using one of four tensile failure strains: two below and two above the expected critical value, notably $\epsilon_f/\rho = 0.048, 0.24, 0.48$ or 0.96. The

same values of fracture strains were employed for all truss types. To capture the transition from fracture- to buckling-dominated failure in each truss, additional FE simulations were performed with ϵ_f/ρ ranging from 0.097 to 1.34. For comparison, simulations were also performed without a prescribed failure strain, *i.e.* for a purely linear-elastic material.

The results are couched in terms of stress normalized by $E_o\rho^2$ and strain normalized by ρ [32]. These normalizations yield the expected scalings in properties, notably stiffness proportional to $E_o\rho$ and buckling strength proportional to $E_o\rho^2$. Provided ρ is sufficiently small and failure is buckling-dominated (that is, neither yielding nor fracture intervene), the results in this form are, to a very good approximation, independent of ρ and E_o.

5.4 Elastic strain concentrations

5.4.1 Role of free surfaces

The maximum tensile strains in the $\{FCC\}$ truss (absent defects) are obtained in type III struts located along the truss edges (arrows in Fig. 5.3(a)). Here the peak strains and strain concentrations are $\epsilon_{max}/\epsilon_1 = -0.51$ and $k_{max} = 1.53$ (Table 5.2).

But the effects are highly localized; neighboring struts experience only slight strain elevations while those more than 2 strut lengths from the defect location are almost unaffected.

The maximum tensile strains in the $\{FCC\}|\{SC\}$ truss also occur in type III struts located near the truss edges, but offset by a distance of one strut length from the edge itself (arrows in Fig. 5.3(b)). Here the peak strains are considerably smaller: $\epsilon_{max}/\epsilon_1 = -0.36$ (Table 5.2). Strain elevations are also obtained in the type V struts within the $\{SC\}$ sub-truss located along the free surfaces, although their magnitudes are even smaller ($\epsilon_{max}/\epsilon_1 = -0.28$). In the $\{BCC\}|\{SC\}$ truss, the peak tensile strains are obtained in type V struts located at the free surface and oriented perpendicular to those surfaces ($\epsilon_{max}/\epsilon_1 = -0.29$, Fig. 5.3(c), Table 5.2).

5.4.2 Bulk defects in infinite trusses

As we show presently, elevations in the minimum principal strains around strut defects do not affect the buckling response and thus the following discussion focuses on tensile struts alone. (Notwithstanding, the minimum principal strains may be relevant to scenarios in which failure involves strut yielding and are therefore included for completion, in Table 5.1 and Table 5.2.)

Bulk defects are most benign in the $\{FCC\}$ truss (Table 5.1, Table 5.2). The maximum tensile strains in type III struts increase by 25% and 12% around type I and type III defects, respectively. The strain elevations persist over distances of 2 strut lengths (or 1.4 unit cell lengths). Most importantly, the strain elevations are smaller than those in struts located at the free surfaces. The inference is that, when truss failure is fracture dominated, bulk defects should play almost no role in truss strength.

In the binary trusses, only type IV defects (within the $\{SC\}$ truss) result in peak tensile strains that exceed those due to free surfaces. In the $\{FCC\}|\{SC\}$ truss, peak tensile strains (in type III struts) increase by 50% around a type IV defect, exceeding the maximum tensile strain at the edges by 5%. In the $\{BCC\}|\{SC\}$ truss, the peak tensile strains due to a type IV defect exceed those due to the free surfaces by about 15%.

5.4.3 Defects in finite trusses

The effects of defects in finite trusses depend on defect location (Figure 5.4). In the $\{5FCC\}^3$ truss, the effects of a center defect are identical to those at the center of the larger ($\{11FCC\}^3$) truss (Table 5.1, Table 5.3): both yielding peak strains lower than those at the free surfaces. Defects at corners, edges and surfaces are

145

similarly benign.

In the $\{BCC\}|\{SC\}$ truss, type IV defects have the greatest effect, with the strains in surrounding struts being greater than that due to the surfaces for all defect locations (Figure 5.5). Among the possible locations, the edge site is most deleterious; the local strut strain there is about 19% greater than that at the free surfaces in the absence of defects. In the $\{FCC\}|\{SC\}$ truss, type I and type IV defects also yield local strains exceeding those of the free surfaces. The most extreme case is that of a type IV edge defect; the local strains there are 59% greater than those due to the free surfaces alone.

5.5 Inelastic response of finite trusses

Coupled effects of defect type, defect location and tensile failure strain on the compressive stress-strain response of the three trusses are shown in Figure 5.6. Two combinations of defect type and defect location were considered for each truss type. The selected combinations produce the greatest tensile strain elevations (Table 5.3). The variation in truss strength with failure strain (absent strut defects) is plotted on Figure 5.7.

146

5.5.1 $\{FCC\}$ truss

The intrinsic response of the $\{FCC\}$ truss is essentially elastic-"perfectly plastic". That is, buckling occurs in all compressive struts over a narrow strain range; thereafter, the stress needed for continued buckling remains constant. When the material failure strain is taken as $\epsilon_f/\rho = 0.24$, strut failure initiates essentially *at* the point of incipient buckling, where the stress-strain curve just begins to display slight non-linearity. Once buckling initiates, bending of the most critically-loaded struts leads to strut fracture. Failure initiates in tensile struts near the corners and then proceeds diagonally along a (111)-type plane (Vid. S4). Corner defects do not alter the failure response, except that the failure initiation site is shifted slightly towards the defect (Vid. S5–S6).

Doubling the material failure strain (to $\epsilon_f/\rho = 0.48$) increases the truss failure strain by only a small amount. This is because, once large-scale buckling occurs, bending strains in the tensile members increase rapidly, bringing those struts to criticality with only small amounts of additional applied strain (Fig. 5.8). Here again the failure sequence initiates at the corner and proceeds along type III struts within (111)-type planes (Vid. S7). Somewhat larger (though not proportionate) gains in truss failure strain are made when the material failure strain is doubled again (to $\epsilon_f/\rho = 0.96$). In this case, failure occurs well within the plateau associated

with large-scale buckling.

In contrast, when the material failure strain is reduced five-fold from the baseline value (that is, from $\epsilon_f/\rho = 0.24$ to $\epsilon_f/\rho = 0.048$), both the failure strain and the failure stress of the truss decrease proportionately. In this domain, failure occurs while the tensile struts experience only axial strains (with minimal bending); since these strains are proportional to the applied strain, it follows that truss strength varies linearly with the material failure strain. Since truss fracture occurs almost immediately after the first strut failure, the ultimate strength is expected to follow in accordance with

$$\sigma_f/E_o\rho^2 = (E/E_o\rho)(\epsilon_1/\epsilon_a k_{max})(\epsilon_f/\rho) \tag{5.1}$$

where, for the $\{FCC\}$ truss, $E/E_o\rho = 1/9$, $\epsilon_a/\epsilon_1 = 1/3$ and $k_{max} = 1.5$. This prediction, superimposed on Figure 5.7, agrees very well with the computed strengths.

The preceding behavioral transition (at a critical material failure strain) is also manifested as the relative density is varied. The latter transition is shown in a plot of strength vs. relative density (Figure 5.9). At low values of ρ, the strength is buckling-dominated and proportional to ρ^2. In contrast, at high values of ρ, the strength is fracture-dominated and proportional to ρ. The transition occurs at a critical value of ρ that depends on material failure strain. From Eqn. 5.1 and the computed buckling strength ($\sigma_f/E_o\rho^2 = 0.056$), the transition is expected at $\epsilon_f/\rho = 0.25$.

148

Strut defects, even when located in the most deleterious locations, have remarkably small effects on strength of the $\{FCC\}$ truss (typically $\leq 5\%$). This is because strain concentrations associated with the surfaces are generally greater than those around strut defects.

5.5.2 Binary trusses

The behaviors of the two binary trusses differ from that of the $\{FCC\}$ truss in three ways. First, the intrinsic responses of the binaries involve two sets of buckling events: one each for the $\{SC\}$ and either the $\{FCC\}$ or $\{BCC\}$ constituent trusses. The limit stress for the $\{FCC\}|\{SC\}$ truss is about 20% lower than that of the $\{FCC\}$ truss. This reflects the volume fraction of material allocated to the $\{SC\}$ truss, the latter bearing minimal load after buckling. Additionally, the material failure strain needed to reach the limit stress is considerably higher than that in the $\{FCC\}$ truss. This is because buckling of the first set of struts (within the $\{SC\}$ truss) induces bending in the tensile struts and therefore accelerates failure. The limit stress for the $\{BCC\}|\{SC\}$ truss is marginally greater than that of the $\{FCC\}$ truss. But here again buckling of the $\{SC\}$ truss (at about 70% of the limit stress) induces bending in the tensile struts. Attaining the full strength potential therefore requires materials with higher failure strains (by a factor of about 5 relative

149

to that needed for the $\{FCC\}$ truss).

Second, in the domain in which the material failure strain is small, the strength is again proportional to the material failure strain, in accordance with Eqn. 5.1; here $E/E_o\rho = 1/6$ for both binary trusses, and $\epsilon_a/\epsilon_1 = -0.35$ and -0.32 for the $\{FCC\}|\{SC\}$ and the $\{BCC\}|\{SC\}$ trusses, respectively. Here the $\{BCC\}|\{SC\}$ truss emerges as the best choice; the combination of high stiffness and low strains in the constituent tensile struts render it the strongest (more than twice that of the $\{FCC\}$ truss).

Third, the strengths of the binary trusses exhibit a stronger defect sensitivity when the material failure strain is low. In this domain, a type IV corner defect reduces the compressive strength of the $\{FCC\}|\{SC\}$ truss by 25%. Fracture initiates at the flaw location. In contrast, in the pristine truss, failure initiates in the type III struts at the truss corners and edges, indicated in Figure 5.3. In the $\{BCC\}|\{SC\}$ truss, type IV edge and corner defects reduce compressive strength by roughly 13 and 16%, respectively. The reductions in strength agree with strain amplifications due to these defects (Table 5.3). In both defective trusses, tensile failure initiates near the defects. [Details of failure sequences are provided in Supplementary Material (Vid. S8-S12).]

5.5.3 Stochastic failure

Although the present study has focused on cases in which the material failure strain and hence strength are deterministic material properties, some insights into defect sensitivity when failure is stochastic can also be gleaned. Assuming that truss failure occurs when the first tensile strut breaks — an assumption consistent with the FE simulations — the truss strength distribution can be written in terms of the *strut strength* distribution coupled with *strut stress* distribution. Here the survival probability of the truss is simply the product of survival probabilities of all individual struts. If the strength of the struts follows a Weibull distribution with reference strength σ_o for a reference volume equal to strut volume and with a Weibull modulus (or dispersion index) m, the survival probability P_s can be expressed as [67]

$$lnP_s = -\sum_{i=1}^{N}(k_i\sigma_n/\sigma_o)^m \tag{5.2}$$

where σ_n is the nominal tensile strut stress in an infinite truss, k_i is the stress (or strain) concentration on strut i, and N is the total number of tensile struts. It follows that the ratio of the median strength (corresponding to $P_s = 1/2$) of a finite truss in which surface effects are operative to that of a notional truss of the same size but *without* surface effects is $\langle k_i^m \rangle^{-1/m}$ where $\langle\ \rangle$ denotes a mean value.

Distributions of k_i (shown in Figure 5.10) range from 0.6 to 1.5 in the $\{FCC\}$

truss and 0.6 to 1.25 in the $\{BCC\}|\{SC\}$ truss. The computed ratios of median strengths (in Figure 5.11) show that: (i) as $m \to \infty$, the ratio of median strengths approaches $1/k_{max}$, and (ii) for Weibull moduli typical of structural ceramics ($m = 5 - 10$), the ratios of median strengths are close to unity. (For example, for $m = 5$, the ratios are 0.98 and 0.97 for the $\{FCC\}$ and $\{BCC\}|\{SC\}$ trusses, respectively.) The inference is that the small number of affected struts in a large truss made from a brittle material with even a modestly wide strength dispersion should have little effect on average strength.

5.6 Conclusions

The key conclusions from this study follow.

1. Among the three trusses studied here, $\{FCC\}$ is the most defect-tolerant. This is because the strain elevations around bulk strut defects (distant from the free surfaces) are smaller than those at free surfaces. Even when defects are located at a free surface and the strain elevations from the defects are conflated with those due to the surface itself, their effects on local strut strains and compressive truss strength are remarkably small ($\leq 5\%$).

2. Somewhat greater strength reductions are obtained in the binary trusses when

152

defects are situated at the corners (by about 20-25%), a result of the higher strain elevations around these defects.

3. The full strength potential of the $\{FCC\}$ truss, dictated by large-scale strut buckling, is only attained when the material failure strain exceeds a critical value of $\epsilon_f/\rho \approx 0.25$. This condition is conceivably attainable with hard thermoplastics; a failure strain of $\epsilon_f = 0.05$ would satisfy this condition for relative densities up to $\rho = 0.2$. In contrast, if the truss were made of a high-strength ceramic, where the failure strain (optimistically) may be $\epsilon_f = 0.01$, the condition would only be satisfied for relative densities up to $\rho = 0.04$.

4. When the condition for large-scale buckling is satisfied and the maximum possible strength is attained, the $\{FCC\}$ truss is preferred over the two binary trusses, since it attains its peak strength at the lowest level of material failure strain. Although in principle the binary $\{BCC\}|\{SC\}$ truss can achieve a slightly higher strength, this requires materials with much higher failure strains (by almost an order of magnitude). Because of the additional constraints on material properties and the greater geometrical complexity of this truss topology, the marginal strength gains would not likely warrant selection of this truss topology, unless the design necessarily required elastic isotropy in combination with high strength.

5. In cases in which the material failure strain falls well below that required to attain large-scale strut buckling, say $\epsilon_f/\rho < 0.1$, as it might in low relative density ceramic trusses, the $\{BCC\}|\{SC\}$ truss would be preferred, since it exhibits the highest strength, more than twice that of the $\{FCC\}$ truss. This is a consequence of the higher truss stiffness and the lower tensile strains generated in the $\{BCC\}|\{SC\}$ truss.

Table 5.1: Struts with at least a 5% change in principal strain due to the presence of a defect (shown in black). Colors of intact struts represent minimum or maximum principal strut strains.

	Defect type				
	I	III	IV	V	VI
{FCC}					
{FCC}|{SC}					
{BCC}|{SC}					

ϵ_p/ϵ_1
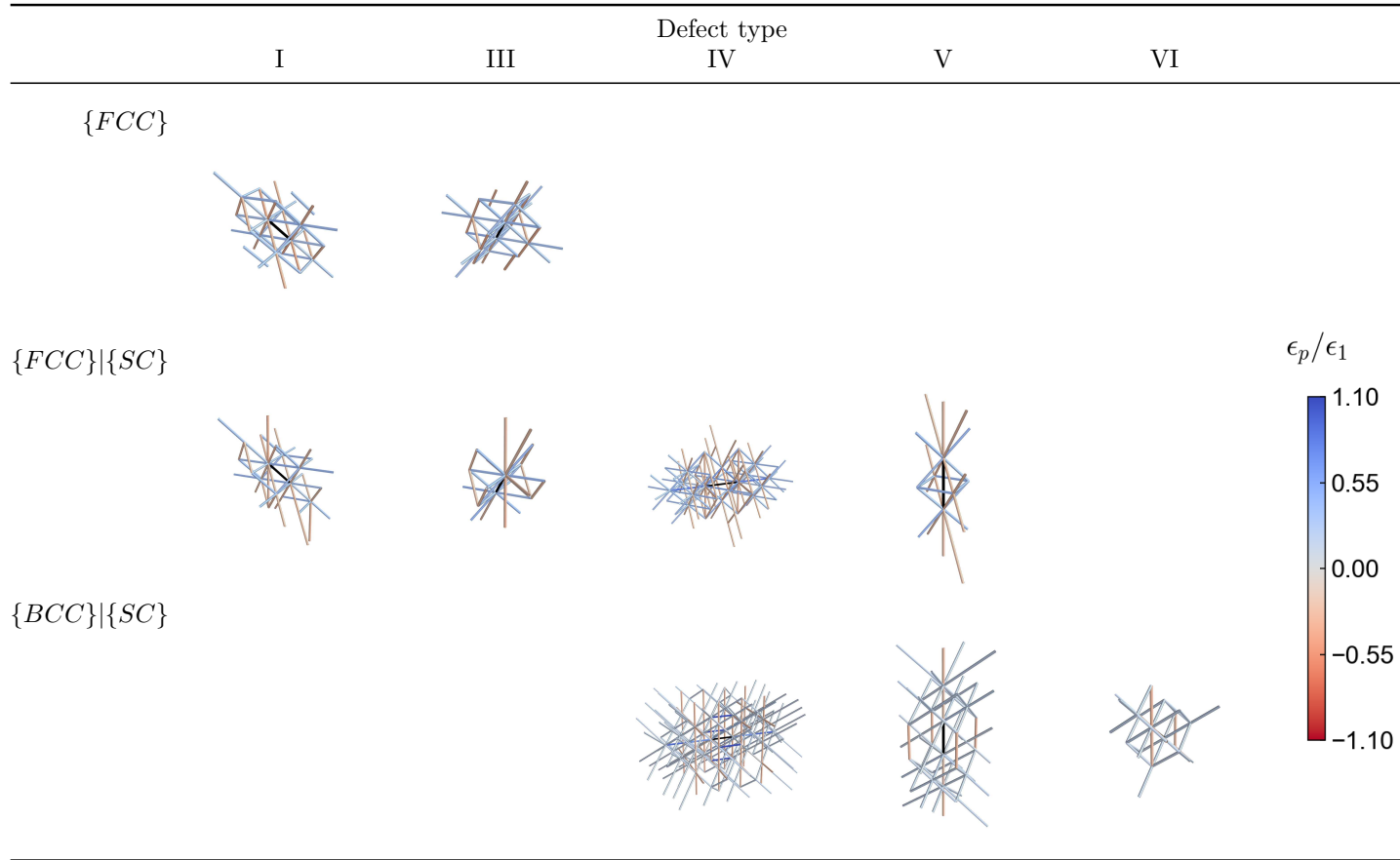
Table 5.2: Effects of bulk defects on principal strut strains.

		Strut Type								
		I, II		III		IV		V		VI, VII	
Truss	Defect type	$\frac{\epsilon_{min}}{\epsilon_1}$	$\frac{\epsilon_{min}^{defect}}{\epsilon_{min}^{edge}}$	$\frac{\epsilon_{max}}{\epsilon_1}$	$\frac{\epsilon_{max}^{defect}}{\epsilon_{max}^{edge}}$	$\frac{\epsilon_{min}}{\epsilon_1}$	$\frac{\epsilon_{min}^{defect}}{\epsilon_{min}^{edge}}$	$\frac{\epsilon_{max}}{\epsilon_1}$	$\frac{\epsilon_{max}^{defect}}{\epsilon_{max}^{edge}}$	$\frac{\epsilon_{min}}{\epsilon_1}$	$\frac{\epsilon_{min}^{defect}}{\epsilon_{min}^{edge}}$
{FCC}	—	0.509		-0.505							
	I, II	0.468	0.919	-0.416	0.825						
	III	0.466	0.917	-0.372	0.737						
{FCC}|{SC}	—	0.559		-0.356		1.061		-0.274			
	I, II	0.501	0.896	-0.332	0.933	1.067	1.006	-0.303	1.108		
	III	0.475	0.849	-0.276	0.775	1.022	0.963	-0.296	1.083		
	IV	0.656	1.173	-0.375	1.053	1.027	0.968	-0.288	1.053		
	V	0.475	0.850	-0.316	0.887	1.022	0.963	-0.264	0.963		
{BCC}|{SC}	—					1.052		-0.293		0.358	
	IV					1.077	1.024	-0.335	1.145	0.446	1.246
	V					1.035	0.984	-0.279	0.951	0.278	0.776
	VI, VII					1.039	0.988	-0.291	0.995	0.258	0.722

Shaded numbers are those most relevant to discussion in the text.

156

Table 5.3: Effects of defects on tensile strut strains in finite trusses.

Truss	$\epsilon_{max}^{edge}/\epsilon_1$	Defect type	Defect location	$\epsilon_{max}^{defect}/\epsilon_1$	$\epsilon_{max}^{defect}/\epsilon_{max}^{edge}$
$\{5FCC\}^3$	-0.50	I	corner	-0.49	0.99
			edge	-0.47	0.94
			surface	-0.44	0.88
			center	-0.44	0.88
		III	corner	-0.49	0.99
			edge	-0.39	0.78
			surface	-0.38	0.75
			center	-0.39	0.78
$\{5FCC\}^3|\{5SC\}^3$	-0.35	I	corner	-0.43	1.25
			edge	-0.42	1.22
			surface	-0.42	1.19
			center	-0.35	0.99
		III	corner	-0.33	0.94
			edge	-0.28	0.79
			surface	-0.26	0.75
			center	-0.31	0.89
		IV	corner	-0.48	1.39
			edge	-0.55	1.59
			surface	-0.47	1.36
			center	-0.38	1.08
		V	corner	-0.35	1.00
			edge	-0.33	0.94
			surface	-0.27	0.78
			center	-0.32	0.92
$\{5BCC\}^3|\{5SC\}^3$	-0.32	IV	corner	-0.36	1.13
			edge	-0.38	1.19
			surface	-0.35	1.12
			center	-0.35	1.11
		V	corner	-0.28	0.90
			edge	-0.29	0.92
			surface	-0.29	0.90
			center	-0.29	0.92
		VI	corner	-0.28	0.90
			edge	-0.29	0.92
			surface	-0.31	0.98
			center	-0.32	1.01

Shaded numbers are those most relevant to discussion in the text.
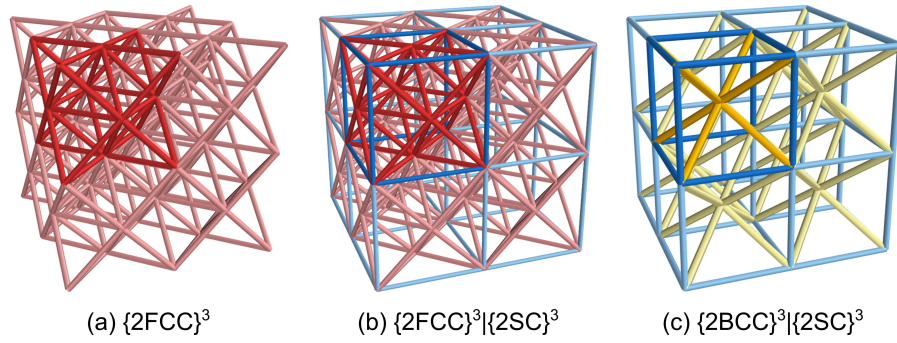
(a) {2FCC}³   (b) {2FCC}³|{2SC}³   (c) {2BCC}³|{2SC}³

Figure 5.1: Cubic truss structures at a relative density $\rho = 0.05$. Unit cells are indicated by darker colors.

(a) {5FCC}³

(b) {5SC}³   (c) {5BCC}³

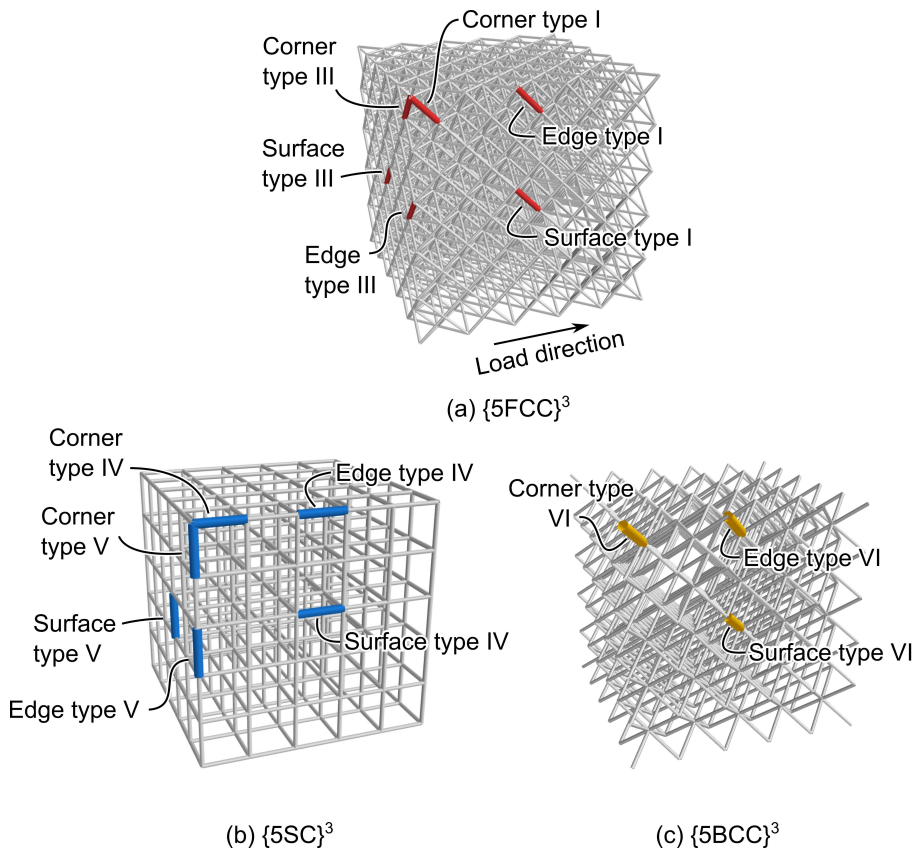**Figure 5.2:** Locations of surface, edge and corner defects in (a) $\{5FCC\}^3$, (b) $\{5SC\}^3$ and (c) $\{5BCC\}^3$ trusses.

x/a = 1   x/a = 5

k_{max}

1.5

1.0

0.5

(a) $\{11FCC\}^3$

(b) $\{11FCC\}^3|\{11SC\}^3$

(c) $\{11BCC\}^3|\{11SC\}^3$
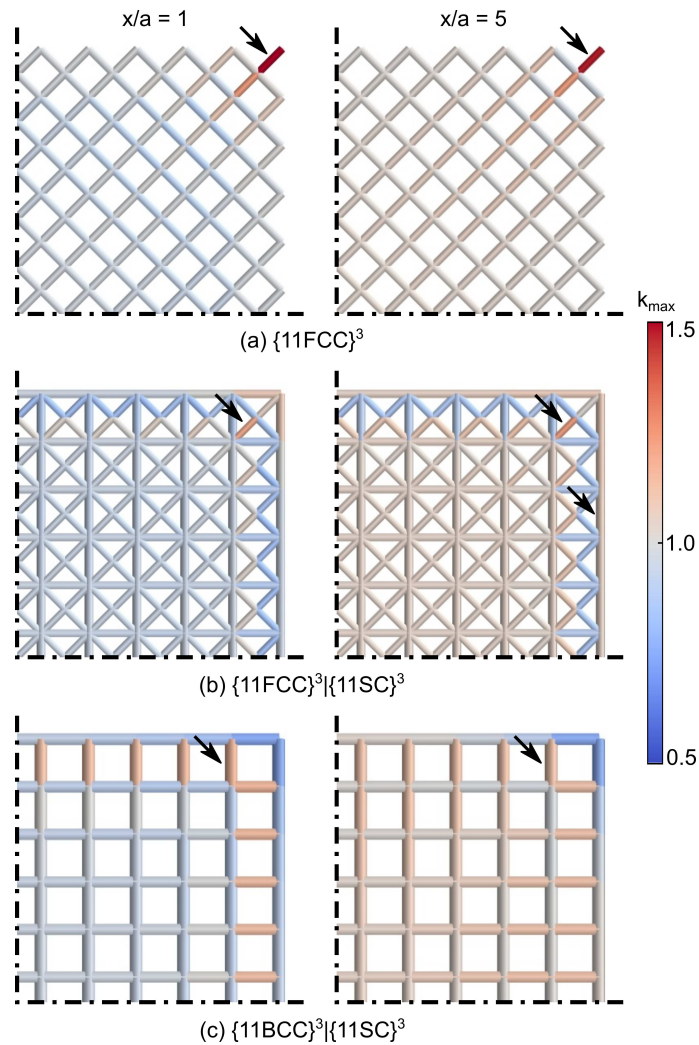
Figure 5.3: (a) The greatest strain concentrations in tensile struts within the $\{FCC\}$ truss are largely confined to the edge struts (shown here in cross-sections transverse to the loading directions, at two distances from one of the loaded faces: $x/a = 1$ and 5). (b, c) The greatest strain concentrations in the two binary trusses are similarly obtained at the truss edges, but their magnitudes are somewhat smaller. Arrows indicate struts with the maximum strain concentration factor within each plane. Due to the cubic symmetry of the trusses, only one quadrant of each cross-section is shown. Thick dashed lines indicate lines of symmetry. [Videos showing sections at distances that, in totality, comprise data for all tensile members in the truss can be found in Supplementary Information (Vid. S1-S3).]
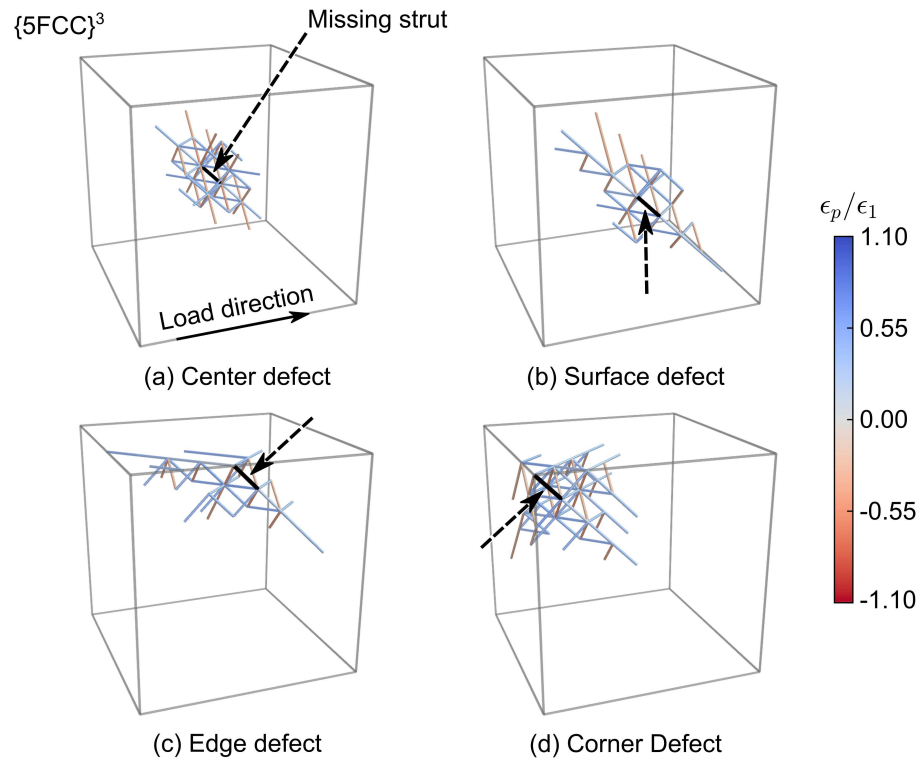
Figure 5.4: Strain elevations around type I strut defects in the $\{FCC\}$ truss depend on defect location, the maximum occurring when the defect is at a truss corner. The effects persist over distances of about two strut lengths. Only struts that experience a strain change $\geq 5\%$ are shown. Arrows indicate missing struts.
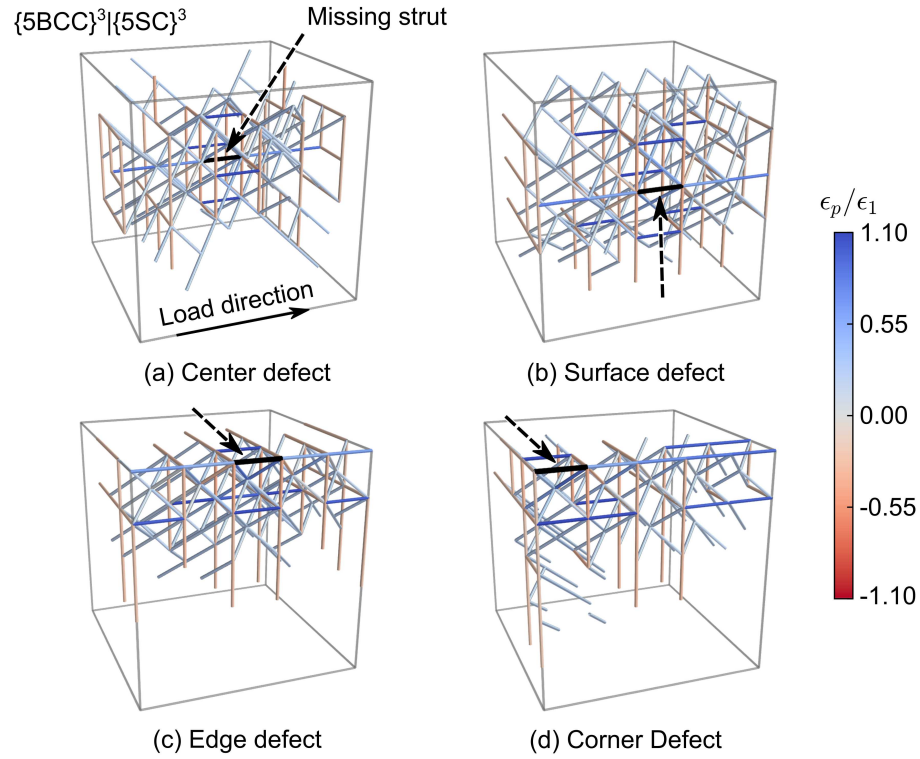
Figure 5.5: Strain elevations around type IV strut defects in the $\{5BCC\}^3|\{5SC\}^3$ truss depend on defect location. Although the strain concentrations are modest, they persist over lengths approaching (in this case) the entire truss. Only struts that experience a strain change $\geq 5\%$ are shown. Arrows indicate missing struts.
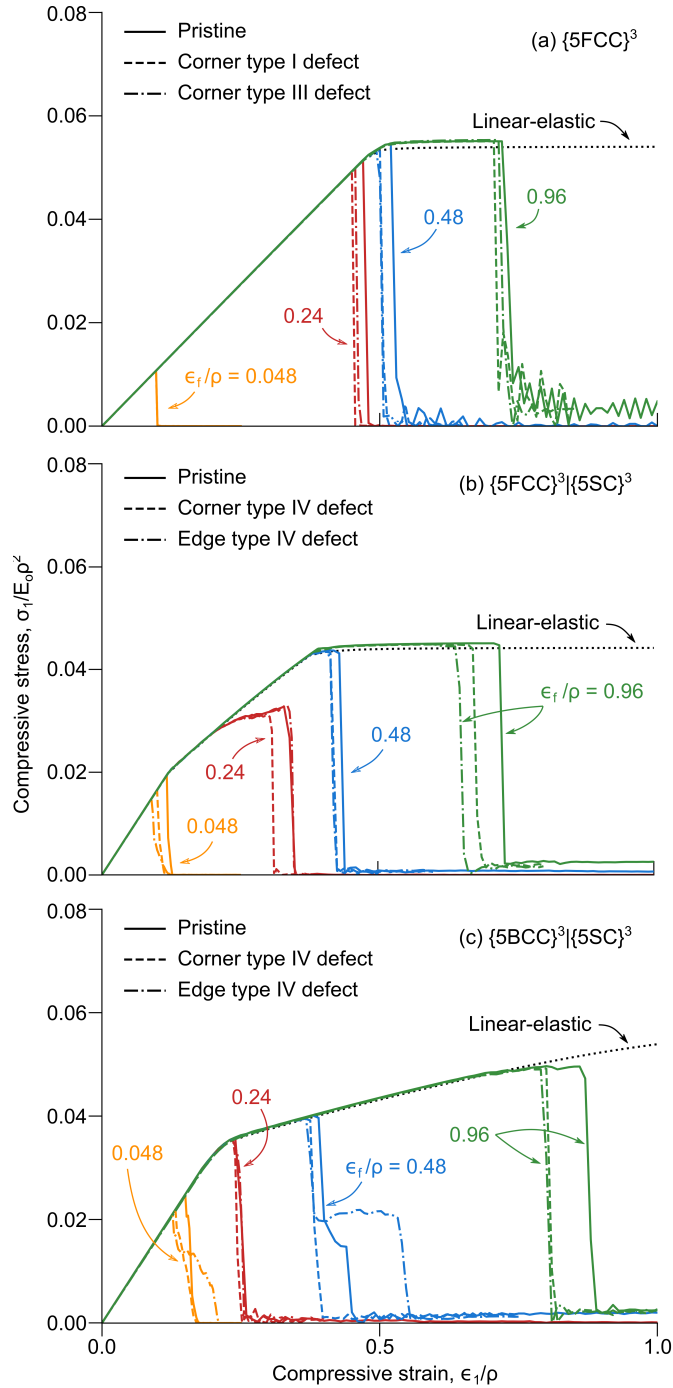
Figure 5.6: Stress-strain responses of the three trusses exhibit varying degrees of non-linearity, dependent on truss topology and material failure strain; the presence of strut defects and their locations within the truss play secondary roles. (a) The $\{5FCC\}^3$ truss undergoes a single buckling event at essentially a single stress, thereby producing effectively elastic-"perfectly plastic" response. (b, c) The two binary trusses undergo two buckling events, each associated with one of the two compressive strut populations.
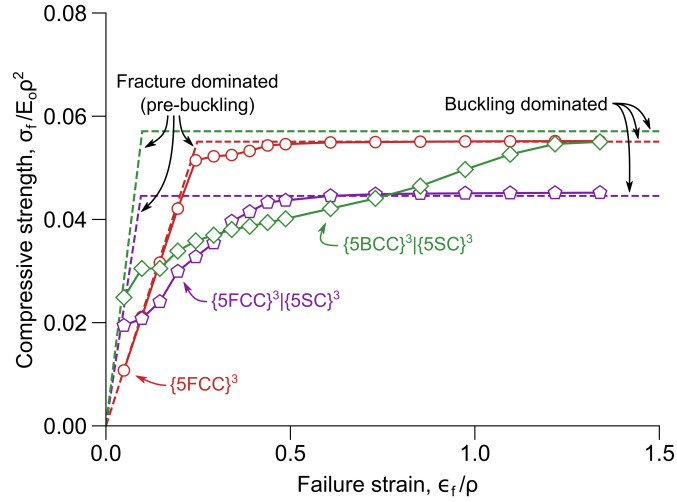
Figure 5.7: Compressive strengths of the three trusses transition from being fracture-dominated to buckling-dominated as the material failure strain increases. In the former domain, truss strength is linear with failure strain (indicated by inclined dashed lines, from Eqn. 5.1); in the latter, it is independent of failure strain (indicated by horizontal dashed lines). In the $\{FCC\}$ truss, the transition occurs over a relatively narrow range of failure strains ($\epsilon_f/\rho = 0.25$ to 0.5.). In contrast, the transitions in the two binary trusses are gradual, spanning a range of failure strains of about an order of magnitude (roughly, from $\epsilon_f/\rho = 0.1$ to 1). In the $\{BCC\}|\{SC\}$ truss in particular, the failure strain needed to attain the full strength is $\epsilon_f/\rho = 1.5$.
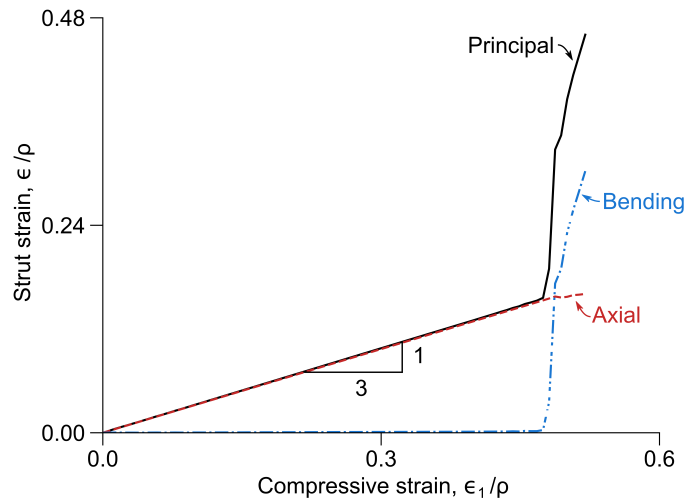
Figure 5.8: TThe principal strain in the first tensile strut to fail in the $\{FCC\}$ truss is initially due entirely to axial deformation. Once the neighboring compressive struts buckle, the axial strain in the tensile strut remains constant; further increases in the maximum principal strain are due to nodal rotations resulting from buckling and, in turn, to strut bending. The curves terminate once the strut strain reaches its failure strain which, in this case, is $\epsilon_f/\rho = 0.48$.
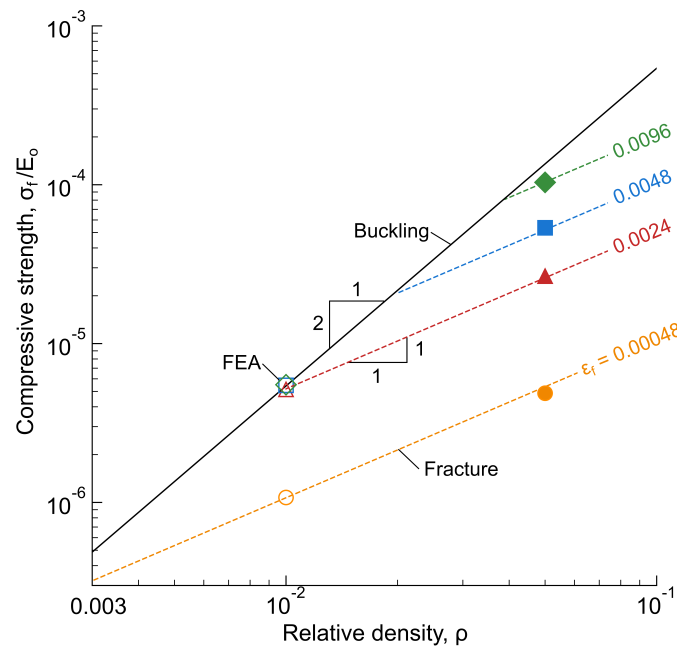
Figure 5.9: The compressive failure mode of the $\{FCC\}$ truss transitions from buckling of the compressive struts to fracture of the tensile struts at a critical point dictated by relative density and material failure strain. Accompanying the transition is a change in the sensitivity of strength to relative density, from quadratic to linear. (Dashed lines are analytical predictions, from Eqn 5.1; symbols are from FEA.)
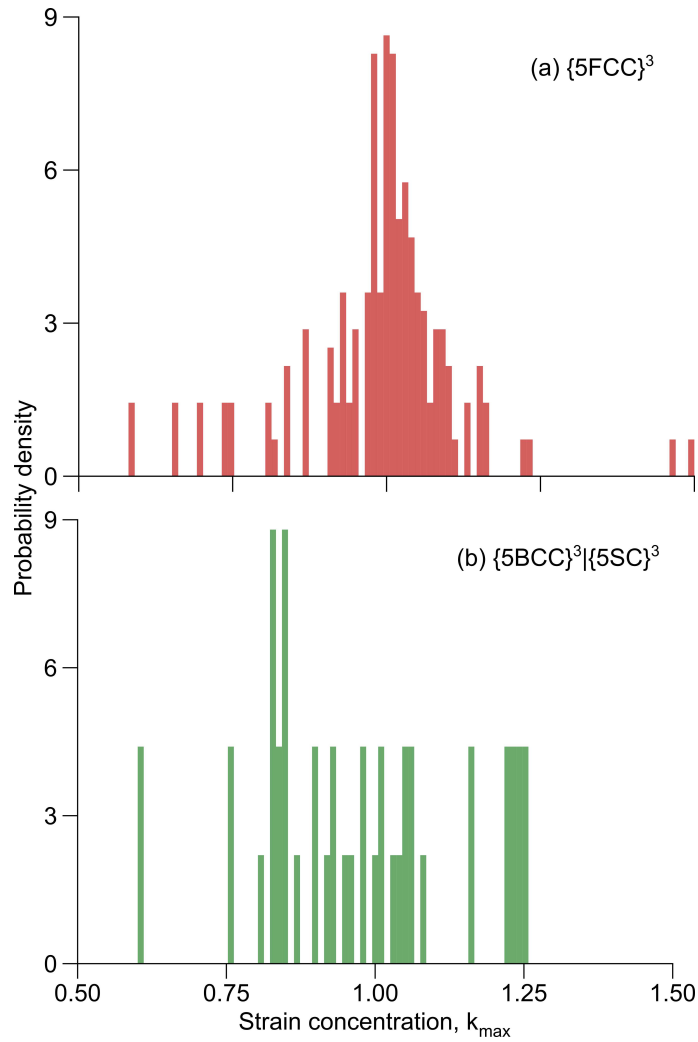
Figure 5.10: (a) The maximum principal strain concentrations in the $\{5FCC\}^3$ truss fall in the range of 0.6 to 1.5, although the number density of struts at the high end of this range is exceedingly small. (b) The $\{5BCC\}^3|\{5SC\}^3$ trusses exhibit a somewhat narrower range. Although the peak value is lower (about 1.25), the number density of struts with the highest strains is considerably greater than that in the $\{5FCC\}^3$ truss.
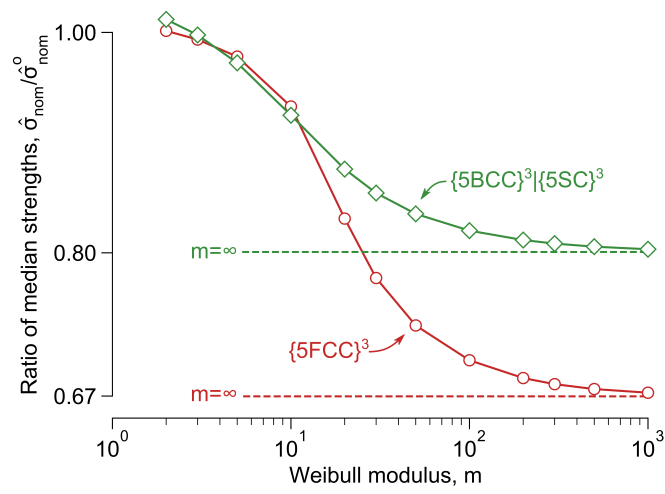
Figure 5.11: When strut strength is stochastic, small numbers of highly-strained tensile struts have little effect on median truss strength. For representative values of Weibull moduli of ceramics (say $m = 5 - 10$), the median strength would be reduced by less than 5%.

Chapter 6

Summary and future work

The design of lightweight trusses that are stiff, strong and defect-tolerant has been investigated using finite element models and experimental tests. The designs are based on a newly-developed system for classification of truss structure that borrows concepts from crystallography and geometry to describe nodal locations and their connectivity. Together, the classification system fully and unambiguously defines truss topology. Within this framework, isotropic trusses are formed by combining two or more elementary cubic trusses in appropriate proportions. This method of forming compound trusses has been used to identify two isotropic binary compound trusses and many isotropic ternary trusses, all with elastic properties equal to the theoretical upper bound for isotropic trusses [22]. While the objective here was to identify trusses with isotropic elastic properties, analogous methods could be used to meet other objectives, *e.g.* maximizing the ratio of bulk to shear moduli or

168

minimizing Poissons ratio.

In addition to achieving high stiffness, compound trusses can exhibit high strength. When tensile failure precedes large-scale buckling, the isotropic $\{BCC\}|\{SC\}$ truss exhibits a compressive strength about twice that of the $\{FCC\}$ truss, a consequence of the higher truss stiffness and the lower tensile strains generated in the compound truss. In another regime, where strength is controlled by strut buckling, the $\{BCC\}|\{SC\}$ truss exhibits a strength that exceeds that of the $\{FCC\}$ truss by only a small margin. Moreover, its strength is predicated on the material response remaining elastic after compressive members buckle.

The full strength potential of the trusses is achieved only when elastic buckling of all compressive members precedes tensile failure. For the $\{FCC\}$ truss, this condition is met when the material failure strain exceeds $\epsilon_f/\rho \approx 0.25$. Attaining the full strength of the isotropic $\{BCC\}|\{SC\}$ truss requires a material failure strain that is roughly 5 times higher ($\epsilon_f/\rho \approx 1.5$). This is because the $\{SC\}$ struts of the compound truss buckle early and the subsequent bending of the buckled struts leads to large material strains before the struts within the $\{BCC\}$ truss begin to buckle.

In pristine trusses, strut strains near the surfaces are elevated by as much as 50% compared to those of equivalent struts in the bulk. Strain elevations due to missing struts in the bulk are lower than or comparable to the elevations already

169

present at the surface and thus do not affect the mechanical performance of the truss. Missing struts in regions of low nodal connectivity (*i.e.* near surfaces, edges and corners) cause the highest strain amplifications. However, their effects on strength are negligible in or near the buckling-dominated domain.

The study of defect sensitivity has been restricted to trusses containing to individual missing struts. Future work is needed to determine the effects of multiple defects and other defect types, *e.g.* strut waviness and variations in strut radii, to determine how property degradation scales with defect type and defect density.

For fixed topology, the mechanical performance of trusses can be improved with the addition of fillets in the node regions. Their addition can increase the buckling strength (by about 20% for the geometries tested) with only a small amount of added mass. In the present study, only one fillet geometry was considered; there are likely more weight-efficient designs that could be explored through the use of 3D finite element simulations. Recent advances in AM technologies, especially improved print resolutions, would enabled the implementation of fillets with optimized geometries.

The present study has addressed the performance of only a very small fraction of the entire universe of truss topologies. Additional work is needed to evaluate the performance of more complex trusses. For example, non-cubic trusses could be of interest for applications where isotropy is not required. In those applications, non-

cubic topologies with anisotropic strength may be preferable over the cubic trusses studied here.

In light of the effects of free surfaces that have been identified here, opportunities may exist for hybrid 2D/3D trusses. For example, 2D surface trusses (acting essentially as face sheets) could be combined with 3D trusses to reduce high strains near the edges and improve overall performance. Recognizing that such designs would require re-distribution of material mass from the bulk to the surface, optimization algorithms could be used to identify optimal truss geometries.

Other advancements in AM allow printing in two or more materials. This could be used, for example, to fabricate $\{FCC\}$ trusses in which compressive members are made from a hard, stiff thermoplastic (to avoid buckling or yielding) while tensile members are made from a softer (elastomeric) material. This could lead to trusses with improved energy absorption capacity relative to those of single-material trusses.

Rather than tailoring the properties of stretching-dominated trusses for high energy absorption efficiency, an alternative approach might seek to improve the performance of bending-dominated trusses. The constant crushing stress of bending-dominated trusses leads to desirable energy absorption characteristics. One topology of interest in this regard is the diamond cubic truss ($\{FCC\lfloor 0\,0\,0 \rfloor \lfloor {}^1\!/_4\,{}^1\!/_4\,{}^1\!/_4 \rfloor\}$). This structure has the lowest nodal connectivity and hence lowest strut aspect ratio at

fixed relative density of all 3D periodic trusses. Designs based on this topology have been used to create trusses with unique mechanical properties, including pentamode materials. (In pentamode materials, 5 of the 6 elements of the diagonalized elasticity tensor are zero [36].) To optimize for strength and energy absorption, its deformation characteristics could be tuned by varying the strut cross-section along the strut length.

References

[1] A. Asadpoure and L. Valdevit. Topology optimization of lightweight periodic lattices under simultaneous compressive and shear stiffness constraints. *International Journal of Solids and Structures*, 60:1–16, 2015.

[2] J. Bauer, S. Hengsbach, I. Tesari, R. Schwaiger, and O. Kraft. High-strength cellular ceramic composites with 3d microarchitecture. *Proceedings of the National Academy of Sciences*, 111(7):2453–2458, 2014.

[3] T. Bückmann, N. Stenger, M. Kadic, J. Kaschke, A. Frölich, T. Kennerknecht, C. Eberl, M. Thiel, and M. Wegener. Tailored 3d mechanical metamaterials made by dip-in direct-laser-writing optical lithography. *Advanced Materials*, 24(20):2710–2714, 2012.

[4] T. Buhl, C. B. Pedersen, and O. Sigmund. Stiffness design of geometrically non-

linear structures using topology optimization. *Structural and Multidisciplinary Optimization*, 19(2):93–104, 2000.

[5] G. A. Buxton and N. Clarke. bending to stretching transition in disordered networks. *Physical review letters*, 98(23):238103, 2007.

[6] G. Campoli, M. Borleffs, S. A. Yavari, R. Wauthle, H. Weinans, and A. A. Zadpoor. Mechanical properties of open-cell metallic biomaterials manufactured using additive manufacturing. *Materials & Design*, 49:957–965, 2013.

[7] H. D. Carlton, J. Lind, M. C. Messner, N. A. Volkoff-Shoemaker, H. S. Barnard, N. R. Barton, and M. Kumar. Mapping local deformation behavior in single cell metal lattice structures. *Acta Materialia*, 129:239–250, 2017.

[8] V. Challis, A. Roberts, and A. Wilkins. Design of three dimensional isotropic microstructures for maximized stiffness and conductivity. *International Journal of Solids and Structures*, 45(14):4130–4146, 2008.

[9] X. Cheng, S. Li, L. Murr, Z. Zhang, Y. Hao, R. Yang, F. Medina, and R. Wicker. Compression deformation behavior of ti–6al–4v alloy with cellular structures fabricated by electron beam melting. *j=Journal of the mechanical behavior of biomedical materials*, 16:153–162, 2012.

[10] S. Chiras, D. Mumm, A. Evans, N. Wicks, J. Hutchinson, K. Dharmasena, H. Wadley, and S. Fichter. The structural performance of near-optimized truss core panels. *International Journal of Solids and Structures*, 39(15):4093–4115, 2002.

[11] V. Deshpande, M. Ashby, and N. Fleck. Foam topology: bending versus stretching dominated architectures. *Acta materialia*, 49(6):1035–1040, 2001.

[12] V. S. Deshpande, N. A. Fleck, and M. F. Ashby. Effective properties of the octet-truss lattice material. *Journal of the Mechanics and Physics of Solids*, 49(8):1747–1769, 2001.

[13] L. Dong, V. Deshpande, and H. Wadley. Mechanical response of ti–6al–4v octet-truss lattice structures. *International Journal of Solids and Structures*, 60:107–124, 2015.

[14] L. Dong and H. Wadley. Mechanical properties of carbon fiber composite octet-truss lattice structures. *Composites Science and Technology*, 119:26–33, 2015.

[15] R. E. Doty, J. A. Kolodziejska, and A. J. Jacobsen. Hierarchical polymer microlattice structures. *Advanced Engineering Materials*, 14(7):503–507, 2012.

[16] S. d. S. e Lucato, J. Wang, P. Maxwell, R. McMeeking, and A. Evans. Design

and demonstration of a high authority shape morphing structure. *International journal of solids and structures*, 41(13):3521–3543, 2004.

[17] Z. C. Eckel, C. Zhou, J. H. Martin, A. J. Jacobsen, W. B. Carter, and T. A. Schaedler. Additive manufacturing of polymer-derived ceramics. *Science*, 351(6268):58–62, 2016.

[18] A. G. Evans, J. W. Hutchinson, N. A. Fleck, M. Ashby, and H. Wadley. The topological design of multifunctional cellular metals. *Progress in Materials Science*, 46(3-4):309–327, 2001.

[19] N. A. Fleck and X. Qiu. The damage tolerance of elastic–brittle, two-dimensional isotropic lattices. *Journal of the Mechanics and Physics of Solids*, 55(3):562–588, 2007.

[20] L. J. Gibson and M. F. Ashby. *Cellular solids: structure and properties*. Cambridge university press, 1999.

[21] J. J. Gilman. Tetrahedral truss, May 8 1984. US Patent 4,446,666.

[22] G. Gurtner and M. Durand. Stiffest elastic networks. In *Proceedings of the Royal Society of London A: Mathematical, Physical and Engineering Sciences*, volume 470, page 20130611. The Royal Society, 2014.

[23] D. Guth, M. Luersen, and P. Muñoz-Rojas. Optimization of three-dimensional truss-like periodic materials considering isotropy constraints. *Structural and Multidisciplinary Optimization*, 52:1–13, 2015.

[24] C. I. Hammetter, R. G. Rinaldi, and F. W. Zok. Pyramidal lattice structures for high strength and energy absorption. *Journal of Applied Mechanics*, 80(4):041015, 2013.

[25] R. Hutchinson, N. Wicks, A. Evans, N. Fleck, and J. Hutchinson. Kagome plate structures for actuation. *International Journal of solids and structures*, 40(25):6969–6980, 2003.

[26] A. J. Jacobsen, W. Barvosa-Carter, and S. Nutt. Compression behavior of micro-scale truss structures formed from self-propagating polymer waveguides. *Acta Materialia*, 55(20):6724–6733, 2007.

[27] A. J. Jacobsen, W. Barvosa-Carter, and S. Nutt. Micro-scale truss structures formed from self-propagating photopolymer waveguides. *Advanced Materials*, 19(22):3892–3896, 2007.

[28] A. J. Jacobsen, W. Barvosa-Carter, and S. Nutt. Micro-scale truss structures with three-fold and six-fold symmetry formed from self-propagating polymer waveguides. *Acta Materialia*, 56(11):2540–2548, 2008.

[29] K.-J. Kang. Wire-woven cellular metals: The present and future. *Progress in Materials Science*, 69:213–307, 2015.

[30] W. Kelvin and D. Weaire. The kelvin problem: foam structures of minimal surface area, 1996.

[31] R. W. Kraft. Construction arrangement, July 7 1964. US Patent 3,139,959.

[32] R. M. Latture, M. R. Begley, and F. W. Zok. Design and mechanical properties of elastically isotropic trusses. *Journal of Materials Research*, 33(3):249–263, 2018.

[33] R. M. Latture, R. X. Rodriguez, L. R. Holmes Jr, and F. W. Zok. Effects of nodal fillets and external boundaries on compressive response of an octet truss. *Acta Materialia*, 149:78–87, 2018.

[34] S. Li, Q. Xu, Z. Wang, W. Hou, Y. Hao, R. Yang, and L. Murr. Influence of cell shape on mechanical properties of ti–6al–4v meshes fabricated by electron beam melting method. *Acta biomaterialia*, 10(10):4537–4547, 2014.

[35] M. C. Messner. Optimal lattice-structured materials. *Journal of the Mechanics and Physics of Solids*, 96:162–183, 2016.

[36] G. W. Milton and A. V. Cherkaev. Which elasticity tensors are realizable? *Journal of engineering materials and technology*, 117(4):483–493, 1995.

[37] L. Murr, K. Amato, S. Li, Y. Tian, X. Cheng, S. Gaytan, E. Martinez, P. Shindo, F. Medina, and R. Wicker. Microstructure and mechanical properties of open-cellular biomaterials prototypes for total knee replacement implants fabricated by electron beam melting. *Journal of the mechanical behavior of biomedical materials*, 4(7):1396–1411, 2011.

[38] L. Murr, S. Gaytan, F. Medina, H. Lopez, E. Martinez, B. Machado, D. Hernandez, L. Martinez, M. Lopez, R. Wicker, et al. Next-generation biomedical implants using additive manufacturing of complex, cellular and functional mesh arrays. *Philosophical Transactions of the Royal Society of London A: Mathematical, Physical and Engineering Sciences*, 368(1917):1999–2032, 2010.

[39] J. F. Nye. *Physical properties of crystals: their representation by tensors and matrices*. Oxford university press, 1985.

[40] M. Osanov and J. K. Guest. Topology optimization for architected materials design. *Annual Review of Materials Research*, 46:211–233, 2016.

[41] J. B. Ostos, R. Rinaldi, C. M Hammetter, G. Stucky, F. Zok, and A. Jacob-

sen. Deformation stabilization of lattice structures via foam addition. *Acta Materialia*, 60(19):6476–6485, 2012.

[42] M. OMasta, L. Dong, L. St-Pierre, H. Wadley, and V. Deshpande. The fracture toughness of octet-truss lattices. *Journal of the Mechanics and Physics of Solids*, 98:271–289, 2017.

[43] H. Pettermann and J. Hüsing. Modeling and simulation of relaxation in viscoelastic open cell materials and structures. *International Journal of Solids and Structures*, 49(19):2848–2853, 2012.

[44] A. S. Phani and N. A. Fleck. Elastic boundary layers in two-dimensional isotropic lattices. *Journal of Applied Mechanics*, 75(2):021020, 2008.

[45] W. D. Pilkey and D. F. Pilkey. *Peterson's stress concentration factors*. John Wiley & Sons, 2008.

[46] D. Queheillalt, V. Deshpande, and H. Wadley. Truss waviness effects in cellular lattice structures. *Journal of Mechanics of Materials and Structures*, 2(9):1657–1675, 2007.

[47] D. Ramirez, L. Murr, S. Li, Y. Tian, E. Martinez, J. Martinez, B. Machado, S. Gaytan, F. Medina, and R. Wicker. Open-cellular copper structures fabri-

cated by additive manufacturing using electron beam melting. *Materials Science and Engineering: A*, 528(16):5379–5386, 2011.

[48] H. Rathbun, Z. Wei, M. He, F. Zok, A. Evans, D. Sypeck, and H. Wadley. Measurement and simulation of the performance of a lightweight metallic sandwich structure with a tetrahedral truss core. *Journal of Applied Mechanics*, 71(3):368–374, 2004.

[49] M. K. Ravari, M. Kadkhodaei, M. Badrossamay, and R. Rezaei. Numerical investigation on mechanical properties of cellular lattice structures fabricated by fused deposition modeling. *International Journal of Mechanical Sciences*, 88:154–161, 2014.

[50] R. Rinaldi, J. Bernal-Ostos, C. Hammetter, A. Jacobsen, and F. Zok. Effects of material heterogeneities on the compressive response of thiol-ene pyramidal lattices. *Journal of Materials Science*, 47(18):6621–6632, 2012.

[51] R. Rinaldi, C. Hammetter, and F. Zok. Ameliorating property gradients in photocured polymer lattices via thermal curing. *Materials Letters*, 105:155–158, 2013.

[52] L. Salari-Sharif, S. Godfrey, M. Tootkaboni, and L. Valdevit. The effect of

manufacturing defects on compressive strength of ultralight hollow microlattices: A data-driven study. *Additive Manufacturing*, 19:51–61, 2018.

[53] T. A. Schaedler, A. J. Jacobsen, A. Torrents, A. E. Sorensen, J. Lian, J. R. Greer, L. Valdevit, and W. B. Carter. Ultralight metallic microlattices. *Science*, 334(6058):962–965, 2011.

[54] O. Sigmund. Tailoring materials with prescribed elastic properties. *Mechanics of Materials*, 20(4):351–368, 1995.

[55] M. J. Silva and L. J. Gibson. The effects of non-periodic microstructure and defects on the compressive strength of two-dimensional cellular solids. *International Journal of Mechanical Sciences*, 39(5):549–563, 1997.

[56] M. A. Sutton, J. J. Orteu, and H. Schreier. *Image correlation for shape, motion and deformation measurements: basic concepts, theory and applications.* Springer Science & Business Media, 2009.

[57] D. D. Symons and N. A. Fleck. The imperfection sensitivity of isotropic two-dimensional elastic lattices. *Journal of Applied Mechanics*, 75(5):051011, 2008.

[58] A. Torrents, T. Schaedler, A. Jacobsen, W. Carter, and L. Valdevit. Characterization of nickel-based microlattice materials with structural hierarchy from the nanometer to the millimeter scale. *Acta Materialia*, 60(8):3511–3523, 2012.

[59] H. N. Wadley. Multifunctional periodic cellular metals. *Philosophical Transactions of the Royal Society of London A: Mathematical, Physical and Engineering Sciences*, 364(1838):31–68, 2006.

[60] H. N. Wadley, N. A. Fleck, and A. G. Evans. Fabrication and structural performance of periodic cellular metal sandwich structures. *Composites Science and Technology*, 63(16):2331–2343, 2003.

[61] S. A. Wainwright. *Mechanical design in organisms.* Princeton University Press, 1982.

[62] J. Wallach and L. Gibson. Mechanical behavior of a three-dimensional truss material. *International Journal of Solids and Structures*, 38(40-41):7181–7196, 2001.

[63] J. Wallach and L. J. Gibson. Defect sensitivity of a 3d truss material. *Scripta Materialia*, 45(6):639–644, 2001.

[64] N. Wicks and J. W. Hutchinson. Optimal truss plates. *International Journal of Solids and Structures*, 38(30-31):5165–5183, 2001.

[65] C. Yan, L. Hao, A. Hussein, and D. Raymont. Evaluations of cellular lattice structures manufactured using selective laser melting. *International Journal of Machine Tools and Manufacture*, 62:32–38, 2012.

[66] X. Zheng, H. Lee, T. H. Weisgraber, M. Shusteff, J. DeOtte, E. B. Duoss, J. D. Kuntz, M. M. Biener, Q. Ge, J. A. Jackson, et al. Ultralight, ultrastiff mechanical metamaterials. *Science*, 344(6190):1373–1377, 2014.

[67] F. W. Zok. On weakest link theory and weibull statistics. *Journal of the American Ceramic Society*, 100(4):1265–1268, 2017.

[68] F. W. Zok, R. M. Latture, and M. R. Begley. Periodic truss structures. *Journal of the Mechanics and Physics of Solids*, 96:184–203, 2016.